Charles University, Faculty of Mathematics and Physics
Institute of Theoretical Physics

Electronic relaxation of low-energy metastable states of atomic and molecular systems

Habilitation thesis

Přemysl Kolorenč

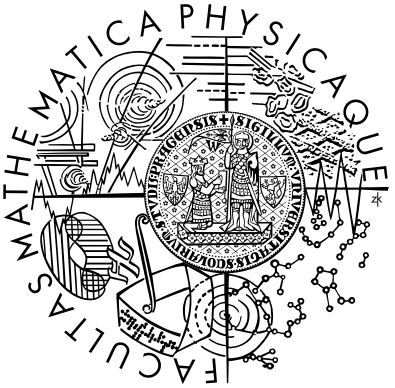

Prague 2021

Acknowledgement

My most sincere gratitude goes to my wife Marcela for her support, her positive thinking, and the most precious gift of all she is about to bring to our lives.

I would like to thank Jiří Horáček, who navigated my early scientific years, Lorenz S. Cederbaum, who introduced me to the rich world of ICD, and my collaborators and friends, Vitali Averbukh and Nicolas Sisourat. Last but not least, I am grateful to all my colleagues at the Institute of Theoretical Physics for the great (not only) working atmosphere they create.

In Prague, May 2021

Contents

Introduction

Deep inner-shell excitation or ionization of atoms and molecules produces highly excited states lying above the double or even multiple ionization thresholds. Such states relax predominantly by autoionization processes, typically involving two-electron transitions. A fundamental example is the Auger (or, more accurately, Auger-Meitner) effect, in which a valence electron refills the core vacancy, and another electron is emitted to the continuum [1, 2]. Auger effect is essentially of intra-atomic or intra-molecular nature and, thus, operative irrespective of the chemical environment. The surroundings manifest themselves by the chemical shift of the Auger lines [3], for instance, but the physics is not altered fundamentally. In 1997, the authors of the theoretical work [4] tried to answer the question of whether an excited state can decay non-radiatively exclusively due to interaction with an environment. It turned out that such decay transitions are not only possible but rather common phenomena, typical of relatively low-energy inner-shell vacancies in a wide variety of atomic and molecular systems.

Specifically, Cederbaum *et al.* [4] investigated hydrogen fluoride and water clusters, representative examples of hydrogen-bonded systems. They showed that while in the isolated HF molecule the F $2s$ inner-valence vacancy state lies below the double ionization threshold, new lower-lying doubly ionized states appear in the $(HF)_3$ trimer, and the autoionization channel opens. The final states are characterized by the spatial distribution of the outer-valence vacancies over two trimer sub-units, thus reducing their electrostatic repulsion compared to the case when both are located at the same HF molecule. The situation is completely analogous for the O $2s$ vacancy in water clusters and, as proved to be true later, also for a large number of van der Waals bonded systems and other weakly bound compounds. The decay process in question, depicted schematically in Fig. 1, was termed interatomic (inter-molecular) Coulombic decay (ICD).

It turns out that ICD is not only energetically accessible in a wide variety of systems but also very efficient, as confirmed both by the theoretical calculations and by the experiments. Typical lifetimes lie in the range from tens to few hundreds of femtoseconds [5,6], which is only one to two orders of magnitude slower than the characteristic lifetimes of the Auger decay. Therefore, ICD outpaces any competing radiative decay modes [7] and is usually the dominant decay pathway whenever the (intra-atomic) Auger decay is energetically forbidden. Furthermore, ICD is not the only interatomic decay transition available for inner-valence vacancies and other relatively low-energy excited states in clusters. Interatomic decay mechanisms thus affect substantially

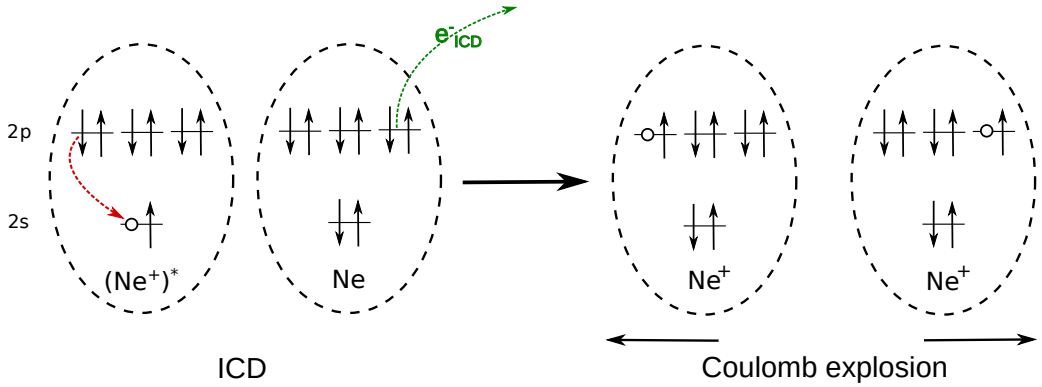

Figure 1: Schematic representation of the ICD process in neon dimer: $2p$ electron of the inner-valence ionized neon recombines with the initial $2s$ vacancy while another $2p$ electron from the neighbouring atom is ejected into the continuum. The resulting doubly charged dimer dissociates by the Coulomb explosion mechanism. The excess energy of the initial vacancy state is partitioned between the outgoing electron and kinetic energy of the ionic fragments.

the response of matter to ionizing radiation. For Auger-active core-ionized states, ICD and other interatomic electronic decay modes usually play only a minor role [8,9] but frequently occur in later steps of decay cascades following the local Auger decay of the initial core vacancy [10,11]. Those cascades can become particularly complex for micro-solvated metal ions and appear to be essential to our understanding of radiation chemistry and radiation damage in biological environments [12].

First indirect experimental evidence of ICD was presented in 2003 by Marburger *et al.*, who identified the process in neon clusters [13]. A year later, using the *cold target recoil ion momentum spectroscopy* (COLTRIMS) [14], Jahnke and coworkers conducted a very detailed study of ICD in the neon dimer [15]. All the decay products – the ICD electron and the neon ions generated by the Coulomb explosion (cf. Fig. 1) – were detected in coincidence, which enabled to verify the characteristic energy conservation pattern. Unlike in the atomic Auger decay, in which the energy of the secondary electron is quantized by the energy differences between the core vacancy and final dicationic states, in ICD the excess energy of the inner-vacancy state is shared by the outgoing electron and the ionic fragments. The actual distribution depends on the geometry (interatomic distance) of the system at the instant of the electronic transition, leading to distinctive diagonal lines in the coincidence maps. Since then, several remarkable experiments were performed, in concert with extensive theoretical exploration. A number of reviews are available, see, e.g., [16–18], or the very recent comprehensive effort by Jahnke and coworkers [19]. The purpose of this work is not to provide another review of the topic. Rather, we seize the opportunity to write a more self-contained work, which provides the theoretical methodology to study both the electronic and nuclear dynamics aspects of interatomic decay processes in polyatomic systems, and offers fundamental insight into the mechanisms driving such phenomena.

The thesis is based on the previously published candidate's contributions to the research topic but not necessarily restricted to them. For instance, Chapter 1 provides the general framework for the quantum-mechanical description of metastable states – resonances – which can be regarded as a standard theory. An exception is the discussion of local complex approximation for interfering resonances, where we attempt to point out and partly fill an existing gap in fundamental understanding. Chapter 2 is then devoted to *ab initio* methods for computing decay widths, the basic attribute of metastable states. The focus is on the Fano-ADC methodology, wherein lies the principal contribution of the candidate, but selected alternative approaches are introduced as well. In Chapter 3, we finally turn our attention specifically to the interatomic processes in rare gas clusters, analyze the various decay mechanisms, and demonstrate the role of nuclear dynamics on some illustrative examples. Here, the theory meets experiment, and most of the reported works thus result from broad international collaborations. An exception is the last section of the chapter, where we present as yet unpublished study undertaken specifically for this thesis to demonstrate the complete theoretical toolbox and, at the same time, resolve one disturbing controversy between the theory and experiment.

The papers enclosed in the appendix are referenced with the prefix [A] in the text. They represent the most significant candidate's contributions to the research field. Few more papers are sufficiently summarized in the main text; the complete list of publications, including topics not covered in the thesis, is available as a part of the candidate's professional CV.

Atomic units $e = m_e = \hbar = 1$ are used unless explicitly stated otherwise.

Chapter 1

General theory of non-radiative decay

In quantum mechanics, metastable states (resonances) can be associated with the so-called Gamow-Siegert states [20,21], which are eigenstates of the time-independent Schrödinger equation for complex energies. Corresponding wave functions are characterized by exponential divergence in the asymptotic region, which is connected with the imaginary part of the energy. Siegert energies can be identified with poles of the S-matrix [22], and resonances usually manifest themselves by rapid variations of phase-shifts and scattering cross-sections.

An alternative way to study metastable states, which is adopted in the present work, is to characterize them as *discrete states* embedded in a continuum into which they can decay [23]. This concept, introduced by Dirac [24], is at the heart of the theory of resonances developed mainly by Fano [25] and Feshbach [26]. Even though we start with a discrete state associated with real energy, interaction with the continuum brings about *complex level shift* which pushes the energy into the complex plane. In both approaches, the imaginary part of the energy, $-i\Gamma/2$, is related to the lifetime of the metastable state as $\tau = \hbar/\Gamma$. The quantity Γ is called the decay width.

In this chapter, we start by the description of the decay of metastable states from a purely electronic point of view. The results thus describe either an isolated atom or a polyatomic system in the fixed nuclei limit. We do not attempt to provide an exhaustive review but rather to facilitate the connection between different frameworks used to study resonance phenomena and introduce the essential terms and techniques. We start with an overview of the time-independent formulation in order to elucidate the origin of the complex energy and its relation to the uncertainty of the resonance position. We then switch to the time-dependent picture, which is more appropriate for the treatment of time-dependent Hamiltonians, e.g., those involving electric fields. This formulation also provides more natural insight into the process itself, which will be particularly beneficial when we include also the nuclear degrees of freedom among dynamical variables. The time-dependent formulation of quantum theory is also better suited to make contact with the classical description of the heavy-particle motion and, thus, is essential to develop semi-classical methods [27–29].

1.1 Time-independent picture

The process of interest – inner-shell ionization and subsequent decay of the resulting excited state – can be described as follows. Initially, the system is in a N-electron stationary state $|\phi_i\rangle$. Interaction with an external field or particle impact brings the system into an intermediate state $|\phi_d\rangle|\epsilon_0\rangle$, where $|\phi_d\rangle$ is the metastable $(N-1)$-electron state of the system (the discrete state), and $|\epsilon_0\rangle$ is energy-normalized wave function of the outgoing primary electron. We assume that its energy is high enough such that sudden approximation [30] is applicable and any subsequent interaction between the primary electron and the residual ion can be neglected. The metastable state then decays by electron emission into continuum of states $|\chi(\epsilon)\rangle$, which represent the final di-cationic state of the system $|\chi\rangle$ with secondary electron emitted with energy ϵ.[1] Validity of this approach, based on the concept of two-step character of the ionization and decay process, is discussed in Refs. [31, 32].

The full Hamiltonian of the system reads

$$\hat{H} = \hat{H}_{el} + \hat{V}, \tag{1.1a}$$

where $\hat{H}_{el}$ is the Hamiltonian of the N-electron system and $\hat{V}$ is the external excitation operator driving the primary inner-shell ionization. The electronic Hamiltonian consists of the kinetic energy operator of the electrons and the electron-electron, electron-nuclei and nuclei-nuclei Coulomb interactions. In polyatomic systems, it is thus parametrically dependent on the nuclear coordinates. We assume that the initial state $|\phi_i\rangle$ is an eigenstate of $\hat{H}_{el}$ and, therefore, interacts with the other states only through $\hat{V}$. The full Hamiltonian $\hat{H}$ can then be expanded as the diagonal part of $\hat{H}_{el}$,

$$\hat{H}_0 = |\phi_i\rangle E_i \langle\phi_i| + \int d\epsilon_0 \, |\phi_d\rangle|\epsilon_0\rangle(E_d + \epsilon_0)\langle\epsilon_0|\langle\phi_d| + \int d\epsilon_0 \int d\epsilon \, |\chi(\epsilon)\rangle|\epsilon_0\rangle(E_f + \epsilon + \epsilon_0)\langle\epsilon_0|\langle\chi(\epsilon)|, \tag{1.1b}$$

and the interaction term comprising the off-diagonal part of $\hat{H}_{el}$ and the excitation operator,

$$\hat{H}_I = \int d\epsilon_0 \int d\epsilon \, |\chi(\epsilon)\rangle|\epsilon_0\rangle W(\epsilon)\langle\epsilon_0|\langle\phi_d| + \int d\epsilon_0 \; |\phi_d\rangle|\epsilon_0\rangle V(\epsilon_0)\langle\phi_i| + h.c. \tag{1.1c}$$

Possible direct double ionization through $\hat{V}$ is not considered, the final states can thus be reached only resonantly via $|\phi_d\rangle$. Under the above assumption of fast primary electron, any possible dependence of the coupling elements W on ϵ_0 is weak and can be usually neglected.

The probability per unit time for the transition from the initial state $|I\rangle = |\phi_i\rangle$ to the final state $|F\rangle = |\chi(\epsilon)\rangle|\epsilon_0\rangle$ reads [33, 34]

$$P_{FI}(\epsilon, \epsilon_0) = 2\pi |\langle F|\hat{T}(E_i)|I\rangle|^2 \delta(E_i - E_f - \epsilon - \epsilon_0). \tag{1.2}$$

[1] Thorough the present work, we consider only angularly averaged cross sections and spectra. For this reason and for the sake of simplified notation, any possible dependence of Hamiltonian matrix elements on the direction of the emitted particles is not taken into account and the electronic states are characterized only by the energy.

Here, $\hat{T}$ is the on-shell T-matrix

$$\hat{T}(E) = \hat{H}_I + \hat{H}_I \hat{G}_0(E)\hat{T}(E) \tag{1.3}$$

and the free Green's function is defined as

$$\hat{G}_0(E) = \lim_{\eta\to 0^+} (E - \hat{H}_0 - i\eta)^{-1}. \tag{1.4}$$

To evaluate the transition probability (1.2), we expand the T-matrix element in a perturbation series

$$\langle F|\hat{T}(E)|I\rangle = \langle F|\hat{H}_I|I\rangle + \langle F|\hat{H}_I\hat{G}_0(E)\hat{H}_I|I\rangle + \langle F|\hat{H}_I\hat{G}_0(E)\hat{H}_I\hat{G}_0(E)\hat{H}_I|I\rangle + \dots \tag{1.5}$$

and use the spectral representation of the free Green's function,

$$\hat{G}_0(E) = \lim_{\eta\to 0+} \left(\frac{|\phi_i\rangle\langle\phi_i|}{E - E_i + i\eta} + \int d\epsilon_0 \, \frac{|\phi_d\rangle|\epsilon_0\rangle\langle\epsilon_0|\langle\phi_d|}{E - E_d - \epsilon_0 + i\eta} + \int d\epsilon_0 \int d\epsilon \, \frac{|\chi(\epsilon)\rangle|\epsilon_0\rangle\langle\epsilon_0|\langle\chi(\epsilon)|}{E - E_f - \epsilon - \epsilon_0 + i\eta} \right). \tag{1.6}$$

Closed-form expression for P_{FI} can be derived assuming the golden rule to be valid for the initial excitation process [34, 35]. The excitation matrix element $V(\epsilon_0)$ is then considered only up to the first order while the decay matrix element $W(\epsilon)$ to infinite order. This approximation is valid, for instance, in the case of weak-field photoionization, i.e., in the regime when the ionization probability is proportional to the field intensity.

Evaluating explicitly the first few terms in the series (1.5), we observe that only terms with even power of $\hat{H}_I$ contribute:

$$\langle F|\hat{H}_I|I\rangle = 0, \tag{1.7a}$$

$$\langle F|\hat{H}_I\hat{G}_0(E)\hat{H}_I|I\rangle = W(\epsilon)G_0^d(E)V(\epsilon_0), \tag{1.7b}$$

$$\langle F|\hat{H}_I\hat{G}_0(E)\hat{H}_I\hat{G}_0(E)\hat{H}_I|I\rangle = 0, \tag{1.7c}$$

$$\langle F|\hat{H}_I\hat{G}_0(E)\hat{H}_I\hat{G}_0(E)\hat{H}_I\hat{G}_0(E)\hat{H}_I|I\rangle = W(\epsilon)G_0^d(E)\mathcal{F}(E-\epsilon_0)G_0^d(E)V(\epsilon_0). \tag{1.7d}$$

We have introduced the discrete-state Green's function matrix element

$$G_0^d(E) = \langle\epsilon_0|\langle\phi_d|G_0(E)|\phi_d\rangle|\epsilon_0\rangle = \lim_{\eta\to 0^+} (E - E_d - \epsilon_0 + i\eta)^{-1} \tag{1.8}$$

and the *level shift* function ($E' = E - \epsilon_0$)

$$\mathcal{F}(E') = \langle\epsilon_0|\langle\phi_d|\hat{H}_I\hat{G}_0(E'+\epsilon_0)\hat{H}_I|\phi_d\rangle|\epsilon_0\rangle = \lim_{\eta\to 0^+} \int d\epsilon' \, W^*(\epsilon')(E' - E_f - \epsilon' + i\eta)^{-1}W(\epsilon'). \tag{1.9}$$

The contribution (1.7c) and other odd-order terms vanish since $\hat{H}_I$ couples both $|F\rangle$ and $|I\rangle$ only to the discrete state and the expressions like $\langle\epsilon_0|\langle\phi_d|\hat{G}_0(E)\hat{H}_I\hat{G}_0(E)|\phi_d\rangle|\epsilon_0\rangle$ are zero due to the diagonal and off-diagonal characters of $\hat{G}_0(E)$ and H_I, respectively. Higher even-order

terms, on the other hand, have the formal structure analogous to Eq. (1.7d), and the whole perturbation expansion for the T-matrix element can be written as

$$\langle F|\hat{T}(E)|I\rangle = W(\epsilon)\sum_{n=0}^{\infty}[G_0^d(E)\mathcal{F}(E-\epsilon_0)]^n G_0^d(E)V(\epsilon_0). \tag{1.10}$$

Summation of the resulting geometric series leads to the final formula for the T-matrix element

$$\langle F|\hat{T}(E)|I\rangle = W(\epsilon)[E-\epsilon_0-E_d-\mathcal{F}(E-\epsilon_0)]^{-1}V(\epsilon_0). \tag{1.11}$$

The resolvent in the above expression can be interpreted as Green's function corresponding to an effective, energy-dependent Hamiltonian governing the dynamics of the discrete state $|\phi_d\rangle$ [27, 34],

$$\mathcal{H}_d(E') = E_d + \mathcal{F}(E'), \tag{1.12}$$

in which the level shift $\mathcal{F}(E')$ fully accounts for the interaction with the continuum. $V(\epsilon_0)$ and $W(\epsilon)$ then represent the entrance and exit amplitudes, respectively. Eq. (1.11) is thus in accordance with the physical picture of the system being excited into the discrete state where it evolves under the action of $\mathcal{H}_d(E')$ and eventually decays through $W(\epsilon)$ to the continuum of final states.

Invoking the Sokhotski-Plemelj theorem ($\mathcal{P}$ stands for the Cauchy principal value integration),

$$\lim_{\eta\to 0^+}\int_a^b \frac{f(x)}{x\pm i\eta}\,dx = \mp i\pi f(0) + \mathcal{P}\int_a^b \frac{f(x)}{x}\,dx, \qquad a<0<b, \tag{1.13}$$

the level shift Eq. (1.9) is readily evaluated as [27]

$$\mathcal{F}(E') = -\frac{i}{2}\Gamma(E'-E_f) + \Delta(E'-E_f) \tag{1.14a}$$

with

$$\Gamma(\epsilon) = 2\pi|W(\epsilon)|^2, \qquad \Delta(\epsilon) = \frac{1}{2\pi}\mathcal{P}\int d\epsilon'\,\frac{\Gamma(\epsilon')}{\epsilon'-\epsilon}. \tag{1.14b}$$

Both $\Gamma(\epsilon)$ and $\Delta(\epsilon)$ are real-valued (for real ϵ) and represent the decay width and real level shift functions, respectively. Inserting (1.14) into (1.11) and setting $E = E_i = E_f + \epsilon_0 + \epsilon$, the transition probability (1.2) reads

$$P_{FI}(\epsilon,\epsilon_0) = \frac{\Gamma(\epsilon)}{[E_f+\epsilon-E_d-\Delta(\epsilon)]^2+\Gamma(\epsilon)^2/4}V(\epsilon_0)^2. \tag{1.15}$$

The factor $V(\epsilon_0)^2$ is not really relevant for our purposes and, in the considered regime of fast primary electron, typically only weakly depends on ϵ_0. It can be integrated out to obtain the spectrum of the secondary electron in the form of a generalized Lorentzian function,

$$\sigma(\epsilon) = \int d\epsilon_0\, P_{FI}(\epsilon,\epsilon_0) \propto \frac{\Gamma(\epsilon)}{[E_f+\epsilon-E_d-\Delta(\epsilon)]^2+\Gamma(\epsilon)^2/4}, \tag{1.16}$$

where the proportionality factor is the total inner-shell ionization probability.

Assuming sufficiently weak energy dependence of the decay width function $\Gamma(\epsilon)$, the spectrum has maximum for $\epsilon = \epsilon_{res}$ that is given by the solution of the implicit equation

$$E_{res} = E_d + \Delta(\epsilon_{res}) = E_f + \epsilon_{res}. \tag{1.17}$$

This energy corresponds to the pole of the K-matrix [22] and defines the *real* resonance energy. The pole of the T-matrix (1.11), which defines *complex* resonance energy z_{res}, satisfies the equation (substituting the energy conservation $E_i - \epsilon_0 = E_f + \epsilon$)

$$Z_{res} = E_d + \Delta(z_{res}) - \frac{i}{2}\Gamma(z_{res}) = E_f + z_{res}. \tag{1.18}$$

This complex energy coincides with the energy associated with the divergent Gamow-Siegert state mentioned at the beginning of the chapter. When $\Gamma(\epsilon)$ depends strongly on the energy, the transition probability (1.15) deviates significantly from the Lorentzian shape. It occurs typically near threshold, i.e., for ϵ close to zero. In the time-dependent picture, it is manifested by non-exponential character of the decay and the notion of the decay width gradually becomes ill-defined.

The finite width of the secondary electron spectrum has its origin in the ambiguity of the energy of the discrete state. Neither the discrete state $|\phi_d\rangle$ nor the continuum states $|\chi(\epsilon)\rangle$ are eigenstates of the $(N-1)$-electron Hamiltonian. Rather, they merely form a basis of the respective Hilbert space. The solution of the time-independent Schrödinger equation (TISE)

$$\hat{H}_{el}|\psi(E)\rangle = E|\psi(E)\rangle \tag{1.19}$$

in the continuum spectral region can thus be expanded as

$$|\psi(E)\rangle = a(E)|\phi_d\rangle + \int d\epsilon\, b(E,\epsilon)|\chi(\epsilon)\rangle. \tag{1.20}$$

This ansatz complies with the observation that, around the resonance energy, the unbound electron is localized in the interaction region near the molecule with a large probability, while at large distances the wave function is not damped exponentially as a regular bound state but oscillates like a free particle [23]. Inserting the expansion (1.20) into TISE and solving for the coefficient $a(E)$ yields [25]

$$|a(E)|^2 = \frac{1}{2\pi}\frac{\Gamma(\epsilon)}{[E_f + \epsilon - E_d - \Delta(\epsilon)]^2 + \Gamma(\epsilon)^2/4}, \tag{1.21}$$

with the decay width and level shift functions defined by Eq. (1.14b). Excitation of the discrete state thus populates a band of stationary continuum states characterized by the width $\Gamma(\epsilon)$. In turn, the subsequent decay process does not represent transition with a precisely defined energy, resulting into a finite width of the spectral line.

1.2 Time-dependent picture

The foundation of the time-dependent formulation of the decay process is the time-dependent Schrödinger equation (TDSE)

$$i\frac{\partial}{\partial t}|\psi(t)\rangle = \hat{H}(t)|\psi(t)\rangle. \tag{1.22}$$

We consider the same basis of electronic states as introduced in Sec. 1.1, in which the structure of the Hamiltonian $\hat{H}(t)$ is given by Eqs. (1.1). The explicit time-dependence arises from the excitation operator $\hat{V}(t)$. For the sake of argument, we consider interaction with electromagnetic field $\boldsymbol{E}(t)$ in the dipole approximation, in which $\hat{V}(t)$ reads [36]

$$\hat{V}(t) = \hat{\boldsymbol{D}} \cdot \boldsymbol{E}(t), \tag{1.23}$$

with $\hat{\boldsymbol{D}}$ being the dipole operator and bold letters denoting vector quantities. The relevant matrix element is then of the form

$$\langle\epsilon_0|\langle\phi_d|\hat{V}(t)|\phi_i\rangle = V(\epsilon_0)g(t). \tag{1.24}$$

The full time-dependent N-electron wave function $|\psi(t)\rangle$ can be expanded as

$$|\Psi(t)\rangle = c_i(t)|\phi_i\rangle + \int d\epsilon_0\, e^{-i\epsilon_0 t}a(\epsilon_0,t)|\phi_d\rangle|\epsilon_0\rangle + \int d\epsilon_0 \int d\epsilon\, e^{-i\epsilon_0 t}b(\epsilon_0,\epsilon,t)|\chi(\epsilon)\rangle|\epsilon_0\rangle, \tag{1.25}$$

where we have already explicitly extracted the trivial phase factors corresponding to the primary electron from the coefficients a and b. Inserting (1.25) into TDSE and projecting onto individual electronic states, we obtain set of coupled differential equations in the form (dot denotes time derivative)

$$i\dot{c}_i(t) = E_i\, c_i(t) + g^*(t)\int d\epsilon_0\, V^*(\epsilon_0)e^{-i\epsilon_0 t}a(\epsilon_0,t), \tag{1.26a}$$

$$i\dot{a}(\epsilon_0,t) = E_d\, a(\epsilon_0,t) + e^{i\epsilon_0 t}V(\epsilon_0)g(t)c_i(t) + \int d\epsilon\, W^*(\epsilon)b(\epsilon_0,\epsilon,t), \tag{1.26b}$$

$$i\dot{b}_f(\epsilon_0,\epsilon,t) = (E_f+\epsilon)\dot{b}_f(\epsilon_0,\epsilon,t) + W(\epsilon)a(\epsilon_0,t). \tag{1.26c}$$

Initial conditions are $|c_i(t\to-\infty)|^2 = 1$ and $a(\epsilon_0, t\to-\infty) = b(\epsilon_0,\epsilon,t\to-\infty) = 0$. In its full complexity, the set can only be solved numerically. However, under certain approximations, which are found to be legitimate in many cases of interest, the equations can be decoupled and solved explicitly. The procedure can be found, e.g., in Ref. [36] and we will review it here for the sake of completeness and readers convenience.

We start by invoking the weak-field approximation for the excitation operator and, in analogy to Sec. 1.1, keep only terms linear in V. Since the discrete state is only populated due to the excitation operator and thus $a(\epsilon_0,t)$ by itself is linear in V, we can neglect the recoupling of the intermediate to the initial state [second term on the right hand side (RHS) of Eq. (1.26a)] and assume that the initial state remains almost unchanged during the whole process. Eq. (1.26a) then has trivial solution,

$$c_i(t) = c_i(0)e^{-iE_i t}. \tag{1.27}$$

We notice that, as a by-product, this approximation also leads to decoupling of equations corresponding to different values of ϵ_0. For the sake of brevity we thus omit this parameter in $a(t)$ and $b(\epsilon, t)$ in the following, but note that the dependence is still there through the second term on RHS in Eq. (1.26b).

Second step comprise the formal solution of Eq. (1.26c),[2]

$$b(\epsilon, t) = -ie^{-i(E_f+\epsilon)t} \int_{-\infty}^{t} d\tau\, e^{i(E_f+\epsilon)\tau} W(\epsilon) a(\tau). \tag{1.28}$$

Substituting (1.27) and (1.28) into (1.26b), the equation for the discrete state coefficient reads

$$i\dot{a}(t) = E_d a(t) + V(\epsilon_0) g(t) e^{-i(E_i-\epsilon_0)t} - i \int_{-\infty}^{t} d\tau \mathcal{F}(t-\tau) a(\tau). \tag{1.29}$$

The equation is decoupled from those for the continuum components but interaction with the continuum results in non-locality in time – the evolution of $a(t)$ is determined by its value at all previous times. We have used the same notation $\mathcal{F}$ for the *memory kernel*,

$$\mathcal{F}(\tau) = \int d\epsilon'\, W^*(\epsilon') e^{-i(E_f+\epsilon')\tau} W(\epsilon'), \tag{1.30}$$

as for the level shift function (1.9) since the two functions are connected by Laplace transformation [27],

$$\mathcal{F}(E) = \frac{1}{i} \int_{0}^{\infty} d\tau e^{iE\tau} \mathcal{F}(\tau). \tag{1.31}$$

The memory effects thus reflect the energy-dependence of the effective Hamiltonian (1.12) and vice versa. Indeed, for energy-independent coupling, $\mathcal{F}(\tau)$ is proportional to $\delta(\tau)$ – Laplace pre-image of a constant – and the time evolution is Markovian. For a weak energy dependence of $W(\epsilon)$ on energy, we can thus expect that the memory will be limited to very short times. It suggests that if the memory time is shorter than the characteristic timescale of the process, the non-local operator in Eq. (1.29) can be replaced by a suitable local approximation. It in turn corresponds to a constant approximation of the energy-dependent level shift function (1.14),

$$\mathcal{F}(E) \to \mathcal{F}^{loc} = \Delta^{loc} - \frac{i}{2}\Gamma^{loc} \quad \Longleftrightarrow \quad \mathcal{F}(\tau) \to i\mathcal{F}^{loc}\delta(\tau). \tag{1.32}$$

This is the so-called *local complex potential* (LCP) approximation (in the fixed-nuclei limit) within the time-dependent framework. In the time-independent picture, LCP thus provides energy-independent approximation to the effective Hamiltonian (1.12),

$$\mathcal{H}_d^{loc} = E_d + \Delta^{loc} - \frac{i}{2}\Gamma^{loc}. \tag{1.33}$$

[2]This is only possible due to the absence of continuum-continuum coupling, $\langle\chi(\epsilon')|\hat{H}_{el}|\chi(\epsilon)\rangle \propto \delta(\epsilon-\epsilon')$.

In general, LCP is not uniquely defined as it is not clear what constant value should be chosen for the level shift function. We defer the derivation of LCP until Sec. 1.3, here we only state that two possible definitions are given by Eqs. (1.17) and (1.18). Setting $\mathcal{F}^{loc} = \mathcal{F}(\epsilon_{res})$ is motivated by the highest transition probability for the (real) secondary electron energy ϵ_{res}, while $\mathcal{F}^{loc} = \mathcal{F}(z_{res})$ corresponds to the pole of the T-matrix. Discussion of the consequences of different choices can be found, e.g., in Ref. [37]. Since we will employ the LCP approximation thorough this work, from now on we drop the superscript *loc* at the approximate $\mathcal{H}_d$, Δ and Γ, as it is implied by the missing argument ϵ. Whenever the exact level shift function is used, it will be indicated by the explicit energy dependence.

Within the LCP approximation, the time evolution of the discrete state is greatly simplified. Without the source term (i.e., after the ionizing pulse), the survival probability reads

$$|a(t)|^2 \propto e^{-\Gamma t}. \tag{1.34}$$

LCP thus predicts purely exponential decay. General solution of (1.29) with the local kernel (1.32) yields

$$a(t) = -ie^{-i(E_d+\Delta-i\Gamma/2)t} \int_{-\infty}^{t} d\tau e^{i(E_d+\Delta-i\Gamma/2+\epsilon_0-E_i)\tau} g(\tau) V(\epsilon_0). \tag{1.35}$$

Introducing Fourier transform of the excitation function,

$$g(\tau) = \frac{1}{\sqrt{2\pi}} \int d\omega \, e^{-i\omega\tau} g(\omega), \tag{1.36}$$

the solution can be further rewritten as

$$a(t) = \frac{1}{\sqrt{2\pi}} \int d\omega \, \frac{g(\omega)}{E_i - \epsilon_0 - E_d - \Delta + i\Gamma/2 + \omega} e^{-i(E_i-\epsilon_0+\omega)t} V(\epsilon_0) \tag{1.37}$$

Inserting this formula into Eq. (1.28) we finally obtain

$$b(\epsilon, t) = -\frac{i}{\sqrt{2\pi}} e^{-i(E_f+\epsilon)t} \int d\omega \int_{-\infty}^{t} d\tau \, e^{-i(E_i+\omega-\epsilon_0-E_f-\epsilon)\tau} \, W(\epsilon) \frac{g(\omega)}{E_i + \omega - \epsilon_0 - E_d - \Delta + i\Gamma/2} V(\epsilon_0). \tag{1.38}$$

The coincidence spectrum $\sigma(\epsilon, \epsilon_0)$, corresponding to the transition probability P_{FI} of Eq. (1.15), is obtained within the time-dependent picture as

$$\sigma(\epsilon, \epsilon_0) = \lim_{t\to\infty} |b(\epsilon, t)|^2, \tag{1.39}$$

resulting into[3]

$$\sigma(\epsilon, \epsilon_0) = \frac{2\pi |W(\epsilon)|^2}{(E_f + \epsilon - E_d - \Delta)^2 + \Gamma^2/4} |V(\epsilon_0)|^2 |g(E_f + \epsilon_0 + \epsilon - E_i)|^2. \tag{1.40}$$

[3]In the limit $t \to \infty$, the integral over τ converges to $2\pi\delta(\omega + E_i - E_f - \epsilon_0 - \epsilon)$ and the remaining time-dependence of the phase of $b(\epsilon, t)$ cancels in the absolute value squared.

As in the time-independent picture, within the sudden approximation, the dependence on ϵ_0 can be trivially integrated out, yielding the secondary electron spectrum

$$\sigma(\epsilon) \propto \frac{2\pi|W(\epsilon)|^2}{(E_f + \epsilon - E_d - \Delta)^2 + \Gamma^2/4}. \tag{1.41}$$

Compared to the exact solution (1.16), LCP approximation resulted into substitution of the energy-independent level shift and decay width in the denominator. In the numerator we can still identify the exact energy-dependent decay width function. In the time-independent picture, such a result can be obtained by substituting the energy-independent LCP level shift for the exact $\mathcal{F}(\epsilon)$ in the effective Hamiltonian (1.12) but keeping the energy dependence of the exit amplitude $W(\epsilon)$ in the T-matrix element (1.11). Replacing also the numerator by the energy-independent decay width Γ leads to an approximation known in the context of electron-molecule scattering as *boomerang model* [38, 39]. However, Cederbaum and Domcke [40] has shown that the *semi-local* approximation, in which the entry and exit amplitudes are treated exactly, indeed provides improved results and significantly extends the applicability of LCP.

1.3 Local complex potential approximation

In this section we present derivation of the local complex potential approximation in the framework of the time-dependent picture. We adopt the method of Domcke [27], which is also reminiscent of the *adiabatic elimination of the continuum* by Fedorov and coworkers [41, 42]. We choose this approach because it enables systematic construction of corrections to the standard LCP, and can help to resolve the ambiguity in definition of LCP mentioned below Eq. (1.32). Simplified derivation can be found in Ref. [36].

The starting point is the third term on RHS of Eq. (1.29) with the memory kernel (1.30),[4]

$$Z[a(t)] \equiv -i \int_0^\infty d\tau \int d\epsilon\, W^*(\epsilon) e^{-i(E_f+\epsilon)\tau} W(\epsilon) a(t-\tau) \tag{1.42}$$

We expect that, due to the weak energy dependence of $W(\epsilon)$, the memory kernel decays quickly in time with some characteristic decay time τ_M. Therefore, to determine the local approximation to the RHS, we can expand $a(t-\tau)$ into Taylor series around t and evaluate the leading term. To this end, we first extract from $a(t)$ the dominant time-dependence in the form of a phase factor,

$$a(t) = e^{-iE_r t}\tilde{a}(t), \tag{1.43}$$

where the hitherto unknown E_r will be determined later. The remaining time-dependence of $\tilde{a}(t)$ is assumed to be weak and we can thus write

$$\tilde{a}(t-\tau) = \tilde{a}(t) - \tau\dot{\tilde{a}}(t) + O(\tau^2) \tag{1.44}$$

[4] We have made the substitution $\tau \to t - \tau$.

and, in turn,

$$Z[a(t)] = Z^{(0)}[a(t)] + Z^{(1)}[a(t)]. \tag{1.45}$$

It is important to note that this approach is justified only if the excitation function $g(t)$ [c.f. Eq. (1.24)] is also slowly varying with respect to the timescale defined by the memory time τ_M. If, for example, the initial excitation is essentially instantaneous and $g(t) \approx \delta(t - t_0)$, $\tilde{a}(t)$ will not be smooth around t_0. We will discuss this problem further below. Taking only the τ-independent term of the expansion (1.44) and introducing the convergence factor $e^{-\eta\tau}$, the leading contribution to (1.42) reads

$$\begin{aligned} Z^{(0)}[a(t)] &= -ie^{-iE_r t}\tilde{a}(t) \int d\epsilon\, |W(\epsilon)|^2 \int_0^\infty d\tau e^{-i(E_f+\epsilon-E_r-i\eta)\tau} \\ &= a(t) \int d\epsilon\, \frac{|W(\epsilon)|^2}{E_r - E_f - \epsilon + i\eta} \overset{\eta\to 0^+}{=} a(t) \left(\Delta(E_r - E_f) - \frac{i}{2}\Gamma(E_r - E_f) \right). \end{aligned} \tag{1.46}$$

In the last step, we have invoked the Sokhotski-Plemelj theorem and the definition of the level shift function, Eqs. (1.13) and (1.14).

We have thus recovered the expected form of the complex level shift but the resonance energy E_r remains unknown. Optimal choice can be determined by minimizing the correction stemming from the linear term of the Taylor series (1.44),

$$\begin{aligned} Z^{(1)}[a(t)] &= ie^{-iE_r t}\dot{\tilde{a}}(t) \int d\epsilon\, |W(\epsilon)|^2 \int_0^\infty d\tau\, \tau e^{-i(E_f+\epsilon-E_r-i\eta)\tau} \\ &= -ie^{-iE_r t}\dot{\tilde{a}}(t) \int d\epsilon\, \frac{|W(\epsilon)|^2}{(E_r - E_f - \epsilon + i\eta)^2}. \end{aligned} \tag{1.47}$$

The integral can be evaluated *per partes*. The coupling $W(\epsilon)$ vanishes for $\epsilon \to \infty$ but can be nonzero[5] for $\epsilon \to 0$. The correction thus reads

$$Z^{(1)}[a(t)] = -ie^{-iE_r t}\dot{\tilde{a}}(t) \left[\frac{|W(0)|^2}{E_r - E_f} + \frac{1}{2\pi}\mathcal{P}\int d\epsilon\, \frac{\Gamma'(\epsilon)}{E_r - E_f - \epsilon} - \frac{i}{2}\Gamma'(E_r - E_f) \right]. \tag{1.48}$$

Except the first term in square brackets, it is proportional to the derivative of $\Gamma(\epsilon)$, corroborating the presumption that LCP is appropriate for weakly energy dependent decay width function. The first term, $|W(0)|^2/(E_r - E_f)$, will be small if the resonance energy is well above threshold (measured by the scale of Γ), which is another known condition for the LCP to be valid.

Denominating the term in square brackets in Eq. (1.48) as δ and noting that $e^{-iE_r t}\dot{\tilde{a}}(t) = \dot{a}(t) + iE_r a(t)$, the equation (1.29) with the first two contributions to the non-local term reads

$$i\dot{a}(t)(1+\delta) = \left[E_d + \Delta(E_r - E_f) - \frac{i}{2}\Gamma(E_r - E_f) + E_r\delta \right] a(t) + V(\epsilon_0)g(t)e^{-i(E_i-\epsilon_0)t}. \tag{1.49}$$

[5] For the long range Coulomb interaction, the decay width attains a finite value at threshold [43, 44]

Keeping only terms at most linear in δ, the equation can be rearranged to

$$i\dot{a}(t) = \left[E_d + \Delta(E_r - E_f) - \frac{i}{2}\Gamma(E_r - E_f)\right] a(t) + V(\epsilon_0)g(t)e^{-i(E_i-\epsilon_0)t} + \delta\left[E_r - E_d - \Delta(E_r - E_f) + \frac{i}{2}\Gamma(E_r - E_f)\right] a(t) - \delta\, V(\epsilon_0)g(t)e^{-i(E_i-\epsilon_0)t}. \quad (1.50)$$

The first line is the LCP approximation and the second line represents the first correction due to dependence of the discrete state-continuum coupling on the energy. After the ionizing pulse is over [$g(t) = 0$], the correction is minimized if the expression in the square bracket on the second line is set to zero. We thus recover the equation (1.18) for the complex pole of the T-matrix and obtain $E_r = E_f + z_{res}$. However, with this choice, E_r would attain negative imaginary part and the time integrals in Eqs. (1.46) and (1.47) would diverge. Therefore, E_r has to be restricted to be real and the optimal definition of the resonance energy reads

$$E_r = E_d + \Delta(E_r - E_f), \quad (1.51)$$

which is Eq. (1.17) for the pole of the K-matrix and (approximately) the maximum of the secondary electron spectrum (1.16).

The requirement that E_r must be real is, however, connected with this particular derivation. As already mentioned below Eq. (1.32), definition of LCP through the complex pole of the T-matrix is also commonly used approach. For sufficiently narrow resonances and weakly energy-dependent discrete state-continuum coupling, the difference is small. Furthermore, in practical situations where the resonance parameters are determined by *ab initio* methods, the choice is either dictated by the method itself, or these rather subtle differences are below their resolving power. An example of the former case are methods based on the complex absorbing potential or complex scaling, which search directly for the Gamow-Siegert states and thus determine the complex resonance energy z_{res} as the corresponding eigenvalue of the Hamiltonian.

Before moving on to the discussion of interacting metastable states, let us comment briefly on the problem of instantaneous *broadband*[6] ionization, represented by the excitation function $g(t) = \delta(t)$. In this case, $a(t)$ is zero for $t < 0$ and the time integral in Eq. (1.46) only extends from 0 to t instead to infinity. For $t \gg \tau_M$ the upper bound can be readily extended to infinity without changing its value and the derived LCP approximation is valid. For t shorter or comparable the decay time of the memory kernel, however, already the leading contribution $Z^{(0)}[a(t)]$ will contain a time-dependent correction. This is special manifestation of the fundamental result that, for very short times, the decay of an unstable state is necessarily non-exponential due to its finite spread in energy [45–47].

[6]Fourier transform $g(\omega)$ of $g(t) \propto \delta(t)$ is constant.

1.4 Interacting metastable states

So far, we have only discussed the simplest case of a single decaying state and a single decay continuum. If, however, two or more metastable states are energetically close together, they might interact and it is necessary to describe the whole manifold together. The same is true about the final states of the decay. Such situations occur frequently, e.g., in polyatomic systems where the electronic Hamiltonian depends on the positions of the nuclei and different electronic states can approach each other for specific geometries, or in atomic processes involving Rydberg series of autoionizing states [48].

To adapt the theory for the general case is in principle straightforward [34]. We start by writing the diagonal and interactions parts of the total Hamiltonian (1.1) in a matrix form,

$$\hat{H}_0 = |\phi_i\rangle E_i \langle\phi_i| + \int d\epsilon_0 \, |\boldsymbol{\phi}_d\rangle|\epsilon_0\rangle|(\boldsymbol{H}_d + \epsilon_0 \mathbb{1})\langle\epsilon_0|\langle\boldsymbol{\phi_d}| + \int d\epsilon_0 \int d\epsilon \, |\boldsymbol{\chi}(\epsilon)\rangle|\epsilon_0\rangle(\boldsymbol{H}_f + \epsilon\mathbb{1} + \epsilon_0\mathbb{1})\langle\epsilon_0|\langle\boldsymbol{\chi}(\epsilon)|, \quad (1.52a)$$

and

$$\hat{H}_I = \int d\epsilon_0 \int d\epsilon \, |\boldsymbol{\chi}(\epsilon)\rangle|\epsilon_0\rangle \boldsymbol{W}(\epsilon)\langle\epsilon_0|\langle\boldsymbol{\phi}_d| + \int d\epsilon_0 \; |\boldsymbol{\phi}_d\rangle|\epsilon_0\rangle \boldsymbol{V}(\epsilon_0) g(t) \langle\phi_i| + h.c. \quad (1.52b)$$

Here, $|\boldsymbol{\phi}_d\rangle = \{|\phi_{d_1}\rangle, |\phi_{d_2}\rangle, \dots\}^T$ is a column vector of N_d discrete states and $|\boldsymbol{\chi}(\epsilon)\rangle$ a column vector of final continuum states derived from the dicationic channels $|\chi_\alpha\rangle, \alpha = 1, \dots, N_c$. $\boldsymbol{H}_d$ and $\boldsymbol{H}_f$ are in general non-diagonal Hamiltonian matrices acting on the manifolds of the interacting metastable states and dicationic channels, respectively. The excitation operator is now represented by a column vector $\boldsymbol{V}(\epsilon_0)$ of length N_d, and $\boldsymbol{W}(\epsilon)$ is $N_c \times N_d$ matrix of discrete state-continuum coupling elements. Consequently, the system of equations (1.26) is formally the same but attains a matrix form with the coefficients $\boldsymbol{a}(\epsilon_0, t)$ and $\boldsymbol{b}(\epsilon_0, \epsilon, t)$ becoming vectors. The electron spectrum is derived analogously to the case of an isolated resonance. Special care is required, however, since the energies and coupling elements represented previously by complex numbers are replaced by matrices which, in general, do not commute.

In full analogy with the single-state case, the equation for the evolution in the manifold of the discrete states reads

$$i\dot{\boldsymbol{a}}(\epsilon_0, t) = \boldsymbol{H}_d \, \boldsymbol{a}(t) + g(t) e^{-i(E_i - \epsilon_0)t} \boldsymbol{V}(\epsilon_0) - i \int_{-\infty}^{t} d\tau \boldsymbol{\mathcal{F}}(t-\tau) \boldsymbol{a}(\epsilon_0, \tau), \quad (1.53)$$

with the memory kernel

$$\boldsymbol{\mathcal{F}}(\tau) = \int d\epsilon' \, \boldsymbol{W}^\dagger(\epsilon') e^{-i(\boldsymbol{H}_f + \epsilon')} \boldsymbol{W}(\epsilon). \quad (1.54)$$

The memory kernel is again connected through the Laplace transform with the energy-dependent level shift matrix arising in the time-independent picture [49],

$$\boldsymbol{\mathcal{F}}(E) = \lim_{\eta \to 0^+} \int d\epsilon' \, \boldsymbol{W}^\dagger(\epsilon') (E - \boldsymbol{H}_f - \epsilon' + i\eta)^{-1} \boldsymbol{W}(\epsilon'). \quad (1.55)$$

Application of the LCP approximation to the memory kernel leads to an effective Hamiltonian for the discrete states manifold [c.f. Eq. (1.33)],

$$\boldsymbol{\mathcal{H}}_d = \boldsymbol{H}_d + \boldsymbol{\Delta} - \frac{i}{2}\boldsymbol{\Gamma}, \tag{1.56}$$

where both $\boldsymbol{\Delta}$ and $\boldsymbol{\Gamma}$ are now $N_d \times N_d$ matrices. The off-diagonal elements of $\boldsymbol{\Delta}$ and $\boldsymbol{\Gamma}$ account for the so-called *via the continuum coupling*. It is an indirect interaction between the discrete states that can be visualized as a process in which one metastable state decays into the common continuum and the outgoing particle is recaptured into another discrete state.

Since we have kept the correct order of the factors during the analysis of the single state evolution, Eq. (1.38) can be readily used to give

$$\boldsymbol{b}(\epsilon, \epsilon_0, t) = -\frac{i}{\sqrt{2\pi}} e^{-i(\boldsymbol{H}_f + \epsilon)t} \int d\omega\, g(\omega) \int_{-\infty}^{t} d\tau\, e^{-i(E_i + \omega - \epsilon_0 - \boldsymbol{H}_f - \epsilon)\tau}\, \boldsymbol{W}(\epsilon)(E_i + \omega - \epsilon_0 - \boldsymbol{\mathcal{H}}_d)^{-1} \boldsymbol{V}(\epsilon_0). \tag{1.57}$$

For non-interacting decay channels with diagonal Hamiltonian, $(\boldsymbol{H}_f)_{\alpha\alpha'} = E_\alpha \delta_{\alpha\alpha'}$, the coincidence spectrum breaks into a sum of partial spectra corresponding to individual channels $|\chi_\alpha\rangle$ of the similar form as (1.40), namely

$$\begin{aligned} \sigma(\epsilon, \epsilon_0) = \lim_{t\to\infty} \boldsymbol{b}^\dagger(\epsilon, \epsilon_0, t)\boldsymbol{b}(\epsilon, \epsilon_0, t) &= \sum_\alpha \sigma_\alpha(\epsilon, \epsilon_0) \\ &= \sum_\alpha 2\pi |g(E_\alpha + \epsilon + \epsilon_0 - E_i)|^2 |\boldsymbol{W}_\alpha(\epsilon)(E_\alpha + \epsilon - \boldsymbol{\mathcal{H}}_d)^{-1} \boldsymbol{V}(\epsilon_0)|^2. \end{aligned} \tag{1.58}$$

Here, $\boldsymbol{W}_\alpha(\epsilon)$ denotes the row α of the matrix $\boldsymbol{W}(\epsilon)$. Diagonal form of the effective Hamiltonian $\boldsymbol{\mathcal{H}}_d$ acting on the discrete states manifold, on the other hand, leads to no such simplification. While non-interacting final states contribute incoherently to the decay spectrum, $\boldsymbol{b}(\epsilon, t)$ of Eq. (1.58) is always a coherent superposition of contributions from individual metastable states [34].

It turns out that the least straightforward step in the above procedure is a consistent definition of the LCP approximation. It is notable that, despite the fact that the existence of a suitable LCP approximation is commonly assumed for interacting resonances, the literature discussing the peculiarities of its definition is rather sparse. The most relevant works are those of Estrada *et al* [49] and more recently of Feuerbacher and coworkers [50]. Both authors consider primarily the more general problem involving nuclear degrees of freedom but, as pointed out by Estrada, it is instructive to discuss the problem already in the fixed-nuclei limit.

Let us start by the analysis of the form of the level shift (1.55). As for the decay spectra, the formula can be simplified if we assume non-interacting decay channels and thus diagonal $\boldsymbol{H}_f$. The level shift matrix then reduces to

$$\boldsymbol{\mathcal{F}}(E) = \boldsymbol{\Delta}(E) - \frac{i}{2}\boldsymbol{\Gamma}(E) = \sum_\alpha \boldsymbol{\Delta}_\alpha(E - E_\alpha) - \frac{i}{2}\sum_\alpha \boldsymbol{\Gamma}_\alpha(E - E_\alpha) \tag{1.59a}$$

with the decay width and level shift matrices given by (no summation over α implied)

$$\boldsymbol{\Gamma}_\alpha(\epsilon) = 2\pi \boldsymbol{W}_\alpha^\dagger(\epsilon)\boldsymbol{W}_\alpha(\epsilon), \qquad \boldsymbol{\Delta}_\alpha(\epsilon) = \mathcal{P}\int d\epsilon' \, \frac{\boldsymbol{W}_\alpha^\dagger(\epsilon')\boldsymbol{W}_\alpha(\epsilon')}{\epsilon - \epsilon'}. \tag{1.59b}$$

The diagonal element $[\boldsymbol{\Gamma}_\alpha(\epsilon)]_{ll}$ of the decay width matrix can be interpreted as the partial decay width of the metastable state l into the (non-interacting) channel α. From Eq. (1.58) we see that the partial widths determine the population of individual decay channels. In the case that the non-interacting channels have been obtained by a unitary transformation (prediagonalization) of interacting decay continua, it is still possible to extract partial decay widths associated with the original decay channels but the formula becomes more involved [51].

Having recovered the standard form of the level shift matrix, Eq. (1.59), we can now proceed to the definition of the LCP approximation, which involves replacing the complex symmetric and energy dependent Hamiltonian,

$$\boldsymbol{\mathcal{H}}_d(E) = \boldsymbol{H}_d + \boldsymbol{\mathcal{F}}(E), \tag{1.60}$$

by a suitable energy independent matrix. In the previous sections, we have learned that LCP can be defined by evaluating the level shift function at the energy corresponding to either the K-matrix or the T-matrix pole. Let us consider first the latter option which we find more straightforward for multiple discrete states. Definition of LCP through the poles of the K-matrix leads to similar complications [49] and will be commented upon later.

Lets assume for the arguments sake that the discrete state manifold contains two states, $N_d = 2$. Matrix analog of Eq. (1.18) for the poles of the T-matrix reads

$$\det\left[\boldsymbol{\mathcal{H}}_d(Z_{res}^{(l)}) - Z_{res}^{(l)}\mathbb{1}\right] = 0. \tag{1.61}$$

Assuming that each discrete state generates one pole, this equation has two solutions, $Z_{res}^{(1)}$ and $Z_{res}^{(2)}$. It is immediately clear that straightforward generalization of the single state approach and setting $\boldsymbol{\mathcal{H}}_d^{loc} = \boldsymbol{\mathcal{H}}_d(Z_{res})$ is not possible for multiply-valued Z_{res}. Neither is it correct to use different complex pole energies to evaluate individual matrix elements of $\boldsymbol{\mathcal{H}}_d^{loc}$. For interacting resonances, there is no simple one-to-one correspondence between the poles and the original discrete states, and it is not clear how such a substitution should be made in the off-diagonal elements.

Instead, we take as the starting point of the LCP approximation the diagonal matrix

$$\boldsymbol{\mathcal{H}}_d^{diag} = \mathrm{diag}\left(Z_{res}^{(1)}, Z_{res}^{(2)}\right). \tag{1.62}$$

This matrix represents the desired constant effective Hamiltonian of Eq. (1.56) but not in the representation the two initially chosen discrete states, $|\phi_{d_1}\rangle$ and $|\phi_{d_2}\rangle$. Furthermore, it does not arise as a unitary transformation of a single Hamiltonian matrix expressed in that basis [49]. Indeed, it follows from Eq. (1.61) that the two complex resonance energies, $Z_{res}^{(1)}$ and $Z_{res}^{(2)}$, are obtained as eigenvalues of two different complex symmetric matrices, $\boldsymbol{\mathcal{H}}_d(Z_{res}^{(1)})$

and $\boldsymbol{\mathcal{H}}_d(Z_{res}^{(2)})$. The second eigenvalue of each matrix does not correspond to a resonance pole and is irrelevant for the construction of LCP. Consequently, the two eigenvectors corresponding to the relevant eigenvalues of each matrix are not orthogonal,[7] and thus together they do not define an unitary transformation between the original discrete states and the representation of the diagonal Hamiltonian (1.62).

With no better option at hand, we suggest that the two vectors can nevertheless be used to transform $\boldsymbol{\mathcal{H}}_d^{diag}$ back to the original basis and construct the sought LCP Hamiltonian. We thus define the transformation matrix as

$$\boldsymbol{S}_T = \left(\boldsymbol{v}_T^{(1)}, \boldsymbol{v}_T^{(2)}\right), \tag{1.63}$$

where $\boldsymbol{v}_T^{(1)}$ and $\boldsymbol{v}_T^{(2)}$ are column eigenvectors of $\boldsymbol{\mathcal{H}}_d(Z_{res}^{(1)})$ and $\boldsymbol{\mathcal{H}}_d(Z_{res}^{(2)})$, respectively, each associated with the eigenvalue corresponding to the T-matrix pole. The LCP Hamiltonian,

$$\boldsymbol{\mathcal{H}}_d^{loc} = \boldsymbol{S}_T^{-1} \boldsymbol{\mathcal{H}}_d^{diag} \boldsymbol{S}_T, \tag{1.64}$$

is then represented by a complex non-Hermitian matrix with the same spectrum as $\boldsymbol{\mathcal{H}}_d^{diag}$. Therefore, if substituted for the energy-dependent $\boldsymbol{\mathcal{H}}_d(E)$ in the formula for the T-matrix, it reproduces the correct positions of the poles. Transformation as close as possible to the original basis of the discrete states manifold ensures that also the residua are approximated satisfactorily. This in turn results to an adequate description of the physical process, as the decay transition is dominated by the behavior of the T-matrix around its singular points.

Construction of the LCP approximation through the poles of the K-matrix is analogous but brings about an additional ambiguity [49]. The poles are defined by the matrix equation

$$\det\left[\boldsymbol{H}_d + \boldsymbol{\Delta}(E_{res}^{(l)}) - E_{res}^{(l)}\mathbb{1}\right] = 0 \tag{1.65}$$

and are thus given by eigenvalues of the real part of the effective Hamiltonian $\boldsymbol{\mathcal{H}}_d(E)$, evaluated at two different real energies. In the representation of the corresponding eigenvectors, $\boldsymbol{v}_K^{(1)}$ and $\boldsymbol{v}_K^{(2)}$, we obtain diagonal real part of the sought LCP Hamiltonian.[8] Unlike the previous method, however, this approach does not provide automatically the corresponding representation of the decay width matrix $\boldsymbol{\Gamma}$, and there is no unique way to define it since it is in general non-diagonal even in the representation of the eigenvectors $\boldsymbol{v}_K^{(l)}$. One possible approach is to transform the

[7] For complex symmetric matrices, the orthogonality is defined with respect to the inner c-product [52] in which the bra-vector is not complex conjugate. In general, the ket and bra eigenstates are associated with right end left eigenvectors of the matrix, respectively. The left eigenvectors, which form *dual basis* to the set of right eigenvectors, are equal to the right eigenvectors of the transposed matrix. For a Hermitian matrix, the left eigenvectors are thus obtained from right eigenvectors through transposition and complex conjugation while for a complex symmetric matrix through transposition only. Discussion of the problems associated with potential incompletness of the spectrum of non-Hermitian operators can be found, e.g., in Ref. [53].

[8] Again, the two eigenvectors of different real symmetric matrices are not orthogonal, the orthogonality being defined with respect to standard scalar product.

coupling matrix $\boldsymbol{W}(\epsilon)$ into the new basis as

$$\boldsymbol{W}_K(\epsilon) = \boldsymbol{W}(\epsilon)\boldsymbol{S}_K^{-1}, \qquad \boldsymbol{S}_K = \left(\boldsymbol{v}_K^{(1)}, \boldsymbol{v}_K^{(2)}\right). \tag{1.66a}$$

Individual columns of $\boldsymbol{W}_K(\epsilon)$ now correspond to discrete states defined by the vectors $\boldsymbol{v}_K^{(l)}$, and it is thus appropriate to evaluate them at the respective resonance energies $E_{res}^{(l)}$,

$$[\boldsymbol{W}_K]_{\alpha l} = [\boldsymbol{W}_K(E_{res}^{(l)} - E_\alpha)]_{\alpha l}. \tag{1.66b}$$

The decay width matrix is then naturally constructed as

$$\boldsymbol{\Gamma}_K = 2\pi \boldsymbol{W}_K^\dagger \boldsymbol{W}_K \tag{1.67}$$

and the desired LCP Hamiltonian in the original basis is obtained as

$$\boldsymbol{\mathcal{H}}_d^{loc} = \boldsymbol{S}_K^{-1}\left[\mathrm{diag}\left(E_{res}^{(1)}, E_{res}^{(2)}\right) - \frac{i}{2}\boldsymbol{\Gamma}_K\right]\boldsymbol{S}_K. \tag{1.68}$$

The soundness of the above constructions rests on the same assumption that is vital for the LCP approximation to be applicable already in the single state case, i.e., on a weak energy dependence of the discrete state-continuum coupling elements and thus of $\boldsymbol{\mathcal{H}}_d(E)$ itself. For the metastable states to interact strongly, they have to be energetically close and thus the Hamiltonian matrix evaluated at the two resonance energies will be similar, leading to nearly orthogonal pair of eigenvectors $\boldsymbol{v}_{T/K}^{(1)}$ and $\boldsymbol{v}_{T/K}^{(2)}$. Still, the non-orthogonality leads to a qualitative difference between $\boldsymbol{\mathcal{H}}_d(E)$ and its LCP approximation – the latter is in general non-symmetric. Symmetry can in principle be restored by performing symmetric orthogonalization of the two eigenvectors forming the transformation matrix $\boldsymbol{S}_{T/K}$. Model studies suggest that, concerning the resulting decay spectra, the difference between symmetrized and non-symmetrized LCP is typically smaller than the error introduced by the LCP approximation itself. In other contexts, the symmetry of the approximate Hamiltonian might be more critical. The problem thus requires further study which is beyond the scope of the present work.

Model example

To illustrate the effects of interacting resonances and the properties of the LCP approximation, we use a simple model of two metastable states decaying into a single continuum, with the discrete state-continuum coupling described by the formula

$$W_l(\epsilon) = \sqrt{A_l}\epsilon^{\alpha/2}e^{-\beta_l\epsilon}. \tag{1.69}$$

This model is adopted from Refs. [27, 54] and is often used to study low-energy resonances and threshold effects in electron-molecule scattering [55, 56]. In the present work, we do not

attempt to simulate any realistic system, the choice of the model is motivated primarily by the possibility to evaluate the real level shift $\mathbf{\Delta}(E)$ in Eq. (1.59) analytically as

$$\Delta_l(\epsilon) = \begin{cases} -A_l(-\epsilon)^\alpha e^{-2\beta_l\epsilon}\Gamma(1+\alpha)\Gamma(-\alpha,-2\beta_l\epsilon) & \epsilon < 0 \\ A_l\epsilon^\alpha e^{-2\beta_l\epsilon}\left[\pi\cot\pi\alpha + e^{i\pi\alpha}\Gamma(1+\alpha)[\Gamma(-\alpha)-\Gamma(-\alpha,-2\beta\epsilon)]\right] & \epsilon > 0 \end{cases}, \tag{1.70}$$

where $\Gamma(\alpha, x)$ is the incomplete gamma function. In the following, the two discrete states are defined by the numerical values $E_{d_1} = 5.5$, $A_1 = 1.5$, $\beta_1 = 0.25$, and $E_{d_2} = 6$, $A_2 = 2$, $\beta_2 = 1/3$. The threshold exponent $\alpha = 3/2$ corresponds to an outgoing p-wave electron but is also chosen rather arbitrarily. The threshold energy E_f is set to zero.

We start by investigating the two resonances individually, i.e., neglecting their mutual interaction. Decay widths and real level shifts for the chosen values of parameters are shown in the left panel of Fig. 1.1. The respective positions of resonance poles are shown in the first row of Tab. 1.1. In the right panel of the figure, we plot the decay spectra resulting from each metastable state. Full lines show exact spectra obtained from Eq. (1.16). In both cases the line profiles are slightly asymmetric Lorentzian shapes, narrowing on the high-energy side due to the decreasing coupling functions $W_l(\epsilon)$. Broken lines result from the LCP approximation (1.41) derived from the poles of the K-matrix (dashed) and of the T-matrix (dashed-dotted). We see that LCP is an adequate description for both resonances. The two variants of the LCP approximation result into only very small shift of the peaks towards lower energies (K-matrix poles) or slight deviation of the relative intensities (T-matrix poles). These inaccuracies are to be attributed to the appreciable dependence of the decay width functions on energy in the relevant range. For completeness, we also show in the figure the summed spectrum (black line) that would arise from equal initial population of the two non-interacting metastable states.

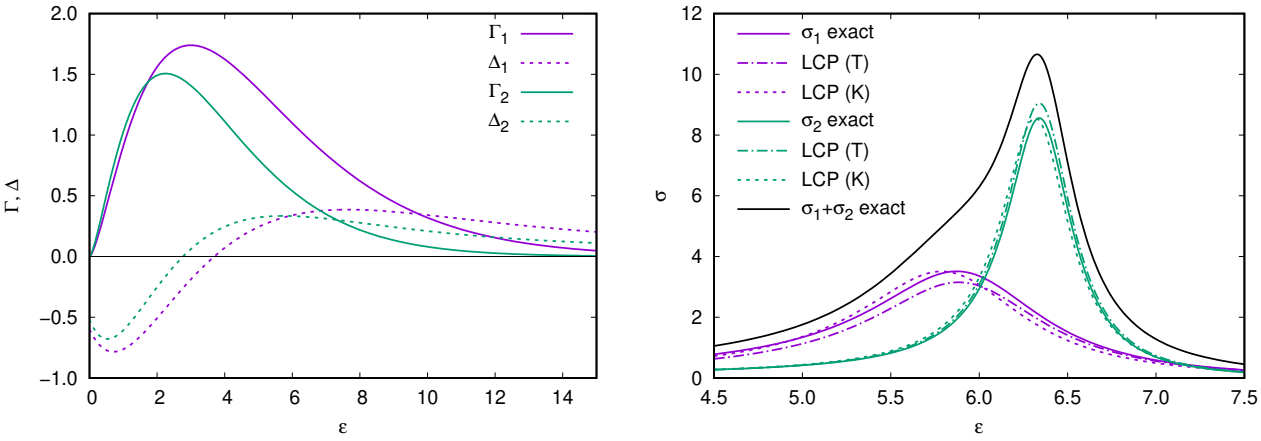

Figure 1.1: Left panel: diagonal elements of the decay width and level shift matrices. **Right panel:** decay spectra calculated for each resonance independently, neglecting their interaction. Full lines show exact results while broken lines correspond to the LCP approximations: dashed-dotted – defined by the positions of the T-matrix, Eq. (1.18); dashed – defined by the positions of the K-matrix, Eq. (1.17). Solid black line represents the summed spectrum that would result from equal initial population of the two non-interacting metastable states.

type of interaction	$Z_{res}^{(1)}$	$E_{res}^{(1)} - i\Gamma(E_{res}^{(1)})/2$	$Z_{res}^{(2)}$	$E_{res}^{(2)} - i\Gamma(E_{res}^{(2)})/2$
no interaction	$5.928 - 0.597i$	$5.828 - 0.573i$	$6.351 - 0.227i$	$6.329 - 0.234i$
continuum only	$5.762 - 0.105i$	$5.647 - 0.209i$	$6.574 - 0.583i$	$6.517 - 0.542i$
continuum & direct	$5.229 - 0.074i$	$5.186 - 0.095i$	$7.056 - 0.507i$	$6.975 - 0.533i$

Table 1.1: Complex resonance energies Z_{res} of Eq. (1.18) and E_{res} of Eq. (1.17) with the corresponding decay widths $\Gamma(E_{res})$ for the model system. First row shows poles associated with the two discrete states when all interaction between the discrete states is neglected. In the second row, coupling through the continuum is taken into account. In the third row, additional direct coupling $U = \langle\phi_{d_1}|H_d|\phi_{d_2}\rangle = 1/2$ is included.

In the next step, we take into account the *via the continuum* coupling stemming from the off-diagonal elements of the level shift matrix (1.55). Shifted positions of the resonance poles are given in the second line of Tab. 1.1. It is remarkable that the values of the imaginary parts of the resonance poles (i.e., the decay widths of the two resonances) have been approximately interchanged, but that is mostly coincidental. The more important observation is that the resonance poles can no longer be associated with the original discrete states. In fact, assuming an equal initial population of $|\phi_{d_1}\rangle$ and $|\phi_{d_2}\rangle$ with the same phase means that the wider resonance associated with the higher-energy pole $E_{res}^{(2)}$ acquire more than 90% of intensity, resulting into the decay spectrum dominated by the corresponding broad structure, as shown in the left panel of Fig. 1.2. Mixing the two discrete states with the opposite phase populates dominantly the lower-energy resonance and results into a single narrow Lorentzian peak centered around $\epsilon \approx 5.7$ (shown in the inset of the plot).

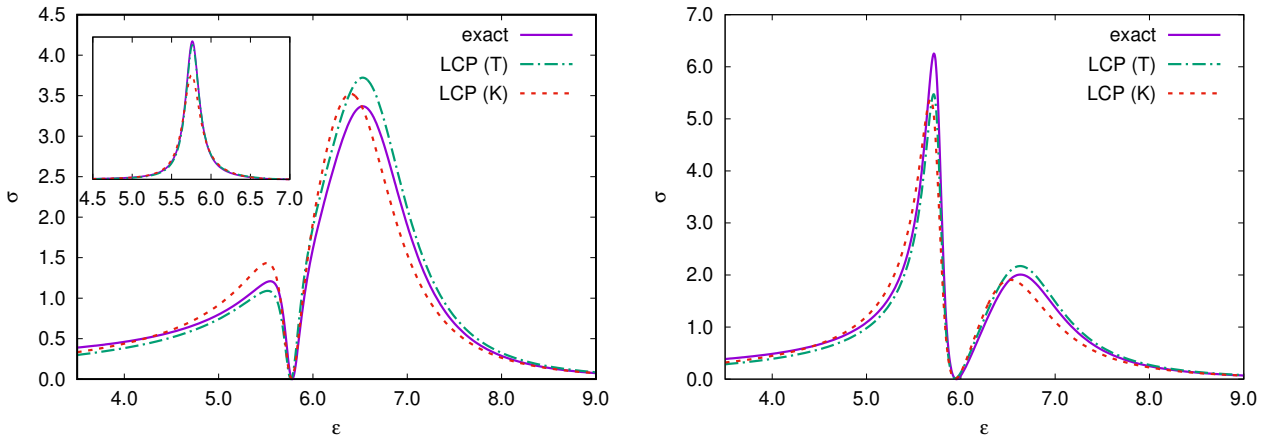

Figure 1.2: Decay spectra for the two-state model with full account for the *via the continuum* coupling. **Left panel:** uniform initial population of the discrete states with equal (main plot) and opposite phase (inset). **Right panel:** uniform initial population of the resonance states associated with the K-matrix poles shown in Tab. 1.1. In both panels, full purple curve shows the exact solution (1.58) while dahed-dotted green and dotted red lines correspond to the LCP approximations based on the T-matrix poles and K-matrix, respectively.

The right panel of Fig. 1.2 shows spectrum resulting from equal population of the two resonances rather than the original discrete states, i.e., the entry amplitude in Eq. (1.58) is given as a sum of the eigenvectors corresponding to individual resonance poles,

$$\boldsymbol{V}(\epsilon_0) = \boldsymbol{v}_K^{(1)} + \boldsymbol{v}_K^{(2)}. \tag{1.71}$$

In this case, the two peaks associated with individual resonances are formed, but the Lorentzian profiles are significantly deformed by the mutual interaction. In both panels of the figure, the spectra calculated using the two variants of the LCP approximation, defined by Eqs. (1.64) and (1.68), are shown by green and red broken lines, respectively.[9] Both variants show minor imperfections, but correctly reproduce all features of the spectra regardless the initial population. In particular, all the exact and approximate spectra comply with the general result of Fano that the transition amplitude vanishes once in each interval between two neighbouring resonances [25].

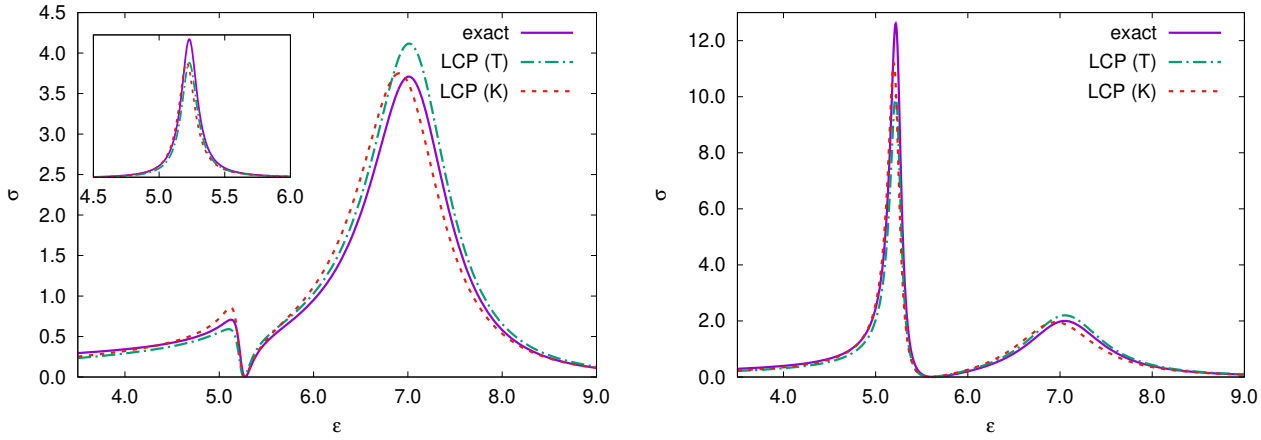

Figure 1.3: Decay spectra for the two-state model with full account for the *via the continuum* coupling and with additional direct coupling $\langle\phi_{d_1}|H_d|\phi_{d_2}\rangle = 1/2$ between the two discrete states. **Left panel:** uniform initial population of the discrete states with equal (main plot) and opposite phase (inset). **Right panel:** uniform initial population of the resonance states associated with the K-matrix poles shown in Tab. 1.1. In both panels, full purple curve shows the exact solution (1.58) while dashed-dotted green and dotted red lines correspond to the LCP approximations based on the T-matrix poles and K-matrix, respectively.

Increasing further the complexity of the problem, we incorporate the direct coupling between the discrete states through off-diagonal elements of the Hamiltonian $\boldsymbol{H}_d$,

$$\langle\phi_{d_1}|\boldsymbol{H}_d|\phi_{d_2}\rangle = 1/2. \tag{1.72}$$

The chosen value is comparable in strength to the indirect coupling through the continuum. As can be seen from the third row of Tab. 1.1, the two resonance poles are pushed further apart and the lower resonance narrows considerably. As a result, the overlap between the resonances is significantly reduced and the mutual interaction is thus much weaker. Resulting

[9] Thorough this subsection, we use non-symmetric LCP Hamiltonians. For this particular model, symmetrization does not change the results appreciably.

decay spectra are shown in Fig. 1.3 in the same format as before. Left panel results from uniform population of the original discrete states with equal (main plot) and opposite phases (inset), corresponding to dominant excitation of the broad and narrow resonances, respectively. Right panel then shows the spectrum resulting from uniform population of the two resonances directly associated with the poles of the K-matrix. Due to the weaker interaction, the latter is closer to a sum of two Lorentzian profiles, although the narrow line in particular is still visibly asymmetric.

Performance of the LCP approximations is similar to the previous case. This is not surprising. In fact, in the fixed nuclei limit, there is no qualitative difference between diagonal and non-diagonal Hamiltonian in the discrete states manifold – it is always possible to diagonalize it first by means of a unitary transformation (note that $\boldsymbol{H}_d$ is Hermitian) without any loss of information or generality. The significance of non-diagonal $\boldsymbol{H}_d$ will become apparent in the following section in which we take into account nuclear motion and introduce adiabatic and diabatic electronic basis sets. The coupling of electronic states then originates from the operator of the kinetic energy of the nuclei and cannot be transformed out in principle.

Through the present section, the LCP decay spectra were computed using the formula (1.58) with correct energy-dependent coupling $\boldsymbol{W}(\epsilon)$ in the numerator, which is equivalent to the semi-local approximation of Cederbaum and Domcke [40]. In the simpler, boomerang model-like local approximation, the exit amplitude $\boldsymbol{W}^{loc}$ is constant and is derived from the imaginary part of the diagonal matrix elements of the LCP Hamiltonian. It typically results into a more symmetric spectral features as the approach does not account for the variation of the exit amplitude with increasing energy. For the presented models, however, the results are very similar to those shown and we will not pursue this discussion further.

To conclude, we have demonstrated that even in the case of strongly interacting resonances it is possible to consistently define LCP approximation which correctly accounts for all aspects of the decay process. More thorough discussion of its reliability, in particular if it has to be constructed without the complete information encoded in the energy-dependent discrete state-continuum couplings, is beyond the scope of this work.

1.5 Introducing nuclear dynamics

The theory presented in this chapter so far is directly applicable to the description of decay processes in isolated atoms. It can also be used for polyatomic systems if the decay lifetime is much shorter than the characteristic times associated with nuclear motion, which is often but not necessarily the case for Auger or Coster-Kronig transitions in molecules. For interatomic decay processes in weakly bound aggregates, however, this condition is seldom fulfilled. Therefore, in the present section, we include nuclear degrees of freedom among the dynamical variables.

The problem was formulated in both the time-dependent [34, 57, 58] and time-independent

[34,35] frameworks. We adopt the time-dependent approach to provide a more intuitive understanding. To account for the nuclear motion, the purely electronic Hamiltonian (1.1) has to be augmented by the operator $\hat{T}_N$ of the kinetic energy of the nuclei. The full Hamiltonian thus reads

$$\hat{H} = \hat{T}_N + \hat{H}_{el}(\boldsymbol{r};\boldsymbol{Q}) + \hat{V}(\boldsymbol{r},\boldsymbol{Q},t), \tag{1.73}$$

where we assume the excitation operator to be time-dependent and of the form (1.23) describing the interaction of the system with an electromagnetic field in the dipole approximation. We have also explicitly indicated the dependence of the Hamiltonian operator on the nuclear and electronic coordinates, collectively designated by $\boldsymbol{Q}$ and $\boldsymbol{r}$, respectively.

Within the Born representation [59], the total time-dependent wave function $\Psi(\boldsymbol{r},\boldsymbol{Q},t)$ factorizes as

$$\Psi(\boldsymbol{r},\boldsymbol{Q},t) = \sum_j \phi_j(\boldsymbol{r};\boldsymbol{Q})\psi_j(\boldsymbol{Q},t), \tag{1.74}$$

where $\psi_j(\boldsymbol{Q},t)$ describes the nuclear motion in the specific electronic state represented by the wave function $\phi_j(\boldsymbol{r};\boldsymbol{Q})$. The latter constitute a time-independent basis in the electronic Hilbert space, which is only parametrically dependent on the nuclear coordinates. The correspondence with the fixed-nuclei limit presented in Sec. 1.2 is evident through the comparison of this ansatz with the expansion (1.25). The electronic states $|\phi_j(\boldsymbol{Q})\rangle$ correspond to the basis of $|\phi_i\rangle$, $|\phi_d\rangle|\epsilon_0\rangle$, and $|\chi(\epsilon)\rangle|\epsilon_0\rangle$, while the nuclear wave packets $|\psi_j(t)\rangle$ play the role of the respective time-dependent expansion coefficients.[10]

Construction of an appropriate basis of electronic states is critical for an efficient solution of the dynamical problem, as well as for intuitive understanding of the physics. An obvious choice comprises *adiabatic* stationary states obtained as solutions of the electronic time-independent Schrödinger equation for each geometry,

$$\hat{H}_{el}(\boldsymbol{Q})|\phi_j^{ad}(\boldsymbol{Q})\rangle = E_j^{ad}(\boldsymbol{Q})|\phi_j^{ad}(\boldsymbol{Q})\rangle, \tag{1.75}$$

but other alternatives might be preferable in many situations. Therefore, for the time being, we will consider $|\phi_j(\boldsymbol{Q})\rangle$ to be some convenient orthogonal basis, not necessarily adiabatic, which reflects the physical characteristics of the states involved in the studied process.

Inserting the expansion (1.74) into the time-dependent Schrödinger equation with the Hamiltonian (1.73) and projecting onto the individual electronic states $|\phi_j(\boldsymbol{Q})\rangle$, we obtain a set of coupled differential equations which can be cast into the matrix form[11]

$$i\frac{\partial}{\partial t}|\boldsymbol{\psi}(t)\rangle = \left[\hat{T}_N\mathbb{1} + \boldsymbol{U} + \hat{\boldsymbol{\Lambda}} + \boldsymbol{V}(t)\right]|\boldsymbol{\psi}(t)\rangle. \tag{1.76}$$

[10] We denote the electronic states parametrically dependent on the nuclear coordinates as $|\phi_j(\boldsymbol{Q})\rangle$ and the respective wave functions in (electronic) coordinate representation as $\phi_j(\boldsymbol{r};\boldsymbol{Q}) = \langle\boldsymbol{r}|\phi_j(\boldsymbol{Q})\rangle$. Likewise for the nuclear wavepackets, $|\psi_j(\boldsymbol{Q},t)\rangle = \langle\boldsymbol{Q}|\psi_j(t)\rangle$. $|\boldsymbol{r}\rangle$ and $|\boldsymbol{Q}\rangle$ are eigenstates of the respective position operators.

[11] By the circumflex we distinguish differential operators from complex numbers or matrices.

We have introduced the column vector of nuclear wave packets $|\boldsymbol{\psi}(t)\rangle_j = |\psi_j(t)\rangle$, the potential energy matrix $\boldsymbol{U}$ with elements in the coordinate representation

$$U_{jk}(\boldsymbol{Q}) \equiv \langle \boldsymbol{Q}|U_{jk}|\boldsymbol{Q}'\rangle = \langle \phi_j(\boldsymbol{Q})|\hat{H}_{el}(\boldsymbol{Q})|\phi_k(\boldsymbol{Q})\rangle \delta(\boldsymbol{Q}-\boldsymbol{Q}'), \tag{1.77a}$$

and the corresponding matrix of the excitation operator with elements

$$V_{jk}(\boldsymbol{Q}) \equiv \langle \boldsymbol{Q}|V_{jk}(t)|\boldsymbol{Q}'\rangle = \langle \phi_j(\boldsymbol{Q})|\hat{V}(t)|\phi_k(\boldsymbol{Q})\rangle \delta(\boldsymbol{Q}-\boldsymbol{Q}'). \tag{1.77b}$$

The operator $\hat{\boldsymbol{\Lambda}}$ stands for the so-called non-adiabatic (also *vibronic*) coupling which stems from the parametric dependence of the electronic basis on the nuclear coordinates. Its elements can be written as [60]

$$\hat{\Lambda}_{jk}(\boldsymbol{Q}) = \langle \phi_j(\boldsymbol{Q})|\hat{T}_N|\phi_k(\boldsymbol{Q})\rangle - \hat{T}_N\delta_{jk}. \tag{1.78}$$

For the adiabatic electronic basis defined by Eq. (1.75), the potential energy matrix $\boldsymbol{U}(\boldsymbol{Q})$ is diagonal,

$$U^{ad}_{jk}(\boldsymbol{Q}) = E^{ad}_j(\boldsymbol{Q})\delta_{jk} \tag{1.79}$$

and, in the absence of the external field, the nuclear wave packets $|\psi_j(t)\rangle$ are coupled only by the non-adiabatic coupling. If the electronic states are energetically well separated, the off-diagonal coupling matrix elements $\hat{\Lambda}_{jk}$ can be neglected, which constitute the *Born-Oppenheimer (BO) approximation* [50,59]. In the *adiabatic BO approximation*, diagonal elements $\hat{\Lambda}_{jj}$ are neglected as well. Individual nuclear wave packets then evolve on their respective adiabatic potential energy surfaces (PES) defined by the diagonal elements (1.79) of the potential energy matrix, and can interact only through the excitation operator $\hat{\boldsymbol{V}}$.

The BO approximation breaks down if PESs of two or more electronic states approach each other. The non-adiabatic couplings might become significant, and the vibrational wave packets in different electronic states can no longer be treated separately. In such a case, *diabatic* electronic basis [60,61] is often more appropriate since it allows to describe the coupling between nuclear wave packets via the potential matrix rather than via momenta through the complicated operator $\hat{\boldsymbol{\Lambda}}$ [50]. The diabatic basis $|\phi^{dia}_j(\boldsymbol{Q})\rangle$ is connected with the adiabatic one by a unitary transformation and is defined by the condition $\hat{\Lambda}_{jk} = 0$, i.e.,

$$\langle \phi^{dia}_j(\boldsymbol{Q})|\hat{T}_N|\phi^{dia}_k(\boldsymbol{Q})\rangle = \hat{T}_N\delta_{jk}. \tag{1.80}$$

Mead and Truhlar have shown [62] that a strictly diabatic basis exists only for diatomic systems with one relevant degree of freedom, the internuclear distance. In other cases, the condition (1.80) can be satisfied only approximately. Generally, however, sufficiently high accuracy can be achieved, and the residual couplings can be neglected [50,62]. In the diabatic representation, the potential energy matrix $\boldsymbol{U}(\boldsymbol{Q})$ is no longer diagonal. Nevertheless, we will speak of its diagonal elements as PESs corresponding to the diabatic electronic states. Indeed, for most geometries, the diabatic states coincide with the adiabatic ones, and the couplings are significant only in regions where the adiabatic PESs get very close in energy.

Within this framework, the inner-shell ionization or excitation and the subsequent decay process can be visualized as a series of transitions of the nuclear wave packet between PESs corresponding to different electronic states. An example is given in Fig. 1.4, where the sequence is depicted for the prototypical ICD in the neon dimer (cf. Fig. 1). Initially, the system is assumed to be in the ground electronic state $|\phi_i(R)\rangle$ (R is the internuclear distance) of the neutral N-electron system. The corresponding PES $U_i(R)$ for the weakly bound van der Waals system is characterized by a shallow minimum and a rather large equilibrium interatomic distance. Instantaneous broadband photoionization induces vertical transition of the vibrational wave packet into the inner-valence ionized $(N-1)$-electron metastable state $|\phi_d(R)\rangle$, associated with the inner-valence vacancy state $\mathrm{Ne}^+(2s^{-1})$-Ne. This transition is is accompanied by ejection of the primary photoelectron. The binding energy is larger in the ionized dimer, and the nuclear wave packet is thus driven towards shorter internuclear distances. It simultaneously decays via ICD, ejecting the secondary electron with energy ϵ.

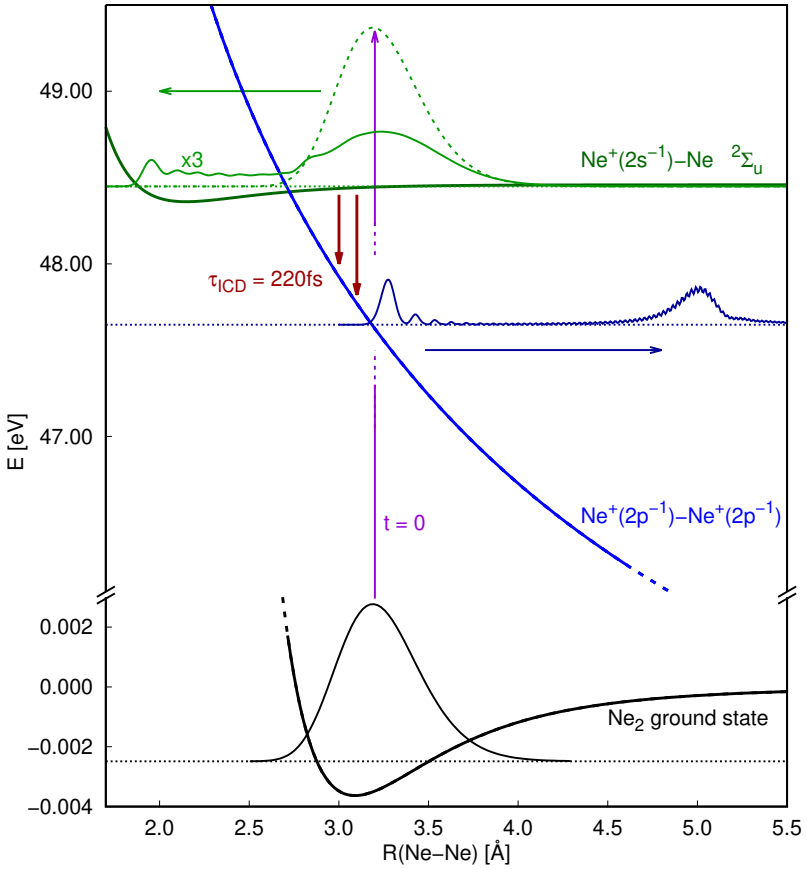

Figure 1.4: Born-Oppenheimer picture of ICD in Ne_2. Black: PES of the neutral dimer with the ground state vibrational wave packet $|\psi_i(R,t)\rangle$. Green: intermediate $\mathrm{Ne}^+(2s^{-1})$-Ne $^2\Sigma_u$ metastable state PES with a snapshot of the wave packet $|\psi_d(R,t)\rangle$ ($t = 170\,\mathrm{fs}$). Blue: repulsive ICD final state $\mathrm{Ne}^+(2p^{-1})$-$\mathrm{Ne}^+(2p^{-1})$ PES with a snapshot of the dissociating wave packet $|\psi_f(\epsilon,R,t)\rangle$ ($\epsilon = 0.6\,\mathrm{eV}$, $t = 83\,\mathrm{fs}$). At the equilibrium interatomic distance, the lifetime of the $\mathrm{Ne}^+(2s^{-1})$-Ne state is about 220 fs (symmetry-averaged, calculated by the Fano-ADC(2,2) method [A1]), consistent with the value of 150 ± 50 fs value extracted from the pump-probe experiment by Schnorr *et al.* [6].

The manifold of final doubly ionized states is characterized by two outer-valence $2p$ vacancies distributed over both atoms. Corresponding PESs $U_f(R)$ are thus dominated by Coulomb repulsion between the two positive charges, leading to dissociation of the doubly-ionized dimer. The geometry at which the electronic transition occurs dictates the partition of the excitation energy between the secondary electron and the ionic fragments; the shorter the internuclear distance, the stronger the Ne^+–Ne^+ repulsion, resulting in higher kinetic energy carried away by the ionic fragments and lower energy ϵ of the emitted electron.

The nuclear dynamics thus determine the kinetic energy release (KER)[12] and ICD electron energy spectra, $\sigma_{\mathrm{KER}}(E_{\mathrm{KER}})$ and $\sigma_e(\epsilon)$. If the nuclear motion were classical, the KER spectrum would be given by the mirror image of the electron spectrum, $\sigma_{\mathrm{KER}}(E_{\mathrm{KER}}) = \sigma_e(E_{\mathrm{tot}} - E_{\mathrm{KER}} - U_f^\infty)$. This relationship follows from the local nature of the classical dynamics and conservation of the total excitation energy, $E_{\mathrm{tot}} = \epsilon + E_{\mathrm{KER}} + U_f^\infty$. Here, $U_f^\infty = U_f(R \to \infty)$ denotes the threshold energy. Even though it often holds to a good approximation even in the quantum world, exact treatment shows that the two spectra in principle carry complementary information on the decay process and might deviate significantly from the mirror image relation [63].

To derive explicit formulae for the decay products spectra, we consider the general situation discussed in Sec. 1.4 involving a single initial N-electron state $|\phi_i(\boldsymbol{Q})\rangle$, manifold of N_d intermediate metastable cationic states $|\phi_{d_l}(\boldsymbol{Q})\rangle$, and N_c dicationic decay channels $|\chi_\alpha(\boldsymbol{Q})\rangle$. Energy-normalized $N-1$–electron final states correlating with dicationic channel α and secondary continuum electron with energy ϵ are denoted $|\chi_\alpha(\epsilon, \boldsymbol{Q})\rangle$. The system of differential equations (1.76) describing the evolution of the nuclear wave packets in their respective electronic states then assumes a matrix form with the same structure as Eqs. (1.26), namely [36,58]

$$i\frac{\partial}{\partial t}|\psi_i(t)\rangle = \hat{H}_i|\psi_i(t)\rangle + g^*(t)\int d\epsilon_0\, \boldsymbol{V}^\dagger(\epsilon_0)e^{-i\epsilon_0 t}|\boldsymbol{\psi}_d(t)\rangle, \tag{1.81a}$$

$$i\frac{\partial}{\partial t}|\boldsymbol{\psi}_d(\epsilon_0,t)\rangle = \hat{\boldsymbol{H}}_d|\boldsymbol{\psi}_d(\epsilon_0,t)\rangle + g(t)\boldsymbol{V}(\epsilon_0)e^{i\epsilon_0 t}|\psi_i(t)\rangle + \int d\epsilon\, \boldsymbol{W}^\dagger(\epsilon)|\boldsymbol{\psi}_f(\epsilon,\epsilon_0,t)\rangle, \tag{1.81b}$$

$$i\frac{\partial}{\partial t}|\boldsymbol{\psi}_f(\epsilon,\epsilon_0,t)\rangle = [\hat{\boldsymbol{H}}_f + \epsilon\mathbb{1}]|\boldsymbol{\psi}_f(\epsilon,\epsilon_0,t)\rangle + \boldsymbol{W}(\epsilon)|\boldsymbol{\psi}_d(\epsilon_0,t)\rangle. \tag{1.81c}$$

Here, $|\boldsymbol{\psi}_d(t)\rangle$ and $|\boldsymbol{\psi}_f(t)\rangle$ are column vectors whose elements are nuclear wave packets associated with the N-electron states $|\phi_{d_l}(\boldsymbol{Q})\rangle|\epsilon_0\rangle$ and $|\chi_\alpha(\epsilon,\boldsymbol{Q})\rangle|\epsilon_0\rangle$, respectively.[13]

The Hamiltonian operators

$$\hat{\boldsymbol{H}}_X \equiv \hat{T}_N\mathbb{1} + \boldsymbol{U}_X, \qquad X = i, d, f, \tag{1.82}$$

play the role of E_i, $\boldsymbol{H}_d$ and $\boldsymbol{H}_f$ from the previous section, but comprise also the operator of the nuclear kinetic energy. We assume diabatic electronic basis and the residual non-adiabatic

[12] The KER spectrum is defined as the distribution over the total kinetic energy of dissociating fragments in the centre-of-mass frame.

[13] As in the previous sections, we consider the primary photoelectron being emitted with high kinetic energy ϵ_0 so that the sudden approximation is applicable. It is thus represented only by the trivial phase factors $e^{-i\epsilon_0 t}$ and as a parameter in the matrix elements of the excitation operator $\hat{\boldsymbol{V}}(\boldsymbol{Q}, t)$.

coupling $\hat{\boldsymbol{\Lambda}}$ is neglected. The matrices $\boldsymbol{U}_X$ are sub-blocks of the non-diagonal potential energy matrix $\boldsymbol{U}$ (1.77a), corresponding to individual manifolds. The off-diagonal block of $\boldsymbol{U}$ representing the coupling between the discrete states and the decay continuum manifolds is again denoted $\boldsymbol{W}(\epsilon)$ and reads

$$W_{\alpha l}(\epsilon, \boldsymbol{Q}) \equiv \langle \boldsymbol{Q}|W_{\alpha l}(\epsilon)|\boldsymbol{Q}'\rangle = \langle \chi_\alpha(\epsilon, \boldsymbol{Q})|\hat{H}_{el}|\phi_l(\boldsymbol{Q})\rangle \delta(\boldsymbol{Q} - \boldsymbol{Q}'). \tag{1.83}$$

Due to the diabatic character of the basis within each manifold, the potential energy matrices $\boldsymbol{U}_d$ and $\boldsymbol{U}_f$ are in general also non-diagonal. The excitation operator $\hat{\boldsymbol{V}}(t)$ is presumed to be of the form given by Eq. (1.24) with the additional dependence on the nuclear geometry.

The solution of Eqs. (1.81) and derivation of the formula for the decay spectrum is fully analogous to the fixed nuclei limit. Indeed, the system of differential equations assumes the exact same form as solved in Sec. 1.4, hence it shares the same formal solution, and the complications only manifest themselves when the working equations in coordinate representation are derived explicitly. We start by invoking the weak-field approximation and neglect the source term in Eq. (1.81a), which allows for its immediate formal solution,

$$|\psi_i(t)\rangle = e^{-i\hat{H}_i t}|\psi_i(0)\rangle. \tag{1.84}$$

Assuming that the system is initially in a stationary vibrational state $|\nu_i\rangle$ corresponding to an eigenenergy E_{ν_i}, the time evolution of the initial wave packet assumes the trivial form

$$|\psi_i(t)\rangle = e^{-iE_{\nu_i} t}|\nu_i\rangle, \tag{1.85}$$

which is to be inserted into the source term in Eq. (1.81b).

The latter is decoupled from the continuous set of differential equations for the final states through the LCP approximation, resulting in [34, 36]

$$i\frac{\partial}{\partial t}|\boldsymbol{\psi}_d(\epsilon_0, t)\rangle = \hat{\boldsymbol{\mathcal{H}}}_d|\boldsymbol{\psi}_d(\epsilon_0, t)\rangle + g(t)e^{-i(E_{\nu_i}-\epsilon_0)t}\boldsymbol{V}(\epsilon_0)|\nu_i\rangle. \tag{1.86}$$

The effective Hamiltonian

$$\hat{\boldsymbol{\mathcal{H}}}_d = \hat{\boldsymbol{H}}_d + \boldsymbol{\Delta}(\boldsymbol{Q}) - \frac{i}{2}\boldsymbol{\Gamma}(\boldsymbol{Q}) \tag{1.87}$$

can be constructed by repeating the procedure discussed in Sec. 1.4 for each geometry. Employing the Fourier transformation (1.36) of the excitation function $g(t)$, the solution for the nuclear wavepackets in the discrete states manifold reads [cf. Eq. (1.37)]

$$|\boldsymbol{\psi}_d(\epsilon_0, t)\rangle = \frac{1}{\sqrt{2\pi}}\int d\omega\, g(\omega)e^{-i(E_{\nu_i}+\omega-\epsilon_0)t}\left(E_{\nu_i} + \omega - \epsilon_0 - \hat{\boldsymbol{\mathcal{H}}}_d\right)^{-1}\boldsymbol{V}(\epsilon_0)|\nu_i\rangle. \tag{1.88}$$

Inserting this expression into the source term of Eq. (1.81c), the final states nuclear wavepackets can be written as

$$\begin{aligned}|\boldsymbol{\psi}_f(\epsilon, \epsilon_0, t)\rangle = -\frac{i}{\sqrt{2\pi}}e^{-i(\hat{\boldsymbol{H}}_f+\epsilon)t}\int d\omega\, g(\omega) \\ \times \int_{-\infty}^{t} d\tau e^{-i(E_{\nu_i}+\omega-\hat{\boldsymbol{H}}_f-\epsilon-\epsilon_0)\tau}\boldsymbol{W}(\epsilon)(E_{\nu_i} + \omega - \epsilon_0 - \hat{\boldsymbol{\mathcal{H}}}_d)^{-1}\boldsymbol{V}(\epsilon_0)|\nu_i\rangle,\end{aligned} \tag{1.89}$$

which is the exact analog of Eqs. (1.38) and (1.57).

Closed-form formula for the coincidence spectrum can be obtained by inserting complete sets of vibronic eigenstates[14] of the Hamiltonian operators in the intermediate and final manifolds into the above formula [36, 64, 65]. Since we are concerned primarily with interatomic decay processes in small weakly bound systems in which the final states are typically dissociative, the Hermitian operator $\hat{\boldsymbol{H}}_f$ has a degenerate continuous real spectrum. In order to unambiguously define the decay channels and KER, we further assume that $\hat{\boldsymbol{H}}_f$ is diagonal in the dissociation limit (large separation of the ionic fragments denoted symbolically as $|\boldsymbol{Q}| \to \infty$) and all the interacting channels have the same threshold energy $U^\infty = [\boldsymbol{U}_f(|\boldsymbol{Q}| \to \infty)]_{\alpha\alpha}$.[15] It is then possible to write the spectrum of $\hat{\boldsymbol{H}}_f$ as

$$\hat{\boldsymbol{H}}_f|\boldsymbol{\zeta}_\beta^{E_{\mathrm{KER}}}\rangle = (E_{\mathrm{KER}} + U^\infty)|\boldsymbol{\zeta}_\beta^{E_{\mathrm{KER}}}\rangle, \qquad \beta = 1, \ldots, N_c \tag{1.90}$$

with E_{KER} being the directly measurable kinetic energy of the dissociating ionic fragments. The indices β denote the degenerate independent solutions. In general it is not possible to associate each $|\zeta_\beta^{E_{\mathrm{KER}}}\rangle$ with any specific channel – the vibronic functions can have nonzero components in all interacting dicationic channels $|\chi_\alpha\rangle$.

The resolution of identity in the space of final vibrational states thus takes on the form

$$\hat{\mathbb{1}} = \sum_\beta \int_0^\infty dE_{\mathrm{KER}}\, |\boldsymbol{\zeta}_\beta^{E_{\mathrm{KER}}}\rangle\langle\boldsymbol{\zeta}_\beta^{E_{\mathrm{KER}}}|. \tag{1.91}$$

Inserting this expansion into the solution (1.89) and taking the limit $t \to \infty$ relevant for the measurable spectra we arrive at (the oscillatory phase is factored out for the limit to exist)

$$|\tilde{\boldsymbol{\psi}}_f(\epsilon, \epsilon_0)\rangle \equiv \lim_{t\to\infty} ie^{i(\hat{\boldsymbol{H}}_f+\epsilon)t}\,|\boldsymbol{\psi}_f(\epsilon, \epsilon_0, t)\rangle = \int dE_{\mathrm{KER}} \sum_\beta |\boldsymbol{\zeta}_\beta^{E_{\mathrm{KER}}}\rangle c_\beta^\infty(E_{\mathrm{KER}}, \epsilon, \epsilon_0) \tag{1.92a}$$

with the expansion coefficients

$$c_\beta^\infty(E_{\mathrm{KER}}, \epsilon, \epsilon_0) = \sqrt{2\pi} g(U^\infty + E_{\mathrm{KER}} + \epsilon + \epsilon_0 - E_{\nu_i}) \langle \boldsymbol{\zeta}_\beta^{E_{\mathrm{KER}}} | \boldsymbol{W}(\epsilon)(U^\infty + E_{\mathrm{KER}} + \epsilon - \hat{\boldsymbol{\mathcal{H}}}_d)^{-1} \boldsymbol{V}(\epsilon_0) | \nu_i \rangle. \tag{1.92b}$$

The expansion coefficients carry the information about the full spectrum,

$$\sigma(E_{\mathrm{KER}}, \epsilon, \epsilon_0) = \sum_\beta |c_\beta^\infty(E_{\mathrm{KER}}, \epsilon, \epsilon_0)|^2, \tag{1.93}$$

[14] The term *vibronic* is used to emphasize the fact that those eigenstates have non-zero components in multiple vibronically coupled electronic states, in contrast to vibrational wave packets which are associated with a single electronic state.

[15] In the case that interacting channels with different threshold energies have to be considered in a single manifold, the formulas for the coincidence and KER spectra become inconveniently cumbersome for our purposes. The problem can be resolved, e.g., by employing projectors onto individual diabatic components of the vibronic eigenstates, see Ref. [66].

measurable through detecting all ionic fragments and both the primary and secondary electrons in coincidence. Introducing further the spectral decomposition of the effective Hamiltonian $\hat{\boldsymbol{\mathcal{H}}}_d$,

$$\hat{\boldsymbol{\mathcal{H}}}_d|\nu_d) = \left(E_{\nu_d} - \frac{i}{2}\Gamma_{\nu_d}\right)|\nu_d), \tag{1.94}$$

the remaining resolvent can be explicitly evaluated to give [36]

$$\sigma(E_{\mathrm{KER}}, \epsilon, \epsilon_0) = 2\pi \sum_{\beta} |g(U^{\infty} + E_{\mathrm{KER}} + \epsilon + \epsilon_0 - E_{\nu_i})|^2 \times \left| \sum_{\nu_d} \frac{\langle \boldsymbol{\zeta}_{\beta}^{E_{\mathrm{KER}}} | \boldsymbol{W}(\epsilon) | \nu_d)(\nu_d | \boldsymbol{V}(\epsilon_0) | \nu_i \rangle}{U^{\infty} + E_{\mathrm{KER}} + \epsilon - E_{\nu_d} + i\Gamma_{\nu_d}/2} \right|^2 . \tag{1.95}$$

In this expression, $|\nu_d)$ and $(\nu_d|$ are the right and left eigenvectors of the non-Hermitian operator $\hat{\boldsymbol{\mathcal{H}}}_d$, see also footnote 7 on page 19. E_{ν_d} and Γ_{ν_d} are, respectively, the real energy and decay width associated with the vibronic eigenstate $|\nu_d)$.

For the sake of simplicity of the following discussion, we will assume that the excitation operator $\boldsymbol{V}(\epsilon_0)$ does not depend on ϵ_0 in the relevant energy range, which is a realistic approximation for fast enough primary photoelectron. Its energy then appears only in the argument of the excitation function $g(\omega)$ and can be integrated out to yield a trivial prefactor σ_0 associated with the total probability of inner-shell photoionization for the given pulse. In other words, the functional dependence of $c_{\beta}^{\infty}(E_{\mathrm{KER}}, \epsilon, \epsilon_0)$ and, thus, of the coincidence spectrum on ϵ and E_{KER} is the same for any fixed value of ϵ_0. The latter affects only the overall intensity and can be ignored. Resulting coincidence spectrum reads

$$\sigma(E_{\mathrm{KER}}, \epsilon) = 2\pi\sigma_0 \sum_{\beta} \left| \sum_{\nu_d} \frac{\langle \boldsymbol{\zeta}_{\beta}^{E_{\mathrm{KER}}} | \boldsymbol{W}(\epsilon) | \nu_d)(\nu_d | \boldsymbol{V} | \nu_i \rangle}{U_{\beta}^{\infty} + E_{\mathrm{KER}} + \epsilon - E_{\nu_d} + i\Gamma_{\nu_d}/2} \right|^2 , \tag{1.96}$$

which is the result commonly found in the literature [17,64]. Although this expression resembles closely the Kramers-Heisenberg formula [67, 68] derived within the second-order perturbation theory, it is not fully equivalent since the latter works with Hermitian operators only [64].

Eqs. (1.95) or (1.96) can be evaluated without propagation of the nuclear wave packets in time but require the vibronic eigenenergies and eigenstates of the Hamiltonian operators for the intermediate and final state manifolds. This is usually the preferable approach if the decay is slow or involves very long-range energy transfer, such as in the case of helium dimer [A9]. Under such conditions, explicit time propagation of the wave packets becomes computationally demanding. With increasing number of degrees of freedom, on the other hand, explicit numerical simulation of the time evolution becomes gradually more efficient in comparison to the solution of Eq. (1.90) over an extended spectral range [34]. It is thus appropriate to express the decay spectra also directly in terms of the time-dependent nuclear wave packets. Besides alternative means of practical calculations, resulting formulas provide a complementary physical understanding of the problem.

The spectrum of the secondary electrons is obtained from the coincidence spectrum through integration over KER,

$$\sigma(\epsilon) = \int dE_{\mathrm{KER}}\, \sigma(E_{\mathrm{KER}}, \epsilon). \tag{1.97}$$

From Eq. (1.92a) it follows immediately that it can be extracted directly from the final state wave packets as [57, 69]

$$\sigma(\epsilon) = \lim_{t\to\infty} \langle \boldsymbol{\psi}_f(\epsilon, t) | \boldsymbol{\psi}_f(\epsilon, t)\rangle. \tag{1.98}$$

The electron spectrum is thus determined by the intricate dynamics of the nuclear wave packets in the manifold of final electronic states. It is driven by the Hamiltonian $\hat{\boldsymbol{H}}_f$ but due to the continuous input of the losses of the metastable states, represented by the source term $\boldsymbol{W}(\epsilon)|\boldsymbol{\psi}_d(t)\rangle$, it also reflects the interference between contributions arriving at different times [63]. Effects of electronic and vibronic interference of overlapping resonances on the electron spectrum are explored in some detail in Ref. [70].

Assuming an energy-independent coupling $\boldsymbol{W}$, i.e., boomerang model-like LCP approximation, an interesting formula for the KER spectrum,

$$\sigma(E_{\mathrm{KER}}) = \int d\epsilon\, \sigma(E_{\mathrm{KER}}, \epsilon), \tag{1.99}$$

can be derived through the expansion of the final state wave packets in terms of the vibronic eigenstates (1.91)

$$|\boldsymbol{\psi}_f(\epsilon, t)\rangle = \sum_\beta \int_0^\infty dE_{\mathrm{KER}}\, c(E_{\mathrm{KER}}, \epsilon, t) |\boldsymbol{\zeta}_\beta^{E_{\mathrm{KER}}}\rangle. \tag{1.100}$$

Inserting the expansion into the differential equation (1.81c) and integrating over ϵ yields[16]

$$\sigma(E_{\mathrm{KER}}) = 2\pi \sum_\beta \int_{-\infty}^\infty d\tau\, |\langle \boldsymbol{\zeta}_\beta^{E_{\mathrm{KER}}} | \boldsymbol{W} | \boldsymbol{\psi}_d(\tau)\rangle|^2. \tag{1.101}$$

This formula shows that the KER spectrum is given by accumulated generalized Franck-Condon factors connecting $|\boldsymbol{\psi}_d(t)\rangle$ and the dissociative final state vibronic eigenfunctions [63]. Note that all contributions are added in absolute value squared and, in contrast to the electron spectrum, no interference occurs.

The results (1.98) and (1.101) corroborate that the two spectra carry complementary information, as stated in the discussion below Fig. 1.4. While valuable for the understanding of the formation of the KER spectrum, Eq. (1.101) still requires the knowledge of the vibronic eigenstates $|\boldsymbol{\zeta}_\beta^{E_{\mathrm{KER}}}\rangle$. In actual numerical propagation of the nuclear wave packets, it can be circumvented and the coincidence and thus also the KER spectrum computed directly from the time-dependent wave functions through analysis of the outgoing flux in the dissociative channels [71].

[16] For energy-dependent coupling $\boldsymbol{W}(\epsilon)$, integration over ϵ cannot be performed in closed form and the formula for $\sigma(E_{\mathrm{KER}})$ would contain products of the $\langle \boldsymbol{\zeta}_\beta^{E_{\mathrm{KER}}} | \boldsymbol{W}(\epsilon) | \boldsymbol{\psi}_d(\tau)\rangle$ matrix elements evaluated at different times, another manifestation of the memory effects in the evolution of the metastable states.

Chapter 2

Ab initio methods for decay widths

It follows from Chap. 1 that quantitative description of the electronic decay in polyatomic systems relies on accurate potential energy surfaces and decay widths associated with the involved electronic states. In particular, the knowledge of the time scale of the decay process is the key not only for reliable prediction of the observable quantities but already for the qualitative assessment of the significance of various dynamical aspects of the problem.

Thus, our goal in the present chapter is to determine the complex effective Hamiltonian, Eqs. (1.59) and (1.60), governing the evolution of the metastable state in the fixed-nuclei limit. We fully adopt the two-step description of the excitation and the subsequent decay processes and restrict ourselves to the $N-1$-electron metastable state, disregarding the primary electron as well as the excitation mechanism. Most of the discussion, however, is completely general, the notion of the metastable state relating to the ionized systems is kept only for consistency and argument's sake.

Methods available for *ab initio* calculation of the decay widths can be generally divided into two main categories. The first class comprise methods based on true continuum wave functions, such as the R-matrix method [72] [A3] or the single-centre expansion [73]. The second category utilizes square-integrable ($\mathcal{L}^2$) basis sets to approximate both the bound and continuum multi-electron wave functions. It results in discretized decay continua, but usually also in lower computational demands. In addition, $\mathcal{L}^2$-based approaches can build on the highly developed foundations of computational quantum chemistry for bound states, facilitating the implementation of highly efficient codes. The inevitable shortcomings are connected with the incorrect boundary conditions satisfied by the approximate wave functions, e.g., the impossibility to properly discriminate between individual decay channels or to study the angular distribution of the decay products. In this chapter, we focus primarily on the Fano-ADC method, which proved to be the method of choice for interatomic decay processes due to its computational efficiency and the ability to provide converged results over many orders of magnitude. Furthermore, despite the incorrect boundary condition, it can still be used to estimate the partial decay widths. Other methods are also briefly discussed but we mostly refer the reader to the existing literature.

2.1 Fano-ADC method

Building on the work of Howat *et al.* [51], the Fano-ADC method was initially devised and first applied to study ICD widths by Averbukh and Cederbaum in 2005 [74]. Starting from the Fano theory of resonances [25, 75], it is based on the explicit construction of the discrete state representing the resonance and thus fits well into the framework introduced in Chap. 1. The many-electron wave functions are constructed in terms of an $\mathcal{L}^2$ basis using size-consistent and fast-convergent algebraic diagrammatic construction (ADC) methodology [76, 77] in the intermediate states representation (ISR) [78, 79]. Correct normalization and interpolation of the discretized continuum is achieved via the Stieltjes imaging technique [80, 81].

Over the last decade, the method was further developed and generalized for a wider range of problems, namely ICD in doubly ionized [A2] as well as neutral excited clusters [82, 83], and has been recently utilized to study also the Penning ionization [84]. Generic implementation applicable to systems with arbitrary symmetry was first described by Kolorenč and Sisourat in Ref. [85] for ICD in helium trimer. Among the most notable applications of the Fano-ADC method rank the study of ICD in helium dimer [A9], electron transfer-mediated decay in $NeKr_2$ [A12], resonant Auger-ICD cascades [A13], or collective decay in fluoromethane [A7].

Through the extension of the ADC methodology to the four-component framework [86, 87], it is possible to study also the effects of relativistic phenomena, such as spin-orbit coupling, on the electronic decay process [88]. Full potential of the ADC methodology was recently exploited through the development of the ADC(2,2) approximation scheme [A1], which enabled for the first time to represent electron correlation – the primary driver of the processes of interest – in both the initial and final states of the decay in a balanced and consistent way. In the latter reference, the method is described in great detail, so only a brief overview is given in the following.

2.1.1 Fano theory of resonances

Fano theory of resonances, on which the Fano-ADC methodology relies, was described in Sec. 1.1 for the case of single metastable state interacting with a single decay continuum, and in Sec. 1.4 for an arbitrary number of metastable states as well as decay channels. A concise overview of the aspects directly relevant to the Fano-ADC methodology can be found in Ref. [A1].

The form of the electronic Hamiltonian (1.52) is associated with the basis of the $(N-1)$-electron Hilbert space, consisting of N_d discrete states $|\phi_{d_l}\rangle$ $(l = 1 \dots N_d)$ and N_c decay continua described by continuum wave functions $|\chi_\alpha(\epsilon)\rangle$ $(\alpha = 1 \dots N_c)$ with ϵ denoting the energy of the outgoing electron. It is convenient to introduce the partitioning of the Hilbert space into the subspace $\mathcal{Q}$ containing the discrete states and the (background) continuum subspace $\mathcal{P}$,

through definition of the respective projection operators[1] [75]

$$\hat{Q} = \sum_{l=1}^{N_d} |\phi_{d_l}\rangle\langle\phi_{d_l}| \quad \text{and} \quad \hat{P} = \sum_{\alpha=1}^{N_c} \int d\epsilon \, |\chi_\alpha(\epsilon)\rangle\langle\chi_\alpha(\epsilon)|. \tag{2.1}$$

If possible, the two subspaces are defined as complementary with the corresponding projectors being orthogonal, but a handy feature of the Fano theory is that it is not strictly required. Construction of the projectors within the framework of an *ab initio* methodology chosen to represent the many-electron wave functions and, in turn, the electronic Hamiltonian comprises the key step in the development of a practical computational method. The fundamental requirement is that the discrete states have strictly bound character within the $\mathcal{Q}$ subspace itself and can only decay via the interaction with the continuum states from the $\mathcal{P}$ subspace. $\mathcal{Q}$ thus contains purely $\mathcal{L}^2$ wave functions while the $\mathcal{P}$ subspace is composed of continuum (or continuum-like) functions representing states with at least one outgoing electron.

Once the projectors (2.1) are defined, the discrete states representing individual resonances are usually identified with eigenstates of the Hamiltonian projected onto the $\mathcal{Q}$ subspace,

$$\hat{Q}\hat{H}\hat{Q}|\phi_{d_l}\rangle = E_{d_l}|\phi_{d_l}\rangle. \tag{2.2}$$

Likewise, the background continuum is assumed to diagonalize the Hamiltonian in the $\mathcal{P}$ subspace,

$$\langle\chi_{\alpha'}(\epsilon')|\hat{P}\hat{H}\hat{P} - E|\chi_\alpha(\epsilon)\rangle = (E_\alpha + \epsilon - E)\delta_{\alpha'\alpha}\delta(E_{\alpha'} + \epsilon' - E_\alpha - \epsilon). \tag{2.3}$$

If the Hamiltonian depends parametrically on the nuclear coordinates in a polyatomic system, this corresponds to an electronic basis which is adiabatic within each subspace [cf. Eq. (1.75)]. The level shift matrix is then evaluated using Eq. (1.59). Namely, the formula for the decay width matrix $\mathbf{\Gamma}(E)$ has the form of the sum over decay channels and reads

$$[\mathbf{\Gamma}(E)]_{ll'} = 2\pi \sum_{\alpha=1}^{N_c} \langle\phi_l|\hat{H} - E|\chi_\alpha(E - E_\alpha)\rangle\langle\chi_\alpha(E - E_\alpha)|\hat{H} - E|\phi_{l'}\rangle. \tag{2.4}$$

The energy E subtracted from the Hamiltonian in the above matrix element compensates for the possible non-orthogonality of the $\mathcal{Q}$ and $\mathcal{P}$ subspaces [51, 74].

Construction of the LCP approximation from the known level shift matrix $\boldsymbol{\mathcal{F}}(E)$ and the energies of the discrete states given by Eq. (2.2) was discussed in detail in Sec. 1.4. It provides the sought-after complex PESs required for the efficient description of the nuclear dynamics aspect of the decay process. If relevant, a fully diabatic basis can be obtained through subsequent transformations within each subspace. We will see below, however, that in the case of a

[1] The projection operator $\hat{Q}$ should not be confused with the generalized nuclear coordinates $\boldsymbol{Q}$ as used in Sec. 1.5. We find it preferable to adhere in both contexts to the established notations, notwithstanding the occasional conflict.

discretized continuum stemming from the use of an $\mathcal{L}^2$ basis, the Stieltjes imaging technique allows to recover only the diagonal elements of the decay width matrix,

$$\Gamma_l(E) = \sum_{\alpha=1}^{N_c} \Gamma_{l,\alpha}(E) = 2\pi \sum_{\alpha=1}^{N_c} |\langle \phi_l | \hat{H} - E | \chi_\alpha(E - E_\alpha) \rangle|^2, \tag{2.5}$$

which are necessarily real and non-negative. The *via the continuum* coupling between the interacting resonances thus can be taken into account only approximately or neglected.

2.1.2 Algebraic diagrammatic construction

To evaluate the formula (2.4), approximations for the initial and final states multi-electron wave functions, $|\phi_l\rangle$ and $|\chi_\alpha(\epsilon)\rangle$, have to be provided. In the case of ICD of an inner-valence vacancy, they are both associated with $(N-1)$-electron states and can be thus represented using an ADC scheme for single ionization. Originally, the so-called direct ADC procedure was developed within the Green's function (GF) formalism [77]. It provides a framework to develop a hierarchy ADC(n) of approximations for the one-electron propagator which are complete through the order n of the perturbation theory (PT). In addition, ADC(n) schemes include infinite partial summations needed to recover the correct simple poles analytical structure of the propagator, which is lost in the traditional diagrammatic approach. The method can be readily applied to construct multi-electron GF [89, 90] or the polarization propagator [76, 91]. A detailed and pedagogical account on ADC and related many-body methods is available in the excellent recent book by J. Schirmer [92].

For the Fano-ADC method, it is the alternative ISR-ADC formulation [78, 79] that is relevant. The key point is that, in contrast to the direct ADC procedure, ISR-ADC is a wave function method and thus provides explicit representations of the $(N-1)$-electron states needed to evaluate the coupling matrix elements involved in Eq. (2.4). Most conveniently, the method can be explained in comparison to the well-known configuration interaction (CI) expansion [93], which represents the most straightforward approach to describe electronic correlation in quantum chemistry.

Consider the Hartree-Fock (HF) ground state $|\Phi_0\rangle$ of the N-electron system. Using the so-called physical excitation operators,

$$\left\{\hat{C}_J\right\} = \left\{c_k; c_a^\dagger c_k c_l, k<l; c_a^\dagger c_b^\dagger c_j c_k c_l, j<k<l; \ldots\right\}, \tag{2.6}$$

a complete orthonormal set of $(N-1)$-electron basis functions (also called HF configurations) can be derived as

$$|\Phi_J\rangle = \hat{C}_J |\Phi_0\rangle. \tag{2.7}$$

The indices j, k, l, ... and a, b, ... correspond to the occupied and virtual HF orbitals, respectively. The HF configurations are naturally classified as *one-hole* ($1h$), *two-hole-one-particle*

$(2h1p)$ and so on, according to the degree of excitation. The common notation is that J denotes individual configuration while $[J] = \mu$ stands for the whole $\mu h - (\mu - 1)p$ excitation class.

The basis set (2.7) is used in the CI method for expansion of the correlated $(N-1)$-electron wave functions $|\Psi_{\boldsymbol{q}}^{(N-1)}\rangle$, where $\boldsymbol{q}$ denotes the complete set of quantum numbers specifying the ionized state. The principal drawback of such a direct approach is slow convergence and, once truncated after some specific excitation class $[J]$, lack of size consistency. The slow convergence is rooted in the fact that the HF configurations are uncorrelated and, therefore, every ionized state is constructed "from scratch". In search of an improvement, the ISR-ADC employs an alternative basis set of the so-called correlated excited states (CESs),[2]

$$|\Psi_J^0\rangle = \hat{C}_J|\Psi_0\rangle, \tag{2.8}$$

where $|\Psi_0\rangle$ is the exact N-electron ground state. The intuitive idea underlying the use of CESs is that the removal of an electron affects the correlation with respect to the initial N-electron ground state but does not alter it completely. Therefore, the information on the correlation in the N-electron system conveyed by the CESs should result in faster convergence of the subsequent expansion of the $(N-1)$-electron wave functions [92].

In contrast to the HF configurations (2.7), the CESs (2.8) are not orthonormal. It is the specific *excitation class orthogonalization* (ECO) procedure that leads to an orthonormal basis of intermediate states (ISs) $|\tilde{\Psi}_J\rangle$, providing the sought-after size-consistent and fast-convergent expansion of $|\Psi_{\boldsymbol{q}}^{(N-1)}\rangle$. ECO is an iterative process consisting of Gram-Schmidt orthogonalization between different excitation classes and symmetric orthogonalization of the resulting *precursor states* within each excitation class. For more details see Refs. [92] [A1].

Using the complete manifold of excitation operators (2.6), the basis of ISs provides an exact representation of the secular matrix (shifted Hamiltonian with E_0 being the exact neutral ground state energy),

$$M_{IJ} = \langle\tilde{\Psi}_I|\hat{H} - E_0|\tilde{\Psi}_J\rangle \tag{2.9}$$

as well as of the $(N-1)$-electron wave functions,

$$|\Psi_{\boldsymbol{q}}^{(N-1)}\rangle = \sum_J Y_{\boldsymbol{q},J}|\tilde{\Psi}_J\rangle. \tag{2.10}$$

A practical computation scheme is obtained by using truncated PT expansion for the neutral ground state through the order n,

$$|\Psi_0\rangle = |\Phi_0\rangle + |\Psi_0^{(1)}\rangle + \cdots + |\Psi_0^{(n)}\rangle + O(n+1), \tag{2.11}$$

which in turn leads naturally to the PT expansions of the ISs, the ground state energy E_0, and finally the secular matrix elements M_{IJ}. To arrive at a consistent scheme, the wave function expansion (2.10) has to be truncated after some specific excitation class, restricting the active

[2] ISR-ADC is not the only *ab initio* method that can be formulated in terms of CESs or other intermediate states. Other representatives are equation-of-motion or biorthogonal coupled-cluster methods [92].

configuration space. Ionization energies and the corresponding $(N-1)$-electron eigenstates are then obtained by diagonalization of the resulting finite matrix $\boldsymbol{M}$.

One of the defining properties of the ADC method are the *canonical order relations* (COR), according to which the PT expansion of the off-diagonal ($[I] \neq [J]$) matrix elements of the secular matrix follow the general rule

$$M_{IJ} \sim O(|[I] - [J]|). \tag{2.12}$$

COR dictates at which order and excitation class the expansions (2.11) and (2.10) have to be truncated, respectively, in order to obtain ionization energies consistent through the required PT order. If $|\Psi_{\boldsymbol{q}}^{(N-1)}\rangle$ is an eigenstate belonging to the excitation class $[I]$ (i.e., it's expansion is dominated by class $[I]$ ISs), truncation of the configuration space after the excitation class $[J] > [I]$ introduces an error of order $2(J+1-I)$. Specifically, for main $1h$ states ($I=1$) this means an error of order $2J$, which can be compared to an error of the order $(J+1)$ for the slower converging CI expansion.

The ISR-ADC scheme most commonly employed in the Fano-ADC method is the extended second-order scheme [ADC(2)x]. The configuration space is spanned by the $1h$ and $2h1p$ ISs and the $1h/1h$ block of the secular matrix contains corrections up to the second-order of PT, while the $1h/2h1p$ and $2h1p/2h1p$ blocks only up to the first order. As a result, the energies of the $1h$-like states are determined through the second-order while those of the $2h1p$-like states through the first order of PT only. Since in a typical application, the initial state of the decay belongs to the $1h$ class while the final state into to $2h1p$ class (the "particle" orbital representing the electron in the continuum), such a correlation imbalance can compromise the accuracy of the calculated decay widths.

To remedy this shortcoming, we have recently introduced the ADC(2,2) approximation [A1] which, through the inclusion of the $3h2p$ excitation class and appropriate order structure of the secular matrix $\boldsymbol{M}$ (see Tab. I in Ref. [A1]), allows for a balanced description of both $1h$ and $2h1p$-like states through second order of PT. In addition to the improved accuracy, the ADC(2,2) scheme also provides access to second-order decay processes resulting in two secondary electrons, such as double Auger decay [94]. The price to be paid is significant growth of computational demands connected with the large $3h2p$ excitation class. Compared to the ADC(2)x scheme, the computational cost increases from $n_{occ}^3 n_{virt}^2$ to $n_{occ}^3 n_{virt}^4$, where n_{occ} and n_{virt} are the numbers of occupied and virtual orbitals, respectively. For larger polyatomic systems, ADC(2)x thus remains the method of choice.

2.1.3 Fano theory in the framework of ISR-ADC

As pointed out in Sec. 2.1.1, the key step in the implementation of the Fano theory within the framework of an *ab initio* methodology for many-electron wave functions is the definition of the $\mathcal{Q}$ and $\mathcal{P}$ subspaces, or equivalently, the construction of the corresponding projectors (2.1).

In a rigorous theory, the fundamental difference between the two subspaces is that $\mathcal{Q}$ contains strictly $\mathcal{L}^2$ wave functions, ensuring that the corresponding states cannot decay within the $\mathcal{Q}$ subspace itself. This also guarantees that the $\mathcal{P}$ subspace is asymptotically complete,

$$\lim_{r\to\infty} \langle \boldsymbol{r}|\hat{P}|\Psi_E\rangle = \lim_{r\to\infty} \langle \boldsymbol{r}|\Psi_E\rangle, \tag{2.13}$$

where $|\Psi_E\rangle$ with $E > 0$ is a continuum state and r is the radial coordinate of the outgoing particle. In a method employing $\mathcal{L}^2$ one-particle basis set, however, this distinction is lost as $\mathcal{L}^2$ wave functions approximate even the continuum states. Therefore, other criteria leading to an appropriate classification of the ISs have to be devised.

The requirement that the discrete components are bound within the $\mathcal{Q}$ itself means that any representation of $|\phi_l\rangle$ must not contain any contribution corresponding to the possible final states of the decay. The first observation is that, within an ISR-ADC scheme, such final states are represented by $2h1p$ or higher excitation classes as the electron has to be described by a virtual orbital. However, these classes are also vital to account for the correlation in the discrete states, or the discrete state itself can be of $2h1p$ character if we are interested in metastable shake-up satellite states. Thus, corresponding ISs have to be divided appropriately between both the $\mathcal{Q}$ and $\mathcal{P}$ subspaces.

The applicability of possible classification schemes depends on the character of the decay process. For the argument's sake, we will focus on the $2h1p$ excitation class, but generalization to higher classes is straightforward, see Ref. [A1]. In many cases, the $2h1p$ ISs can be directly associated with open or closed decay channels based on either the core/valence character or the spatial localization of the HF molecular orbitals (MOs) defining the $2h$ configuration. In the case of Auger decay of a core vacancy, energetically accessible final states are typically characterized by all $2h$ configurations that do not contain the initial or deeper-lying vacancies. Similar situation is encountered when studying an interatomic decay process in a hetero-nuclear cluster such as

$$(A^+)^*B \to \begin{cases} A^+ + B^+ + e^- & \text{ICD} \\ A + B^{2+} + e^- & \text{ETMD} \end{cases},$$

in which MOs are spatially localized on specific atoms. Here, the final states are distinguished by at least one vacancy on the initially neutral cluster constituent B, which in turn defines ISs belonging to the $\mathcal{P}$ subspace.

In other cases, however, there is no straightforward one-to-one correspondence between the $2h1p$ ISs and the open or closed channels of the decay process. Complications arise, e.g., when MOs are delocalized due to some symmetry of the system. In such a case, some localization procedure, based on an appropriate transformation of the basis of ISs, needs to be performed prior to the $\mathcal{Q}/\mathcal{P}$ classification. An example is a homonuclear dimer such as Ne_2, in which all MOs are delocalized over both atoms due to the inversion symmetry and form gerade-ungerade pairs. Here, specific symmetrization procedure can be devised [95] to restore the localized

character of the vacancies, resulting in the adapted $2h1p$ ISs that can be readily classified among the two subspaces.

The symmetrization procedure can be generalized to polyatomic systems with arbitrary symmetry and for higher excitation classes as shown in Refs. [85] and [A1]. First, the $2h1p$ ISs are divided into subsets characterized by the virtual orbital p. When the corresponding small blocks of the ADC secular matrix $\boldsymbol{M}$ are separately diagonalized, the resulting eigenvalues closely mimic the structure of the double ionization thresholds associated with the decay channels. The extra electron attached in the virtual orbital p leads essentially to a uniform shift approximately defined by the corresponding HF energy ε_p, as illustrated in Fig. 2.1 on the example of ICD in the neon dimer. In other words, the partial diagonalization effects the transformation from ISs derived from uncorrelated $2h$ HF configurations to adapted ISs defined by correlated $2h$ states. Each adapted IS can thus be associated with a specific decay channel and the corresponding eigenvectors thus naturally belong to $\mathcal{P}$ or $\mathcal{Q}$, depending on whether the channel is open or closed.

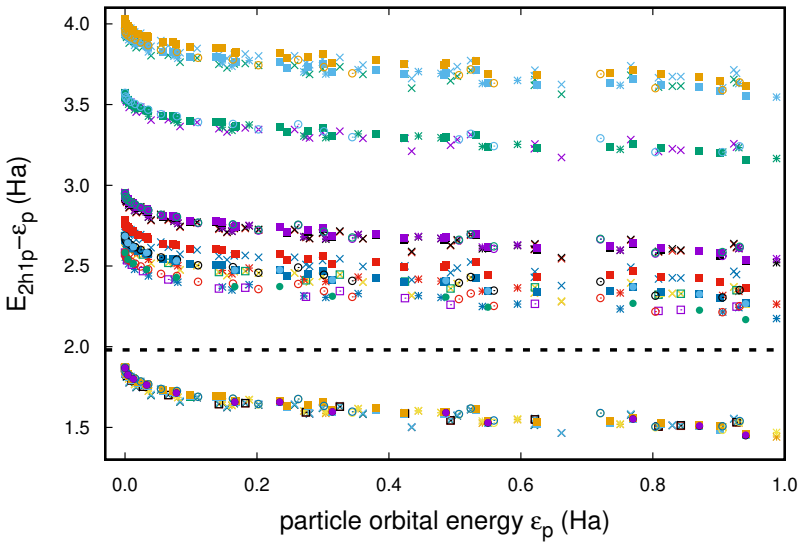

Figure 2.1: $\mathcal{Q}-\mathcal{P}$ partitioning in neon dimer (equilibrium interatomic distance). Points show shifted eigenvalues $E_{2h1p}-\varepsilon_p$ of the sub-blocks of the ADC secular matrix $\boldsymbol{M}$ defined the specific virtual MO p with the HF energy ε_p. Different point types and colours distinguish the symmetry and numbering of the eigenvalues. The dashed black line indicates the HF energy $-\varepsilon_{2\sigma_u}$ of the initial inner-valence vacancy defined by the $2\sigma_u$ MO. It unambiguously divides the shifted eigenvalues into the lower-lying group of two-site ISs corresponding to open ICD channels of the type $\mathrm{Ne}^+(2p^{-1})-\mathrm{Ne}^+(2p^{-1})$, and the higher-lying groups of ISs contributing into the expansion of the metastable state.

The apparent merit of this procedure is the universality. It can be readily applied also to the $3h2p$ excitation class present in the ADC(2,2) scheme, as well as to the $3h1p$ class when describing the decay of initially doubly ionized systems using the ADC(2)x scheme for the two-electron propagator [A2]. Virtually the only input required for the calculation of the decay width is the number of open decay channels for a given metastable state. Still, some care is needed if

the energy gap dividing the open and closed channels is very narrow. The extra electron in the virtual orbital can then cause significant mixing of the open and closed channels in the adapted ISs, resulting in a breakdown of the strictly bound character of the $\mathcal{Q}$ subspace [A1].

Once the projectors onto the $\mathcal{Q}$ and $\mathcal{P}$ subspaces are defined within the full configuration space, the discrete states $|\phi_l\rangle$ representing the metastable states of interest are selected among the eigenstates of the projected Hamiltonian matrix **QMQ**. The selection criterion is typically the dominant $1h$ configuration. The decay continuum $|\chi_\alpha(\epsilon)\rangle$ is approximated by the eigenstates $|\chi_i\rangle$ corresponding to the discrete eigenvalues ϵ_i of the **PMP** matrix. The discrete character of the spectrum, however, prevents the straightforward use of the eigenfunctions $|\chi_i\rangle$ in the decay width formula (2.4). First, these wave functions do not satisfy the appropriate boundary conditions and are normalized to unity rather than energy,

$$\langle\chi_i|\chi_j\rangle = \delta_{ij}. \tag{2.14}$$

Second, the spectrum has to be interpolated to obtain the energy-dependent width matrix.

The solution of these problems is provided by the so-called Stieltjes imaging technique [80, 81, 96], at least for the diagonal elements (2.5) of the decay width matrix. The approach relies on the fact that the wave functions $|\chi_i\rangle$ provide good approximations of the spectral moments of the decay width function,

$$S_l^k \equiv \int dE\, E^k \Gamma_l(E) = 2\pi \sum_{\alpha=1}^{N_c} \int dE\, E^k |\langle\phi_l|\hat{H} - E|\chi_\alpha(E - E_\alpha)\rangle|^2 \approx 2\pi \sum_i (\epsilon_i)^k |\langle\phi_l|\hat{H} - E_{d_l}|\chi_i\rangle|^2. \tag{2.15}$$

It rests on the assumption that, within the region defined by the spatial extent of the discrete states, the solutions $|\chi_i\rangle$ can replace the exact resolution of identity within the $\mathcal{P}$ subspace,

$$\sum_{\alpha=1}^{N_c} \int d\epsilon\, |\chi_\alpha(\epsilon)\rangle\langle\chi_\alpha(\epsilon)| \approx \sum_i |\chi_i\rangle\langle\chi_i|. \tag{2.16}$$

Using the lowest $2n_S$ spectral moments (2.15), an approximation of order n_S of the decay width function $\Gamma_l(E)$ can be recovered using the moment theory. It is obtained in terms of the n_S-point integration quadrature,

$$\int dE\, \Gamma(E) f(E) \approx \sum_{i=1}^{n_S} w_i^{n_S} f(E_i^{n_S}), \tag{2.17}$$

where the decay width $\Gamma(E)$ plays the role of *a priori* unknown weight function. At each order n_S, piece-wise approximation of the correctly normalized decay width $\Gamma(E)$ is obtained from the cumulative function

$$F(E) = \int_{E_{\min}}^{E} dE'\, \Gamma(E') \approx \sum_{i=1}^{q} w_i^{n_S}, \quad E_q^{n_S} < E < E_{q+1}^{n_S} \tag{2.18}$$

through the Stieltjes derivative as

$$\Gamma^{n_S}(E) = \frac{1}{2}\frac{w_{q+1}^{n_S} + w_q^{n_S}}{E_{q+1}^{n_S} - E_q^{n_S}}. \tag{2.19}$$

The procedure thus effectively yields $\Gamma(E)$ at $n_S - 1$ discrete points. Convergence can be controlled by performing a series of approximations of increasing order n_S. Furthermore, in the region of convergence, results from several consecutive orders can be combined to increase the sampling of the energy dependence. Illustration of the procedure is shown in Fig. 2.2, which shows the total ICD width in the neon dimer.

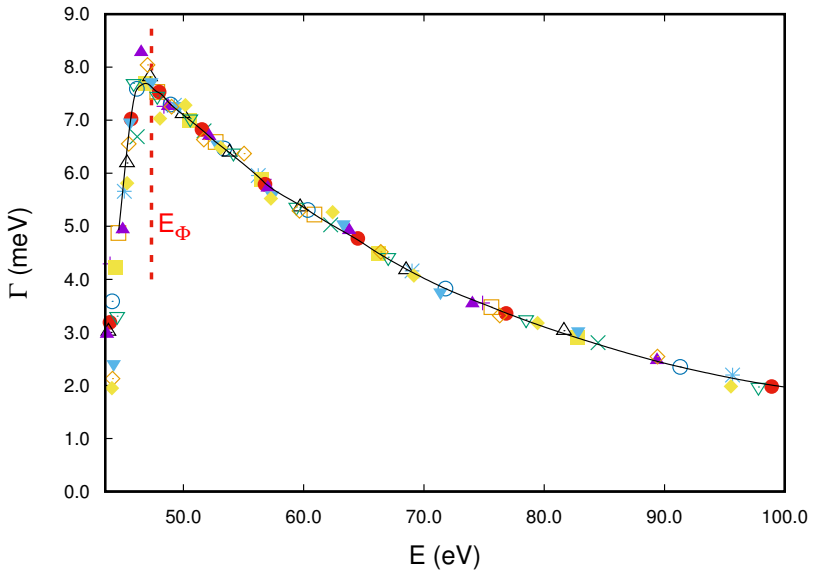

Figure 2.2: Output of the Stieltjes imaging procedure for the total ICD width for the $Ne^+(2s^{-1})Ne\ ^2\Sigma_u^+$ metastable state of neon dimer at the equilibrium geometry. Points of different colours show approximations for $\Gamma(E)$ obtained at individual orders $n_S = 8 - 20$. The black curve is the interpolation obtained using three consecutive orders $n_S = 11 - 13$. Red dashed line indicates the discrete state energy.

Several serious limitations stem from the use of the Stieltjes imaging technique. Most obviously, the weight function in a Gaussian quadrature has to be positive, which is only satisfied for the diagonal elements (2.5) of the decay width matrix. The off-diagonal elements are thus not accessible. Furthermore, the piece-wise approximation usually does not allow for a reliable evaluation of the level shift function $\Delta(E)$ (1.59). Therefore, the resonance energies and widths are commonly approximated as $E_{res_l} \approx E_{d_l}$ and $\Gamma_l \approx \Gamma_l(E_{d_l})$, respectively. For majority of ICD-active states, however, such an approximation is justified as the widths are small enough for the level shift being comparable to the inherent inaccuracy of the *ab initio* methodology.

It follows from Eq. (2.16) that it is not possible to formulate a rigorous procedure for the calculation of the partial decay widths $\Gamma_{l,\alpha}$. This problem is common to the $\mathcal{L}^2$ methods as the decay channels are defined only asymptotically with respect to the position of the outgoing particle. However, the partial decay widths can still be estimated if approximate channel

projectors P_α can be defined in terms of the $\mathcal{L}^2$ ISs. For each channel, the Stieltjes imaging procedure is then repeated with the projected continuum-like functions $P_\alpha|\chi_i\rangle$, as detailed in Refs. [74, 97, 98]. The possibility to obtain (even if only approximate) partial decay widths constitute substantial benefit of the method compared to the alternatives like methods based on complex absorbing potentials or complex scaling. Furthermore, since the $|\chi_i\rangle$ functions only need to accurately mimic the continuum functions over the spatial extent of the discrete state wave function [cf. Eq. (2.15)], Fano-ADC is typically less demanding concerning the quality of the one-particle basis set.

2.2 The alternatives

Despite its many favourable properties, Fano-ADC method is not the only viable option to compute interatomic decay widths. Possibly the most straightforward $\mathcal{L}^2$ method relies on the introduction of a complex absorbing potential (CAP) [99, 100] into the many-electron Hamiltonian to damp the wave functions in the asymptotic region and squeeze the continuum and even the divergent Siegert states into the $\mathcal{L}^2$ functions space. As a representative of the methods employing true continuum wave functions, we will briefly discuss the R-matrix theory [72], which counts as one of the most versatile tools to study resonances, e.g., in electron-molecule collisions. The method is becoming increasingly popular due to the recent code development [101] and the generalization to the time domain [102].

Complex absorbing potential

Methods based on complex absorbing potential target directly the Siegert states associated with the complex eigenenergies, $Z_{res} = E_{res} - i\Gamma/2$, of the electronic Hamiltonian. Similarly to the real-energy solutions near the resonance, the Siegert states are localized in the interaction region but diverge exponentially outside. Mathematically, they can be characterized as solutions satisfying purely outgoing-wave asymptotic form [20]. As such, they are not easily amenable to numerical representation, and less so using an $\mathcal{L}^2$ basis set. However, the introduction of a suitable artificial potential with a negative imaginary part into the Hamiltonian,

$$\hat{H}(\eta) = \hat{H} - i\eta\hat{W}, \tag{2.20}$$

induces an exponential damping and transforms the Siegert states into $\mathcal{L}^2$ wave functions, as demonstrated in Fig. 2.3. Such a solution can then be found by means of the quantum chemistry methodology developed for bound states, with the decay width given by the imaginary part of the corresponding complex eigenenergy.

The operator $\hat{W}$ in Eq. (2.20) is a real non-negative potential, which has to be localized outside the region of the nonzero electronic density of the bound states of the system to avoid unwanted perturbations of the physics. Furthermore, the shape of CAP has to be chosen

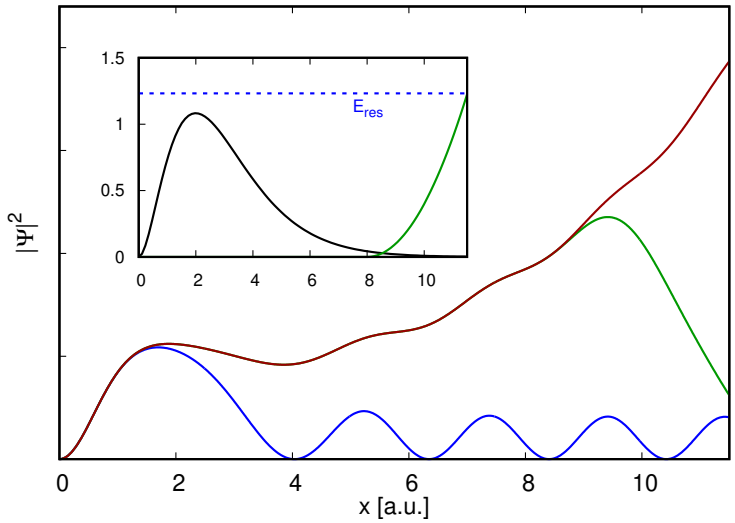

Figure 2.3: Example of the action of CAP on the solution of one-dimensional TISE. **Inset:** interaction potential $2x^2e^{-x}$ (black) and the imaginary part of the CAP $W(x) = -0.1i(x - 8.0)^2$ (green, with the opposite sign). Dashed blue line indicates the real part of the resonance energy $z_{\text{res}} = 1.2318 - 0.16496i$ a.u. **Main plot:** Solution of the TISE for the real energy $E_{\text{res}} = 1.2318$ a.u. (blue) and for the complex energy z_{res} (Siegert state, red), both without CAP. Green line shows the solution at z_{res} after the addition of CAP $W(x)$.

carefully to damp the wave functions efficiently while avoiding artificial reflections [100]. These two requirements are to a large extent conflicting, as the former requires large enough CAP strength η while a weak CAP best meets the latter. The optimal balance and thus the best approximation to the Siegert energy is found by searching for a stabilization point of the eigenenergy trajectory $E(\eta)$, obtained by the diagonalization of the complex Hamiltonian (2.20) for different values of the strength parameter η [99].

The modified non-Hermitian Hamiltonian can be represented employing various *ab initio* methods for excited states [103], including the ISR-ADC discussed above. The resulting CAP-ADC method was applied to compute decay widths in the neon dimer [104] or excited atom-molecule complexes [105]. CAP is also commonly used in connection with the CI expansion [106–108]. More recently, CAP was successfully combined with the equation-of-motion coupled-cluster technique [109–111].

The damping effect needed to confine the Siegert states can be accomplished also by complex scaling of the electronic coordinates, $r \to re^{i\theta}$ [52]. It is done either globally or only in the outer region (exterior complex scaling) [112,113]. After the transformation, the continuum spectrum is uniformly rotated into the lower complex energy plane while the eigenvalues corresponding to the bound and resonance states are equal to those of the unaltered Hamiltonian [114]. In that respect, complex scaling represents a more rigorous approach but brings about considerable technical difficulties associated with the need for the analytical continuation of the Hamiltonian operator. The appeal of CAP, on the other hand, rests in its simplicity and relative ease of implementation. Compared to Fano-ADC, it requires less prior physical insight, which is needed

in the latter for the appropriate $\mathcal{Q}/\mathcal{P}$ partitioning. The major disadvantage of CAP-based methods lies in their enormous computational costs connected with the multiple diagonalization of complex symmetric Hamiltonian matrices [19], and the demand for a high-quality diffuse basis set for an accurate representation of CAP in the outer region. In addition, the approach provides only the total decay widths.

R-matrix method

The R-matrix method [115,116] represents a completely different theoretical framework to seek the solutions of TISE in the continuum energy domain. It has been successfully employed to study resonances in electron-atom and electron-molecule collisions, and its application to compute electronic decay widths is rather straightforward. In the framework of the scattering theory, the autoionizing states discussed in this work can be associated with Feshbach-type resonances [23] in collisions of an electron with the ionized target system. In contrast to the Fano-ADC or CAP techniques, the R-matrix framework is better suited for the computation of partial decay widths as the true continuum wave functions with proper boundary conditions are employed.

In the R-matrix method, the configuration space is separated into the inner and the outer region by a sphere of radius a centred at the centre-of-mass of the system. The inner region contains an explicit multi-electron description of the N-electron target plus the scattered electron, and all the $N+1$ electrons are treated as correlated. Here, the number N relates to the number of electrons in the final state of the target *after* the decay. In the outer region, characterized by the vanishing electron density of the N-electron system, only the free electron is considered, and its interaction with the target is described in terms of a multipole expansion of the interaction potential. The solutions in the two regions are linked by the R-matrix.[3]

The first step of the calculation is diagonalization of the modified Hamiltonian,

$$\hat{H}_a = \hat{H}_{el} + \hat{L}, \tag{2.21}$$

within the Hilbert space restricted to the inner region. $\hat{H}_{el}$ is the $(N+1)$-electron Hamiltonian and $\hat{L}$ is the Bloch operator [116]. The Bloch operator ensures that the operator $\hat{H}_a$ is Hermitian by cancelling the surface terms of the kinetic energy operator at the boundary $r = a$. The eigenfunctions are sought in the form

$$\Psi_k(\boldsymbol{r}_1, \boldsymbol{r}_2, ..., \boldsymbol{r}_{N+1}) = \mathcal{A} \sum_{ij} a_{ijk} \phi_i(\boldsymbol{r}_1, \boldsymbol{r}_2, ..., \boldsymbol{r}_N) u_{ij}(\boldsymbol{r}_{N+1}) + \sum_l b_{lk} \chi_l(\boldsymbol{r}_1, \boldsymbol{r}_2, ..., \boldsymbol{r}_{N+1}), \tag{2.22}$$

where $\phi_i(\boldsymbol{r}_1, \boldsymbol{r}_2, ..., \boldsymbol{r}_N)$ are the electronic states of the target and $u_{ij}(\boldsymbol{r}_{N+1})$ are the continuum-like orbitals which describe the scattered electron within the inner region. The spatial and spin

[3] In a one-dimensional problem, the R-matrix reduces to the logarithmic derivative of the wave function at the boundary of the two regions.

coordinates of the i-th electron are collectively denoted as $\boldsymbol{r}_i$ and the operator $\mathcal{A}$ ensures that the wave functions are anti-symmetric with respect to interchange of any two electrons. In the case of ICD, the electronic states of the target included in the R-matrix calculations are the *final states* of the decay process. The so-called $\mathcal{L}^2$ configurations $\chi_l(\boldsymbol{r}_1, \boldsymbol{r}_2, ..., \boldsymbol{r}_{N+1})$ account for the correlation between the N target electrons and the scattered one and are critical for the description of the Feshbach-type resonances.

In the ansatz (2.22), only the continuum-like orbitals $u_{ij}(\boldsymbol{r}_{N+1})$ extend beyond the boundary $r = a$, which enables to match the $(N + 1)$-electron inner solution with the effectively one-electron wave function in the outer region. The link is provided by the R-matrix

$$R_{ij}(E; a) = \frac{1}{2a} \sum_k \frac{w_{ik}(a) w_{jk}(a)}{E_k - E}, \tag{2.23}$$

where E is the energy of the continuum $N+1$-electron state and the sum runs over all eigenstates defined in Eq. (2.22). The boundary amplitudes $w_{ik}(a)$ for channel i are defined as

$$w_{ik}(a) = \sum_j \alpha_{ijk} u_{ij}(a), \tag{2.24}$$

where the spin coordinates have been summed out, and thus the boundary amplitudes depend only on the spatial coordinates of the scattered particle. It is the key feature of the R-matrix theory that the diagonalization of $\hat{H}_a$ is performed only once. The inner region $(N+1)$-electron problem is independent of the actual energy E of the scattering state [101], which enters the R-matrix (2.23) only as a parameter.

The R-matrix is propagated from the boundary $r = a$ to a larger distance from the centre of mass of the molecule, where it is matched with asymptotic solutions of a known form. This enables to determine the K-matrix, which contains all the information on the scattering process [115]. In particular, the eigenphase sum $\delta(E)$ can be computed as

$$\delta(E) = \sum_i \arctan(k_i), \tag{2.25}$$

where k_i are the eigenvalues of the K-matrix. The total resonance width can then be extracted via fitting $\delta(E)$ in the vicinity of the resonance with a Breit-Wigner profile

$$\delta(E) = \delta_0(E) + \arctan \frac{\Gamma}{2(E_r - E)}, \tag{2.26}$$

where E_r and Γ are the resonance energy and width, respectively. The non-resonant background contribution $\delta_0(E)$ is usually a slowly varying function of energy. The partial widths can be obtained from the time-delay matrix [117, 118]. Alternatively, complex energy poles of the S-matrix associated with the Siegert states can be found directly [119].

In Ref. [A3], we have applied the R-matrix method, as implemented in the UKRmol package [120], to compute ICD widths in the helium dimer following simultaneous ionization and

excitation,

$$\mathrm{He}(1s^2) - \mathrm{He}(1s^2) + h\nu \longrightarrow \mathrm{He}^+(2p) - \mathrm{He}(1s^2) + e_{ph} \longrightarrow \mathrm{He}^+(1s) + \mathrm{He}^+(1s) + e_{\mathrm{ICD}} + e_{ph}. \quad (2.27)$$

This process represents a suitable benchmark system because ICD in this system has been investigated in great detail both theoretically [A9, A10] and experimentally [121, 122]. The results for both the total and partial ICD widths agree satisfactorily with the results of the Fano-ADC(2)x method when equivalent level of correlation model is employed in the R-matrix calculations.

In general, the study confirms that the R-matrix and Fano-ADC are both valuable complementary tools for the computation of electronic decay widths. The R-matrix is expected to perform better for very low energy of the outgoing electrons, when the Fano-ADC method is prone to failure due to the blurred distinction between the open and closed channels. In contrast, Fano-ADC performs better for faster electrons owing to the lower demands on the quality of the basis sets. Furthermore, in larger systems, the eigenphase sum tends to exhibit multiple resonances of different character and their classification based on the eigenphases only is difficult. It can be overcome by employing the so-called Feshbach-Fano R-matrix method [123,124], in which the resonance of interest is analyzed through explicit construction of a suitable discrete state. Owing to the direct evaluation of the energy-dependent level shift matrix, this approach also paves the way to the full description of interacting resonances as well as the description of the nuclear dynamics beyond the LCP approximation.

Diatomics-in-molecules

All the aforementioned *ab initio* methods are computationally expensive and thus not applicable to truly large systems. The simplest way to estimate the interatomic decay widths of metastable states in large clusters is the pairwise additivity approximation, according to which it is given as a sum of the widths obtained considering each neighboring atom separately [125]. In Ref. [126], this simple but efficient approach was used to infer the structure of large NeAr clusters through the comparison of the theoretical and observed ICD electron spectra. The diatomics-in-molecules (DIM) [127, 128] approach also seeks to recover the full information about the complex system from partial information on its atomic and diatomic constituents, but goes beyond the pairwise additivity through taking into account the delocalization of the charges in the decaying as well as the final states. In the context of ICD, We have formulated and tested the method on the example of helium trimer in Ref. [129].

The DIM method is based on the possibility to subdivide the electronic Hamiltonian of the N-atomic system into atomic and diatomic parts [127],

$$\hat{H}_{el} = \sum_{\alpha=1}^{N-1} \sum_{\beta>\alpha}^{N} \hat{H}^{\alpha\beta} - (N-2) \sum_{\alpha=1}^{N} \hat{H}^{\alpha}. \quad (2.28)$$

The atomic fragment $\hat{H}^{\alpha}$ contains kinetic energy operators and intra-atomic potential energy terms which depend exclusively on the coordinates of electrons assigned to the atom α and of the α nucleus itself. The operator $\hat{H}^{\alpha\beta} = \hat{H}^{\alpha} + \hat{H}^{\beta} + \hat{V}^{\alpha\beta}$ is the Hamiltonian of a "diatomic molecule" $\alpha\beta$, containing the atomic contributions plus interatomic potential energy terms depending on the electron and nuclear coordinates common to atoms α and β.

The approximate DIM Hamiltonian is obtained by constructing the DIM basis as antisymmetrized products

$$|\Psi_m^{anti}\rangle = \hat{A}\prod_{\alpha=1}^{N}|\chi_m^{\alpha}\rangle \equiv \hat{A}|\Psi_m\rangle. \tag{2.29}$$

Here, $|\chi_m^{\alpha}\rangle$ are the atomic eigenfunctions,

$$\hat{H}^{\alpha}|\chi_m^{\alpha}\rangle = \epsilon_m^{\alpha}|\chi_m^{\alpha}\rangle, \tag{2.30}$$

m is the generalized index of a molecular basis function, and the operator $\hat{A}$ ensures the antisymmetrization with respect to electrons associated with different atomic fragments. The diatomic Hamiltonian operators $\hat{H}^{\alpha\beta}$ can be expressed in terms of their eigenstates $|\psi_i^{\alpha\beta}\rangle$ and the corresponding eigenvalues $\epsilon_i^{\alpha\beta}$ – adiabatic potential energy functions depending on the interatomic distance $R_{\alpha\beta}$ – as

$$\hat{H}^{\alpha\beta} = \sum_i |\psi_i^{\alpha\beta}\rangle\epsilon_i^{\alpha\beta}\langle\psi_i^{\alpha\beta}|. \tag{2.31}$$

Since $\hat{H}^{\alpha\beta}$ commutes with the antisymmetrization operator, its action on the basis functions $|\Psi_m^{anti}\rangle$ can be expressed as

$$\hat{H}^{\alpha\beta}|\Psi_m^{anti}\rangle = \hat{A}\hat{H}^{\alpha\beta}|\Psi_m\rangle = \hat{A}\sum_i |\Psi_i^{\alpha\beta}\rangle\epsilon_i^{\alpha\beta}\langle\Psi_i^{\alpha\beta}|\Psi_m\rangle. \tag{2.32}$$

We have introduced the N-atomic wave functions $|\Psi_i^{\alpha\beta}\rangle = |\psi_i^{\alpha\beta}\rangle\prod_{\gamma\neq\alpha,\beta}|\chi_i^{\gamma}\rangle$ as products of the diatomic eigenfunctions and the atomic wave functions for the electrons not included in the $\alpha\beta$ diatomic fragment, on which $\hat{H}^{\alpha\beta}$ acts as an identity operator.

The two sets of N-atomic wave functions, $|\Psi_i^{\alpha\beta}\rangle$ and $|\Psi_m\rangle$, are connected by a unitary transformation defined by the overlap matrix $B_{im}^{\alpha\beta} = \langle\Psi_i^{\alpha\beta}|\Psi_m\rangle$. Its elements are readily calculated from the overlap integrals between $|\psi_i^{\alpha\beta}\rangle$ and the atomic wave functions in $|\Psi_m\rangle$ corresponding to the electrons included in the $\alpha\beta$ fragment. In terms of the overlap matrix, the action (2.32) can be recast as

$$\hat{H}^{\alpha\beta}|\Psi_m^{anti}\rangle = \hat{A}\sum_{n,i}|\Psi_n\rangle(B_{in}^{\alpha\beta})^*\epsilon_i^{\alpha\beta}B_{im}^{\alpha\beta} = \sum_{i,n}|\Psi_n^{anti}\rangle(B_{in}^{\alpha\beta})^*\epsilon_i^{\alpha\beta}B_{im}^{\alpha\beta}. \tag{2.33}$$

The DIM basis set (2.29) thus yields the fragment Hamiltonian in the form of a matrix as

$$\boldsymbol{H}^{DIM} = \sum_{\alpha,\beta}(\boldsymbol{B}^{\alpha\beta})^{\dagger}\boldsymbol{\epsilon}^{\alpha\beta}\boldsymbol{B}^{\alpha\beta} - (N-2)\sum_{\alpha}\boldsymbol{\epsilon}^{\alpha}, \tag{2.34}$$

where $\boldsymbol{\epsilon}^{\alpha}$ and $\boldsymbol{\epsilon}^{\alpha\beta}$ are diagonal matrices constructed from the atomic energies (2.30) and the diatomic adiabatic potential energy functions (2.31). These input quantities are obtained from many-electron *ab initio* calculations for all non-equivalent atomic and diatomic subsystems, which are of manageable size. The polyatomic potential energy surfaces are then obtained via diagonalization of the DIM Hamiltonian (2.34). Its size depends on the truncation of the basis (2.29) but generally can be kept small.

Generalization of the DIM method to encompass the metastable states is again based on the projection operator approach [129]. The DIM basis set (2.29) is divided into two subsets, $\mathcal{Q}$ and $\mathcal{P}$. The former corresponds to excited states of the cluster in which all electrons are bound, and the latter contains continuum (or continuum-like) functions associated with the final states of the decay. To illustrate the procedure, consider ICD in a N-atomic rare-gas (Rg) cluster following inner valence ionization,

$$(\mathrm{Rg}^{+*} - \mathrm{Rg}_{N-1}) \longrightarrow (\mathrm{Rg}^{+} - \mathrm{Rg}^{+} - \mathrm{Rg}_{N-2}). \tag{2.35}$$

In this case, the $\mathcal{Q}$ subspace is built from the Rg, Rg^{+*} atomic, and (Rg – Rg), (Rg^{+*} – Rg) diatomic fragments and the DIM Hamiltonian matrix is given by Eq. (2.34) using the corresponding atomic energies and diatomic potential energy functions. Its eigenvectors define the manifold of the adiabatic N-atomic metastable states. Similarly, the final states DIM matrix is constructed from energies corresponding to atomic and diatomic states found in the final doubly-ionized states of the cluster. Namely, the input data needed for the final state manifold DIM matrix are the energies of the neutral Rg and singly ionized Rg^{+} states of atomic fragments, and the potential energy functions corresponding to neutral (Rg−Rg), singly ionized (Rg^{+} – Rg) and two-site doubly-ionized (Rg^{+} – Rg^{+}) states of the diatomic fragments.

The decay widths of the metastable states are given by the block of Hamiltonian matrix that couple the $\mathcal{Q}$ and $\mathcal{P}$ subspaces. Its DIM representation is given by a formula analogous to (2.34), but the $\boldsymbol{\epsilon}^{\alpha}$ and $\boldsymbol{\epsilon}^{\alpha\beta}$ diagonal matrices are replaced by matrices derived from the couplings between the decaying and the continuum final states of all atoms and all pairs of atoms forming the cluster, which is well within reach of the *ab initio* methods discussed in the present section. Application of the approach to ICD in helium trimer confirmed good quantitative agreement with full Fano-ADC(2)x calculations over a large set of geometries for the total and the dominant partial decay widths. Significant discrepancies were only found for some weak channels and were explained by strong three-body effects not accounted for in the DIM method [129].

Chapter 3

Interatomic decay processes in clusters

In Chap. 2, we have introduced a few high-level *ab initio* methods for computation of electronic decay widths of metastable states, which are applicable to atoms, molecules and their aggregates. In the present chapter, we discuss some representative applications to interatomic decay processes in rare gas clusters in order to unveil the mechanisms driving the electronic transitions in weakly bound clusters, and to demonstrate their general characteristics. We start by a qualitative analysis of ICD widths at the lowest order of PT. With the help of advanced *ab initio* calculations, we then explore the limits of the lowest order approximation and explore some related decay mechanisms, such as superexchange or multi-electron decay modes. The last section is devoted to the role of nuclear dynamics, which is demonstrated on some illustrative examples. In particular, strong non-adiabatic effects are identified in a previously unpublished analysis of ICD of shake-up ionization satellites in Ar_2.

3.1 Decay mechanisms

While the high-level *ab initio* methods are indispensable to provide a quantitatively correct description of the decay process, to understand the driving mechanism of ICD it is best to resort to the lowest order PT.[1] It leads to the well-known golden rule formula for the decay width [106, 131]

$$\Gamma = 2\pi \sum_F |\langle I|\hat{H}|F\rangle|^2 \delta(E_F - E_I), \tag{3.1}$$

where $|I\rangle$ and $|F\rangle$ represent the initial and final states, respectively. Despite the apparent similarity to the decay width (2.5) in the Fano theory, the two approaches are fundamentally different. In the latter, the decay width is a function of the final state energy and the theory is in principle exact. PT approach, on the other hand, requires energy conservation and Eq. (3.1) can be regarded as the lowest order estimate of the imaginary part of the Siegert energy.

ICD following an inner-valence (iv) ionization in a dimer AB is schematically represented in Fig. 3.1. In order to apply the golden rule formula, the electronic Hamiltonian is partitioned

[1] In the context of the decay processes, the approach is known as the Wigner-Weisskopf theory [130].

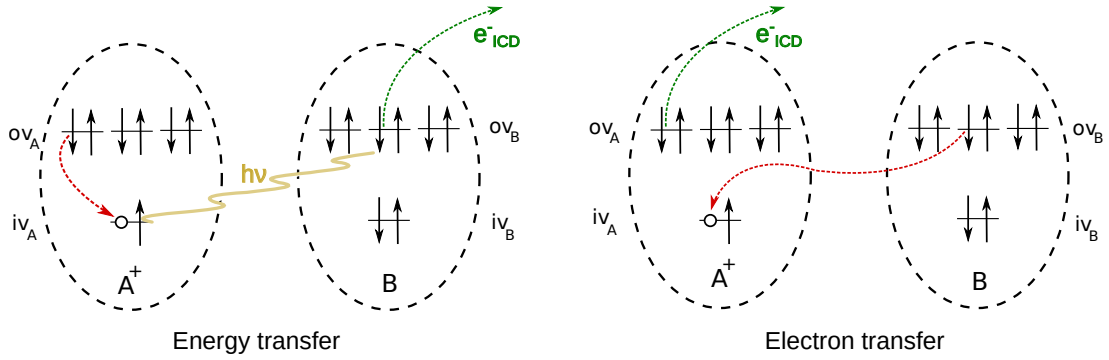

Figure 3.1: Energy and electron-transfer pathways of ICD.

as

$$\hat{H} = \hat{H}_0 + \hat{H}_I = \hat{F} + \hat{V}_C - \hat{V}^{(\mathrm{HF})}, \tag{3.2}$$

where $\hat{H}_0 = \hat{F}$ is the Fock operator and $\hat{H}_I = \hat{V}_C - \hat{V}^{(\mathrm{HF})}$ is the residual Coulomb interaction given as the difference between the full two-electron Coulomb operator $\hat{V}_C$ and the one-electron HF mean-field interaction $\hat{V}^{(\mathrm{HF})}$. At the lowest order of PT, the initial and final states are represented by the HF configurations (2.7) derived from the N-electron HF ground state $|\Phi_0\rangle$. Namely, the inner-valence vacancy state is $|I\rangle = c_{iv_A}|\Phi_0\rangle$, and the final two-site doubly outer-valence (ov) ionized state plus the continuum electron with momentum $\boldsymbol{k}$ is $|F\rangle = c^\dagger_{\boldsymbol{k}} c_{ov_A} c_{ov_B}|\Phi_0\rangle$.

Since the two states differ in four HF orbitals, they are coupled only by the full Coulomb operator $\hat{V}_C$, but not by the mean-field operator $\hat{V}^{(\mathrm{HF})}$. Defining the Coulomb integrals in the "1212" notation as

$$\langle ik|V|jl\rangle = \int d\boldsymbol{r}_1 d\boldsymbol{r}_2\, \varphi_i^*(\boldsymbol{r}_1)\varphi_k^*(\boldsymbol{r}_2)\frac{e^2}{|\boldsymbol{r}_1 - \boldsymbol{r}_2|}\varphi_j(\boldsymbol{r}_1)\varphi_l(\boldsymbol{r}_2). \tag{3.3}$$

and taking into account the anti-symmetry of $|\Phi_0\rangle$ with respect to the exchange of electrons, the coupling matrix element in Eq (3.1) reads

$$\langle I|\hat{H}|F\rangle = \langle \varphi_{iv_A}\varphi_{ov_B}|V|\varphi_{ov_A}\varphi_{\boldsymbol{k}}\rangle - \langle \varphi_{iv_A}\varphi_{ov_A}|V|\varphi_{ov_B}\varphi_{\boldsymbol{k}}\rangle. \tag{3.4}$$

The two terms – the direct and exchange integrals – are visualized in the left and right panels of Fig. 3.1, respectively, and can be interpreted as the energy and the electron transfer pathways of the decay process.

Long-range dependence of the decay width on the distance R between the two monomers can be inferred from the expansion of the Coulomb operator in terms of inverse powers of R [106],

$$\frac{1}{|\boldsymbol{r}_1 - \boldsymbol{r}_2|} = \frac{1}{R} - \frac{\boldsymbol{u}_R \cdot (\boldsymbol{x}_1 - \boldsymbol{x}_2)}{R^2} + \frac{3(\boldsymbol{u}_R \cdot (\boldsymbol{x}_1 - \boldsymbol{x}_2))^2 - (\boldsymbol{x}_1 - \boldsymbol{x}_2)^2}{2R^3} + O\left(\frac{1}{R^4}\right). \tag{3.5}$$

Here, $\boldsymbol{u}_R = (\boldsymbol{R}_1 - \boldsymbol{R}_2)/R$ is the unit vector along the line connecting the centers of mass of the two monomers residing at positions $\boldsymbol{R}_1$ and $\boldsymbol{R}_2$, $\boldsymbol{r}_i$ are the coordinates of the two involved

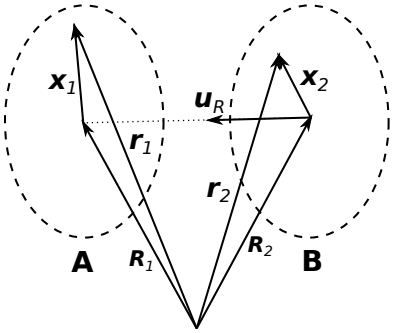

Figure 3.2: Vectors and notation used in the Eq. (3.5).

electrons, and $\boldsymbol{x}_i = \boldsymbol{r}_i - R_i$ are their coordinates relative to the respective nuclei, see Fig. 3.2. At large distances, the bound spin-orbitals $\varphi_j(\boldsymbol{r}_i)$ appearing in Eq. (3.4) are localized either on the monomer A or B with negligible mutual overlap. Furthermore, the orbitals localized on the same monomer are orthogonal, i.e., $\langle\varphi_{iv_A}|\varphi_{ov_A}\rangle = \langle\varphi_{ov_B}|\varphi_{\boldsymbol{k}}\rangle = 0$. In this regime, the electron transfer contribution is zero and the first non-vanishing contribution to the energy-transfer integral arises from the term proportional to R^{-3},

$$\langle\varphi_{iv_A}\varphi_{ov_B}|V|\varphi_{ov_B}\varphi_{\boldsymbol{k}}\rangle \approx \frac{e^2}{R^3}\left(\langle\varphi_{ov_A}|\boldsymbol{x}_1|\varphi_{iv_A}\rangle \cdot \langle\varphi_{ov_B}|\boldsymbol{x}_2|\varphi_{\boldsymbol{k}}\rangle \right. \\ \left. - 3\langle\varphi_{ov_A}|\boldsymbol{x}_1 \cdot \boldsymbol{u}_R|\varphi_{iv_A}\rangle\langle\varphi_{ov_B}|\boldsymbol{x}_2 \cdot \boldsymbol{u}_R|\varphi_{\boldsymbol{k}}\rangle\right). \quad (3.6)$$

This formula corresponds to the interaction of two electric dipoles located at the individual monomers. In the case of an atomic cluster, it can be expressed in terms of purely atomic quantities, leading to the so-called virtual photon transfer model for the decay width [132,133],

$$\Gamma(R) = \frac{3\hbar}{4\pi}\left(\frac{c}{\omega}\right)^4 \frac{\tau_A^{-1}\sigma_B}{R^6}. \quad (3.7)$$

Here, ω is the frequency corresponding to the recombination transition $A^+(iv^{-1}) \to A^+(ov_A^{-1})$, τ_A is the radiative lifetime of the inner-valence vacancy state $A^+(iv^{-1})$ in an isolated atom, and σ_B is the total photoionization cross-section of the atom B at the energy $\hbar\omega$. If the recombination transition is dipole-forbidden for symmetry reasons, even the R^{-3} term in Eq. (3.5) vanishes and the leading contribution stems from the quadrupole-dipole interaction. For instance, the Zn $3d$ vacancy in BaZn dimer can only recombine with the $4s$ electron and the corresponding ICD width thus decreases asymptotically as R^{-8} or even R^{-10}, depending on the magnetic quantum number [133].

The golden rule formula provides even deeper insight into the long-range behaviour of the ICD widths. In Ref. [134], we have generalized the above approach and derived analytical expressions for the energy-transfer contributions to the coupling elements (3.4), explicitly taking into account the symmetry of the involved many-electron states $|I\rangle$ and $|F\rangle$. In the simplest possible scenario, Eq. (3.6) can be related to a classical quantity – the interaction energy between two dipoles $\boldsymbol{p}_1$ and $\boldsymbol{p}_2$ at the distance R,

$$W = \frac{\boldsymbol{p}_1 \cdot \boldsymbol{p}_2 - 3(\boldsymbol{u}_R \cdot \boldsymbol{p}_1)(\boldsymbol{u}_R \cdot \boldsymbol{p}_2)}{R^3}. \quad (3.8)$$

In particular, if both dipoles are aligned parallel to $\boldsymbol{u}_R$, the interaction energy is twice that of the dipoles parallel to each other but perpendicular to $\boldsymbol{u}_R$ and this ratio is independent of the separation.

This result is exemplified by ICD of the Ca $3p$ vacancy in CaHe dimer,

$$\mathrm{Ca}^+(3p^{-1})\mathrm{He} \;\rightarrow\; \mathrm{Ca}^+(4s^{-1}) + \mathrm{He}^+(1s^{-1}) + e^-. \tag{3.9}$$

The decaying state is derived from the triply degenerate $^2P^0$ atomic term of the $\mathrm{Ca}^+(3p^{-1})$ cation and the ^1S ground state of He. In the dimer, it splits into non-degenerate $^2\Sigma^+$ and doubly degenerate $^2\Pi$ molecular states, with the dipole moments oriented parallel and perpendicular to the dimer axis, respectively. Symmetry-induced selection rules for the $\langle I|\hat{H}|F\rangle$ matrix elements imply that the induced dipoles on He will be in both cases parallel to the transition dipole on the Ca atom. Formula (3.8) thus predicts the ratio $\Gamma_\Sigma/\Gamma_\Pi = 4$ between the ICD widths of the $^2\Sigma$ and $^2\Pi$ states, regardless the internuclear distance. This result is indeed corroborated by *ab initio* calculations [125]. In this example, there is only a single final dicationic state available for the decay process. If several final states are accessible, the corresponding transitions have to be considered separately, resulting in more complicated formulae for the ratios of the ICD widths for metastable states of different symmetry [134]. Apart from providing a deeper understanding of the mechanism of the interatomic decay, these considerations can also serve as a test of the consistency of the correlation model employed in quantitative *ab initio* methods.

For smaller internuclear separations, deviations from the asymptotic formulae occur. In this regime, the electronic transitions at the donor and acceptor atoms can no longer be accurately characterized by quantities associated with isolated atoms as they are significantly influenced by the neighboring cluster constituents. Furthermore, the assumption of a negligible overlap of spin-orbitals localized on different monomers is not valid and the electron transfer decay pathway becomes operative. Its strength is then predominantly determined by the overlap integrals of the type $\langle\varphi_{iv_A}|\varphi_{ov_B}\rangle$, which decreases exponentially with the increasing interatomic distance due to the Slater-type character of the atomic orbitals. Therefore, the dependence of the interatomic decay width for the dipole-allowed transition assumes the general form

$$\Gamma \propto \frac{1}{R^6}\left(1 + P(R)e^{-\alpha R}\right), \tag{3.10}$$

where $P(R)$ is some polynomial, and we can expect an enhancement of the decay widths at small interatomic distances due to the electron transfer-driven transitions. Even the energy transfer contributions will be altered due to the distortion of the atomic spin-orbitals in the areas of overlapping electron density. Exact behavior of the decay widths can then only be recovered by advanced *ab initio* methods such as Fano-ADC.

Representative examples of ICD widths in singly and doubly ionized NeAr and NeMg dimers are shown in Figs. 3.3 and 3.4, respectively. In both cases, we study equivalent metastable states characterized by the Ne $2s$ inner-valence vacancy. In NeAr, the total ICD widths of all considered states follow the R^{-6} trend over the whole range of interatomic distances. In contrast, in

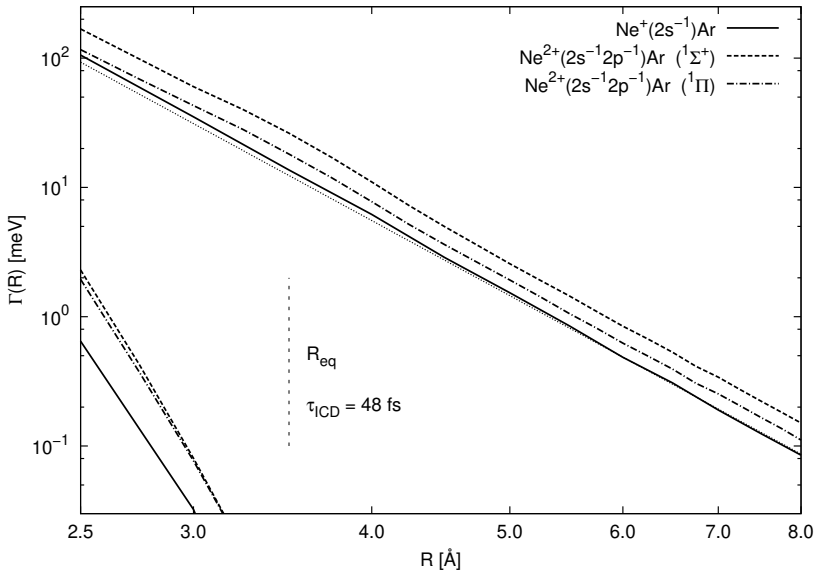

Figure 3.3: Double-logarithmic plot of total interatomic decay widths and the ETMD partial widths (steeply decreasing curves in the lower left corner) of the $Ne^{2+}(2s^{-1}2p^{-1})Ar$ ($^1\Sigma, ^1\Pi$) doubly ionized states (dashed and dashed-dotted lines), compared to the reference ICD width Γ^{2s} of the $Ne^{+}(2s^{-1})Ar$ ($^2\Sigma$) state (solid line). The dotted straight line shows R^{-6} dependence fitted to the latter. The indicated lifetime corresponds to Γ^{2s} at the equilibrium geometry of the neutral cluster. Reprinted with permission from Ref. [A2] (Copyright 2008 AIP Publishing).

the NeMg dimer, the ICD widths exhibit significant enhancement relative to the long-distance asymptote, starting already at around twice the equilibrium internuclear distance of the neutral dimer. However, the difference between the two systems is not caused primarily by a strong electron transfer transitions in NeMg, but rather by a weaker energy transfer. Indeed, at the virtual photon energy $E[\mathrm{Ne}^+(2s^{-1})\,^2S] - E[\mathrm{Ne}^+(2p^{-1}\,^2P)] = 26.9\,\mathrm{eV}$, the photoionization cross sections are $\sigma_{\mathrm{Mg}} = 0.26\,\mathrm{Mb}$ and $\sigma_{\mathrm{Ar}} = 31\,\mathrm{Mb}$ for Mg and Ar, respectively [135]. Thus, in NeAr, the contribution from electron transfer transitions is veiled by the efficient energy transfer even for the shortest interatomic distance.

The actual strength of the electron transfer transitions can be assessed by studying the electron-transfer mediated decay (ETMD) [136]. In ETMD, an electron is transferred from a neighboring monomer (donor) to fill the initial vacancy while another electron is emitted to the continuum from the donor [ETMD(2)] or even a third monomer [ETMD(3)]. In a dimer, only the ETMD(2) process is available,

$$\mathrm{A}^+(iv^{-1})\mathrm{B} \rightarrow \mathrm{AB}^{2+}(ov^{-2}) + e^-. \tag{3.11}$$

The ETMD channels are thus characterized by the initially ionized atom being neutral and both charges being localized on the neighbour. Because these channels are only accessible via electron transfer, corresponding partial decay widths decrease exponentially with increasing interatomic distance, see the steep curves in the lower left corners in Figs. 3.3 and 3.4. At the respective equilibrium interatomic distances, the ETMD widths are $5.10^{-4}\,\mathrm{meV}$ in NeAr and

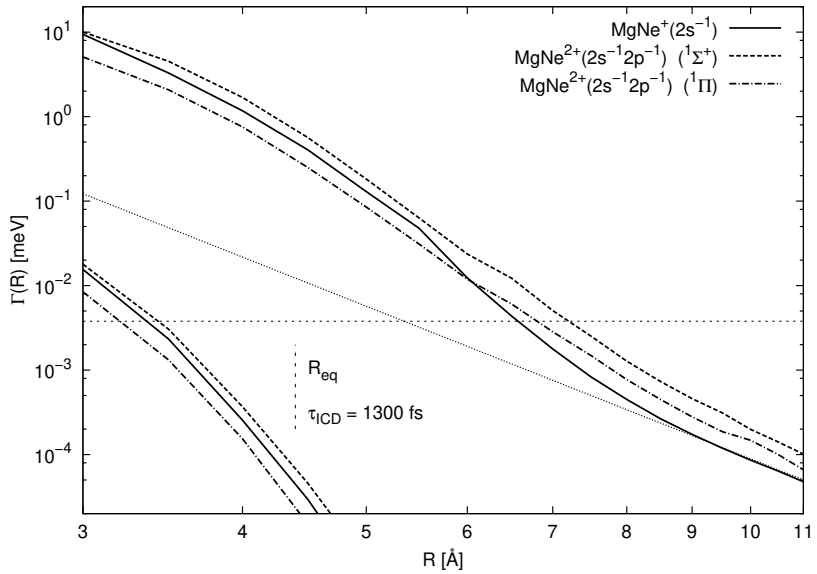

Figure 3.4: Double-logarithmic plot of total interatomic decay widths and the ETMD partial widths (steeply decreasing curves in the lower left corner) of the $Ne^{2+}(2s^{-1}2p^{-1})Mg$ ($^1\Sigma$, $^1\Pi$) doubly ionized states (dashed and dashed-dotted lines), compared to the reference ICD width Γ^{2s} of the $Ne^{+}(2s^{-1})Mg$ ($^2\Sigma$) state (solid line). The dotted straight line shows R^{-6} dependence fitted to the latter. The indicated lifetime corresponds to Γ^{2s} at the equilibrium geometry of the neutral cluster. Reprinted with permission from Ref. [A2] (Copyright 2008 AIP Publishing).

3.10^{-5} meV in NeMg. Related to the number of available ETMD channels, the electron transfer transition is actually about six times stronger in NeAr than in NeMg.

As demonstrated by the above examples, ETMD is typically unimportant once the competing ICD channels are accessible. The significance of ETMD increases for very low-energy excitations when the process becomes the only non-radiative relaxation pathway. Such a situation occurs, for instance, in rare gas clusters in which neon is mixed with heavy atoms such as Kr or Xe. When multiply charged Ne ions are produced by the Auger decay of Ne $1s$ vacancy, ETMD then provides a particularly efficient neutralization pathway for the majority of those ions, even for Ne^{2+} in its ground state electronic configuration $2p^{-2}$ [A12] [98]. In NeKr clusters, for instance, ETMD(3) channel is open for relaxation of the $Ne^{2+}(2p^{-2})$ double vacancy states,

$$Ne^{2+}(2p^{-2}\,{}^1S, {}^1D)Kr_2 \longrightarrow Ne^{+}(2p^{-1}) + Kr^{+}(4p^{-1}) + Kr^{+}(4p^{-1}). \tag{3.12}$$

Complex cascades of relaxation steps bringing the core ionized neon inside the NeKr cluster to its ionic ground state $Ne^{+}(2p^{-1})$, which involve Auger decay and both the ICD and ETMD transitions, were observed by You *et al.* [11]. Because of the stronger dependence of the ETMD widths on the cluster geometry and longer characteristic lifetimes (one or two orders of magnitude longer than for ICD), the influence of the nuclear dynamics is much stronger than in ICD. We will return to this topic in Sec. 3.2.

Superexchange mechanism

In our discussion of the interatomic decay mechanisms up to now, we have taken into account only those cluster subunits that play an active role in the process. In Ref. [A4], we investigated how the energy transfer between two monomers can be influenced by the presence of ICD inactive neighbors, i.e., atoms or molecules whose ionization potential is higher than the excess energy available at the initially excited subunit. As a showcase system, we considered the decay of the $Ne^+(2s^{-1})Ne\ ^2\Sigma^+_{g/u}$ resonances in the presence of a helium atom.[2] We demonstrated that, in the NeHeNe trimer, ICD efficiency can be significantly enhanced through the coupling to the virtual states of the helium atom, which plays a role of a mediator facilitating the energy transfer. In the context of the Förster fluorescence resonance energy transfer, such an energy transfer mediated by bridge molecules is known as superexchange mediated coupling [138, 139]. We thus call the related interatomic decay mechanism superexchange ICD (SE-ICD). Recently, SE-ICD in nanostructures was investigated using a simple model for coupled quantum dots [140], confirming the enhanced efficiency of the energy transfer process, independent of the exact characteristics of the bridge dot.

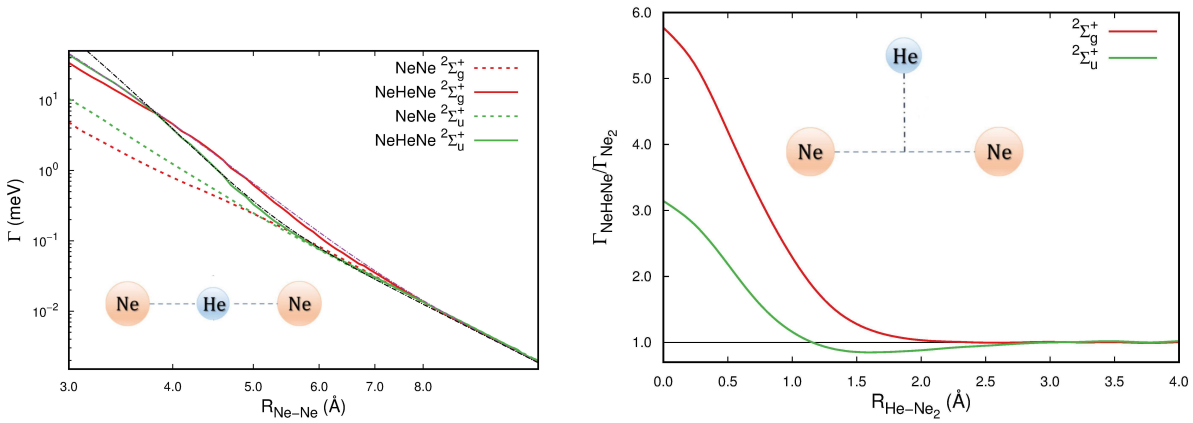

Figure 3.5: Left panel: total decay widths of the $^2\Sigma^+_g$ and $^2\Sigma^+_u$ states of $Ne^+(2s^{-1})HeNe$ (full lines) and of $Ne^+(2s^{-1})Ne$ (dashed lines) as functions of the distance R between the two Ne atoms. Geometry of the NeHeNe trimer is linear with the helium atom at the center of mass. Dashed-dotted lines show fit of the *ab initio* results (purple – $^2\Sigma^+_g$; black – $^2\Sigma^+_u$) via the approximate expression (3.13). **Right panel:** enhancement of the total decay widths of the $^2\Sigma^+_g$ (red) and $^2\Sigma^+_u$ (green) states of $Ne^+(2s^{-1})$ in the NeHeNe relative to the Ne_2 dimer. The trimer is in T-shape geometry with the distance between the neon atoms fixed at 4 Å and a variable distance R_{He-Ne_2} between He and center of mass of Ne_2.

Total decay widths of the $Ne^+(2s^{-1})$ resonance in the NeHeNe trimer (linear geometry) and the Ne_2 dimer as functions of the distance between the Ne atoms, calculated by the Fano-ADC(2)x method, are compared in the left panel of Fig. 3.5. The decay widths in the trimer and the dimer coincide at large distances ($R_{Ne-Ne} > 7$ Å), while at shorter distances the SE-ICD

[2] As shown in Ref. [137], ICD between Ne and He is energetically closed for the interatomic separations shorter than 6.2 Å.

mechanism becomes operative and enhances the decay width in the trimer. The mechanism can be visualised in the energy level diagram in Fig. 3.6. It shows two possible pathways from the initial inner-valence ionized $Ne^+(2s^{-1})HeNe$ state to the ICD final states $Ne^+(2p^{-1})HeNe^+(2p^{-1})$ – the direct and SE ICD. In the latter, which is only available in the trimer, the transition occurs through the coupling to the intermediate virtual states of the mediator, corresponding to the ionic configurations of the type $Ne^+(2p^{-1})He^-Ne^+(2p^{-1})$. More detailed analysis of the SE mechanism and its strength in individual decay channels is available in the followup work [A5]. There, we also show that the SE mechanism is weaker in the NeHeAr trimer due to the increased energy distance between the bridge states and the resonance.

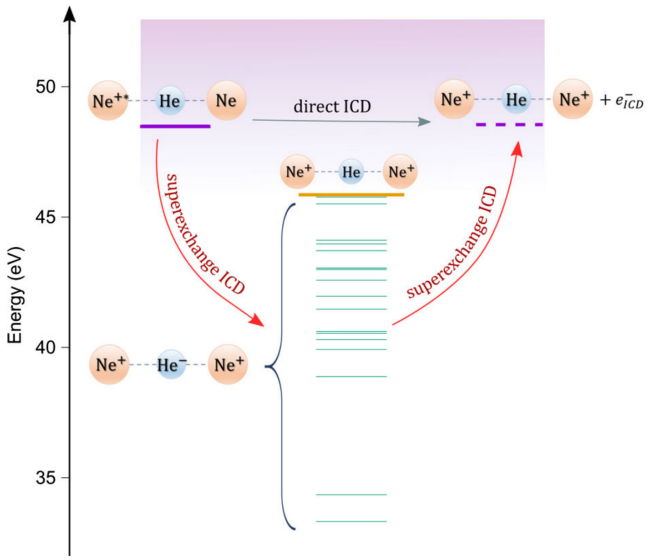

Figure 3.6: Energy level diagram representing the direct and superexchange ICD pathways. The initial and finals states (purple) are shown to the left and right of the diagram, respectively. The purple shaded area indicates that the states are embedded in a continuum. The intermediate states $Ne^+(2p^{-1})He^-Ne^+(2p^{-1})$ are shown in green, together with the corresponding ionization threshold (orange). Note that although isolated He cannot bind an electron to form He^-, in the presence of two neighboring cations the $He^-(1s^2nl)$ anion is stable. Reprinted with permission from Ref. [A4] (Copyright 2017 APS).

Employing a procedure similar to the derivation of the virtual photon model and neglecting the interference between the direct and SE pathways, it is possible to derive an approximate formula for the ICD width as a function of the distance R between the two neon atoms in the form [A4]

$$\Gamma(R) \approx \frac{A}{R^6} + B\frac{e^{-CR}}{R^4}. \tag{3.13}$$

The first and second terms correspond to the dipole-allowed direct and the SE decay pathways, respectively. The exponential factor originates from the overlap integral between the occupied orbitals of Ne_2 and the virtual orbitals of He. The coefficient B depends on the inverse of the energy difference between the initial and intermediate states, and includes the coupling between $He^-(1s^2nl)$ and $He + e^-$ states of the mediator, as well as the Ne transition dipole moment

appearing in the R^{-2} term in the expansion (3.5) of the Coulomb operator. All these factors are of the intra-atomic nature and depend only weakly on the interatomic distance.

In Fig. 3.5, the coefficients A, B and C are fitted to the *ab initio* decay widths and the approximation is shown by the dashed-dotted curves. For shorter interatomic distances, the *ab initio* widths are smaller for both symmetries, indicating that the assumptions leading to Eq. (3.13) are no longer valid, namely the independence of B on the interatomic distance. Recently, we derived another virtual photon model of three-body ICD in the framework of macroscopic quantum electrodynamics [A6]. While it cannot account for the intermediate charge transfer states like $\mathrm{Ne}^+(2p^{-1})\mathrm{He}^-\mathrm{Ne}^+(2p^{-1})$ in the present example, it makes it possible to take into account retardation connected with the finite speed of light, as well as to study the effects of the dielectric properties of a macroscopic environment [141]. The framework thus complements the usual quantum mechanical approaches.

An ICD inactive environment can also suppress the decay process, in particular through the interference of the direct and mediated pathways. This phenomenon is demonstrated in the right panel of Fig. 3.5. In the T-shape geometry of the NeHeNe trimer, the total decay width of the $\mathrm{Ne}^+(2s^{-1})\mathrm{Ne}\ ^2\Sigma_u^+$ state is slightly reduced if the distance of the He atom from the center of mass of the neon dimer is larger than 1.2 Å. However, the deviations of the *ab initio* decay widths from the fitted formula (3.13), shown in the left panel of Fig. 3.5, cannot be attributed to the interference of the two decay pathways – the virtual photon model shows that, in the linear geometry of the trimer, the interference is always constructive [A6]. Stronger effects of the interference – superexchange blocade – are predicted for quantum dots [142]. In general, the findings discussed in the present section indicate that it is possible to control the relaxation processes through manipulation of the environment, which might be useful for the development of nanoscale technologies.

Higher-order decay pathways

Besides two-electron processes like Auger decay or ICD, in which the inner vacancy is refilled by an outer shell electron and another electron is emitted to the continuum, electron correlation can give rise also to higher-order processes involving multi-electron transitions. Basic examples include simultaneous two-electron emission upon recombination of an inner-shell vacancy (double Auger decay [94] or double ICD [143]) or collective decay of two holes with emission of a single electron (collective Auger decay [144, 145] or collective ICD [A8] [146]). Recently, even four-electron Auger decay was unambiguously identified in carbon ions [147]. In the review [148], we have given a comprehensive overview, covering multi-electron relaxation phenomena in systems of diverse complexity, from double Auger decay in atoms to collective autoionization processes in nanoscale samples.

Although the higher order decay processes are often of very low relative intensity, under favourable conditions they can become significant or even dominant decay channels. Recent

systematic investigation covering a large number of molecules showed that the triple ionization can make up as much as 25% of the decay following formation of a single core hole [149]. It was found that the proportion of triple ionization increases linearly with the number N_{ve} of available valence electrons on the atom bearing the initial core hole and its closest neighbours. This trend reflects the simple fact that the number of decay channels grows with the number of valence electrons approximately like N_{ve}^2 and N_{ve}^3 for normal and double Auger decay, respectively.

Double inner-valence ionization of molecules is another situation in which multi-electron processes can play an important role. For instance, the energy of doubly F 2s ionized fluoromethane is well above the triple ionization threshold but all decay channels with at least one F 2s vacancy are energetically closed. Therefore, the collective Auger decay (CAD) represents the only available radiationless relaxation mechanism. Our joint experimental and theoretical study [A7] shows that it not only outpaces the competing radiative decay, but that the CAD rate is well within the range of a typical two-electron Auger decay. Specifically, Fano-ADC(2)x method predicts a lifetime of about 3 fs at the equilibrium geometry of the molecule.

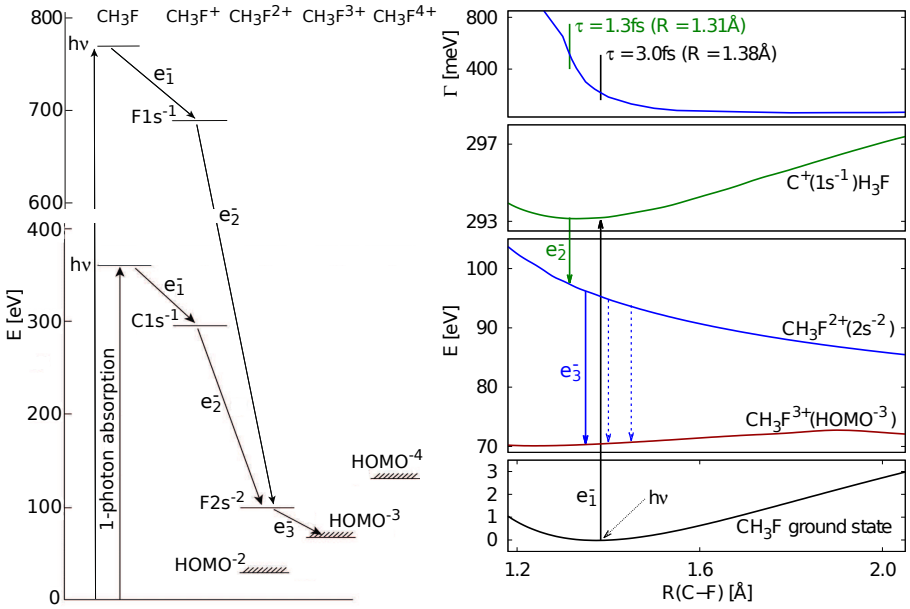

Figure 3.7: Schematic representation of CAD in fluoromethane triggered by the C 1s core ionization. **Left panel:** Energy levels of ionized CH_3F involved in the three-electron transition after initial creation of a core C 1s or F 1s vacancy. HOMO stands for the highest occupied molecular orbital. **Right panel:** PESs along the C-F bond for the states relevant for the C 1s Auger decay initiated-cascade. Reproduced with permission from [A7] (Copyright 2016 APS).

Although the lifetime is not a directly measurable quantity, this striking theoretical result can still be corroborated experimentally exploiting the nuclear dynamics induced by the ionization as a natural clock. The process as realized in the experiment is schematically shown in Fig. 3.7. First, the molecule is photoionized, creating the C 1s core-hole state. The molecule starts to contract along the C-F bond until the subsequent Auger decay takes place. The F $2s^{-2}$ double-vacancy state of interest is populated with a probability of about 0.15%. The relevant

events are selected by detecting the secondary Auger electron with the energy around 195 eV. Contrary to the core-ionized state, the corresponding PES is dissociative and the C-F bond elongates. Ultimately, the double-vacancy state relaxes via CAD into one of the large number of accessible triply ionized states of the molecule.

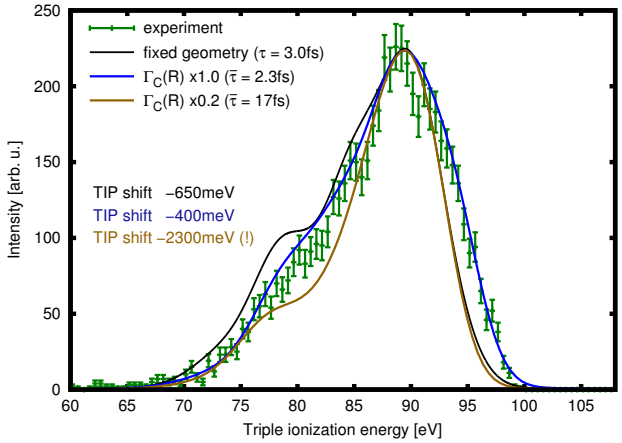

Figure 3.8: Comparison of experimental (green errorbars) and calculated (solid lines) triple ionization spectra resulting from the cascade initiated by C 1s core ionization of the CH_3F molecule. The black curve shows spectrum calculated at the fixed equilibrium geometry. Blue spectrum was obtained with the inclusion of nuclear motion along the C-F bond with the *ab initio* decay width. Light brown curve was calculated in the same way but with the decay width scaled down by a factor of 5. The calculated spectra are shifted in energy to match the maximum of the experimental data.

Resulting triple ionization spectrum is shown in Fig. 3.8, where the experimental data are compared to three theoretical simulations. The spectra are sensitive to the decay rate since slower decay samples a wider range of C-F bond length, and the energies of the secondary electrons depend on molecular geometry. We observe that the inclusion of nuclear dynamics along the C-F bond improves considerably the agreement between the theory and experiment compared to the fixed nuclei calculation, both in the shape and the position of the maximum [see the triple ionization potential (TIP) shift indicated in the figure]. The simulated effective lifetime is $\bar{\tau} = 2.3$ fs, even shorter than at the equilibrium geometry. However, accentuating the dynamics further through scaling down the decay rate significantly deteriorates the agreement, supporting strongly the predicted short lifetime of the F $2s^{-2}$ double-vacancy state. The agreement between the theory and experiment is somewhat worse for the cascade initiated by the F 1s core ionization, which is attributed to opening of the two-electron Auger decay channels, not included in the simulations. For more details on the calculations, the reader is referred to [A7].

The reason for the rapid CAD can be traced to efficient configuration mixing in both the initial and final states of the process [A7] [148]. In the frozen-orbital single-configuration picture, the main two-hole configuration representing the initial state is not coupled directly to the final states characterized by three holes and an electron in the continuum. However, admixture of the shake-up type configurations in the initial state wave function changes the situation

dramatically by making the CAD transition partially allowed. Similarly, in the final state wave functions, the configurations with three outer-valence holes are mixed with those possessing the F $2s$ inner-valence hole, further contributing to the direct coupling of the correlated initial and final states.

Despite the significantly weaker correlation in van der Waals or other weakly bound complexes as compared to molecules, interatomic higher-order pathways can play an important role among relaxation mechanisms even in such environments. Interatomic collective autoionization has been shown to be dominant in resonantly irradiated helium clusters due to the formation of a plasma-like state [150, 151]. Double ICD was proposed [143] and observed [152] to be a viable decay mechanism in endohedral fullerenes due to an enormous number of available decay channels. In another recent experiment with alkali dimers embedded in helium droplets, double ICD was found to be also a very strong mechanism, occurring with efficiency comparable to if not exceeding that of regular ICD [153].

In 2009, we have studied the relevance of collective ICD of multiple vacancies in van der Waals clusters [A8]. For instance, following $4s$ ionization of two neighbouring Kr atoms in mixed KrAr clusters, the process

$$(\mathrm{Kr}^+)_2(4s^{-1}, 4s^{-1})\mathrm{Ar} \longrightarrow \mathrm{Kr}^+(4p^{-1}) + \mathrm{Kr}^+(4p^{-1}) + \mathrm{Ar}^+ + e^- \tag{3.14}$$

can occur without a competition from regular ICD due to the very low initial excitation energy. Similar situation arises in a variety of multiply inner-valence ionized clusters, namely those containing nonmetal hydrides (HCl, HBr, H_2S, ...) or small hydrocarbons. Still, collective ICD can be quenched by the dissociative nuclear dynamics of the multiply ionized cluster as the corresponding decay rate quickly decreases with increasing interatomic distance and, ultimately, the radiative decay of the Kr $4s$ vacancies prevails. At the equilibrium geometry of the Kr_2Ar trimer, the rate associated with the collective process (3.14) predicated by the Fano-ADC(2)x method is $3 \times 10^{12}\,\mathrm{s}^{-1}$, five orders of magnitude faster than that of the radiative decay. The corresponding lifetime of about 300 fs, however, is indeed comparable or even longer than characteristic times associated with nuclear motion. Still, through the explicit simulation of the wave packet evolution along the critical dissociative Kr-Kr bond, we have shown that the collective ICD yields range from 30% to 65%, depending on the mechanism of the initial double ionization [A8].

Similar collective transitions can occur without competition from cluster disintegration if the cluster is initially multiply excited rather than ionized [154] of if the two inner-valence vacancies are localized on a single atom. The three-electron decay

$$\mathrm{NeAr}^{2+}(3s^{-2}\,{}^1S) \longrightarrow \mathrm{Ne}^+(2p^{-1}\,{}^2P) + \mathrm{Ar}^+(3p^{-2}\,{}^3P) + e^- \tag{3.15}$$

was indeed observed by Ouchi *et al.* [146], despite the fact that in this particular transition the efficient energy transfer mechanism is forbidden due to the spin selection rules and the process can proceed only via electron exchange between the two atoms. All those findings confirm

that multi-electron relaxation processes can contribute substantially to the accumulation and redistribution of charges in matter exposed to ionizing radiation, which should motivate further theoretical and experimental research. The Fano-ADC(2,2) method is a promising candidate for this task. Owing to the inclusion of configurations with two electrons in virtual orbitals, is makes it possible to model double continua needed for the study of double Auger decay or double ICD. Benchmark calculations presented in Ref. [A1] indicate that the method is indeed capable of providing a quantitatively correct description of the relevant three-electron transitions.

3.2 Role of nuclear dynamics

Repeatedly through the thesis, we have emphasized that interatomic decay processes occur on a similar time scale as nuclear motion in atomic or molecular aggregates. Furthermore, the distance between sites actively participating in the process affect the decay rates substantially. Nuclear dynamics thus plays a prominent role in the course of the electronic transition. We have demonstrated this fact already in the preceding subsection on multi-electron processes, showing that it not only complicates the theoretical description but can actually be used to our advantage as an inner clock to extract additional information from the experiment.

In the present section, we will conclude this work by presenting a few fundamental examples in which the motion of the nuclei has a particularly pronounced effect on the observables and which are, at the same time, amenable to accurate theoretical description. These examples include ultralong-range energy transfer in a helium dimer [A9] or ETMD in the $NeKr_2$ trimer [A12]. Through the targeted population of ICD active states with considerably different lifetimes, it is possible to partially control the emitted ICD electrons' spectra [A13], which has potential for radiotherapeutic applications. Nuclear dynamics are particularly rich in water clusters or in mixtures of water and organic molecules. For instance, proton transfer along the hydrogen bond competes strongly with ICD [155]. Even though these systems are particularly interesting for the relevance of ICD and related processes in biochemistry, the field is too complex to be covered here. We refer the reader to the recent review by Jahnke and coworkers [19] and the dedicated references cited therein.

Ultralong-range energy transfer via ICD

Being possibly the most weakly bound system in nature with a binding energy of about 10^{-7} eV and a huge average bond length of about 50 Å [156, 157], helium dimer is an extreme quantum system. It is thus particularly suitable to study long-range energy transfer in an interatomic decay process. ICD can be initiated by simultaneous ionization and excitation of one of the

atoms within the dimer by a photon, which provides sufficient energy to ionize the neighbour:

$$\mathrm{He}(1s^2) - \mathrm{He}(1s^2) + h\nu \longrightarrow \mathrm{He}^{+*}(\{2s, 2p\}) - \mathrm{He}(1s^2) + e^-_{ph} \\ \longrightarrow \mathrm{He}^+(1s^1) + \mathrm{He}^+(1s^1) + e^-_{ph} + e^-_{\mathrm{ICD}}. \quad (3.16)$$

This process, which has been experimentally realized by Havermeier *et al.* [121], proved to be one of the most remarkable interatomic decay phenomena observed.

Our thorough theoretical analysis [A9–A11] has shown that, due to the dimer's extreme quantum nature and the large spatial extent of the vibrational wave function, the energy transfer occurs over a distance up to 14 Å. Furthermore, the series of peaks observed in the KER spectrum were shown to reflect the nodal structure of the vibrational wave functions of the decaying state. The possibility to observe the fingerprints of the vibrational wave function in KER was predicted already in the pioneering work of Santra *et al.* [5] for the neon dimer, but it turned out to be an artefact of inaccurate PESs [15, 158]. The principle itself, however, was correct.

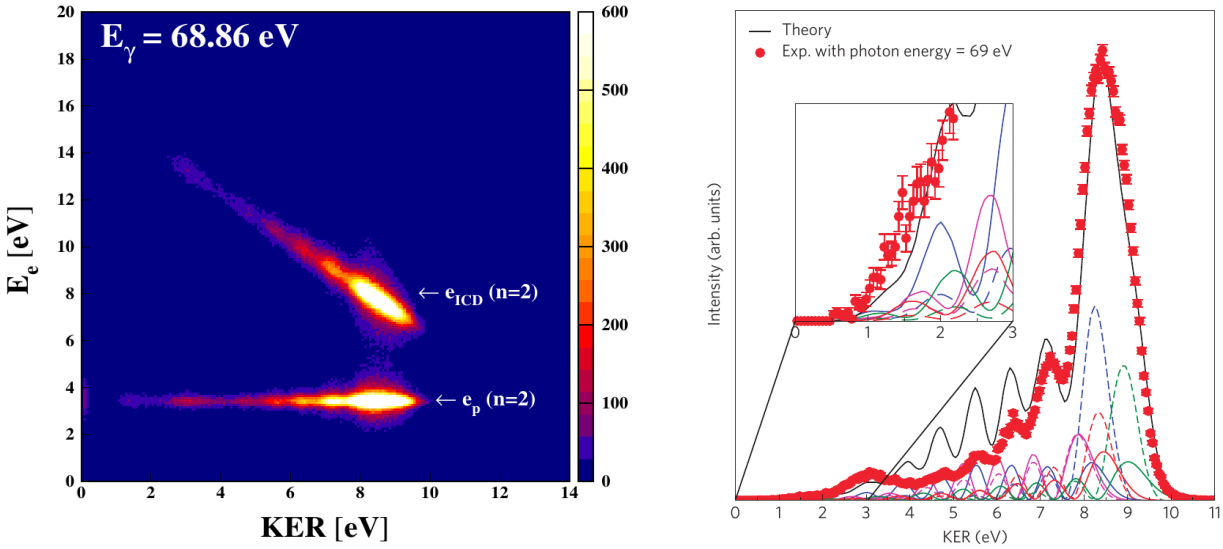

Figure 3.9: Left panel: energy of one of the two electrons from photoionization excitation of He_2 versus KER of the ionic fragments at a photon energy of 68.86 eV. **Right panel:** Experimental KER spectrum (red error bars) compared to theoretical simulation (black curve). The inset shows the low-energy tail of the spectrum, associated with the largest internuclear distances. Coloured lines show partial spectra associated with individual decaying states and decay channels. Reprinted with permission from Refs. [121] (left panel, Copyright 2010 APS) and [A9] (right panel).

Comparison of the observed and theoretical spectra is shown in Fig. 3.9 for the photon energy $E_\gamma = 68.86\,\mathrm{eV}$. In the left panel, the measured coincidence spectrum is shown as the correlation plot between the energies of individual detected electrons and KER of the two He^+ fragments. The horizontal signal corresponds to the primary photoelectron, which carries constant energy independent of the KER. The diagonal signal is the hallmark of ICD, in which

the total released energy is constant, but the sharing between the secondary electron and the ionic fragments depends on the interatomic distance at the instant of the electronic transition.

In both signals, we observe a clear modulation of intensity. In the right panel of the figure, the ICD spectrum is integrated over the electron energy to obtain pure KER spectrum $\sigma(E_{\mathrm{KER}})$, shown by red points with error bars. The modulation translates into a series of peaks which indeed correspond to the nodal structure of the vibrational wave functions associated with the $\mathrm{He}^{+*}(\{2s, 2p\}) - \mathrm{He}$ intermediate states of the dimer. Their origin is best understood via mapping KER to the internuclear distance using the reflection principle [159], as shown in the right panel of Fig. 3.10. The probability density, corresponding to the most populated vibrational wave function of the $^2\Sigma_g^+$ $2p$ metastable state, is plotted at the top. It is multiplied by R^{-6} to account for the decrease of the decay probability with increasing interatomic distance. Through the slope of the dissociative final state PES, the internuclear distance is mapped to KER, reproducing the qualitative features of the observed spectrum.

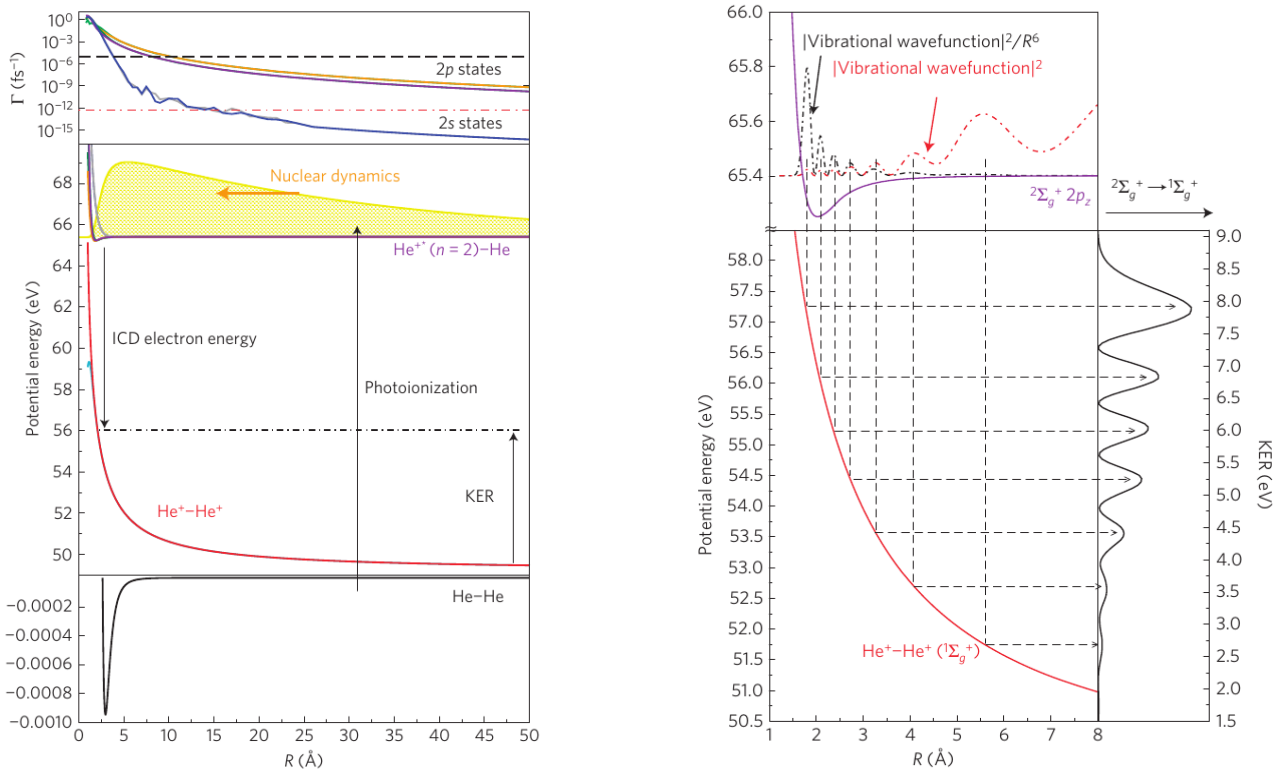

Figure 3.10: **Left panel, from top:** ICD widths, PESs of the relevant $\mathrm{He}^{+*} - \mathrm{He}$ decaying states (with the ground state nuclear wave function shown as a yellow shaded area), dissociative PECs of the $\mathrm{He}^+ - \mathrm{He}^+$ final states, and the PES of the neutral ground state. **Right panel:** Mapping between the vibrational wave function and KER via the reflection principle. Reprinted with permission from [A9].

To obtain a more accurate theoretical description, we have employed the methodology described in Sec. 1.5, taking into account all six decaying states in four different symmetries that are relevant for the given photon energy. These comprise $^2\Sigma_g^+$ $(2p, 2s)$, $^2\Sigma_u^+$ $(2p, 2s)$, $^2\Pi_g$ $(2p)$, and $^2\Pi_u$ $(2p)$ states (labeled by the symmetry and the asymptotic atomic state of the excited

$He^{+*}(n = 2)$). Relevant PESs are depicted in the left panel of Fig. 3.10. The $2p$ and $2s$ states show qualitatively different behaviour. The PESs corresponding to the $2p$ states exhibit minima around 2 Å and support eight bound vibrational states each, with mean interatomic distances covering the range of 2-27 Å. PESs of the $2s$ states have very shallow minima around 5 Å, which can support only two bound vibrational states.

Even more important is the different behaviour of the respective decay widths, shown at the top of the plot. For the $2p$ states, the $2p \to 1s$ recombination is dipole-allowed, and we observe the characteristic R^{-6} dependence on the internuclear distance. $2s \to 1s$ recombination, on the other hand, is forbidden, and ICD can proceed only via the electron transfer mechanism. This is reflected by the exponential decrease of the respective decay width at small distances. It is overridden by R^{-8} dependence for larger separations, which can be traced to a higher-order decay pathway [A10]. The different character of the atomic recombination transitions is also reflected in the radiative lifetimes of about 100 ps and 2 ms for the $He^+(2p)$ and $He^+(2s)$ states, respectively.

The resulting theoretical KER spectrum is compared to the experiment in the right panel of Fig. 3.9. Despite the overestimated intensity in the interval 4-7 eV, the agreement is very good.[3] Besides the confirmation that the KER spectrum modulation is connected with the nodal structure of the vibrational wave function, another remarkable result of the theoretical analysis is the distance over which the two atoms exchange energy. The smallest significant KER observed is about 1 eV (see inset in the right panel of Fig. 3.9), which corresponds to an interatomic separation around 14 Å, more than 45 times the atomic radius [A9]. Observability of ICD at even larger distances is prevented by radiative decay, which for $R > 10$ Å becomes the dominant relaxation channel.

In Ref. [A11], we have also demonstrated how, by measuring the time evolution of the KER spectrum, it is possible to follow in time the nuclear wave packet. Trinter and coworkers indeed carried out such an experiment [122]. Using the method of streaking of photoelectrons based on the post-collision interaction (PCI) between the photo- and ICD electrons, they investigated the temporal evolution of the KER spectrum and clearly demonstrated the principle. Furthermore, they confirmed that the nuclear motion, combined with a strong dependence of the decay widths on the internuclear distance, leads to a non-exponential character of the decay process. Shortly after excitation, the decay rates are low since the average internuclear distance is large. As the dimer contracts, the rate temporarily increases. At still later times, the decay slows down again as the short-range part of the wave packet has decayed and the process is concluded in its long-range tail. Helium dimer can thus serve as a prototype demonstrating many of the characteristic features of ICD in small systems.

[3] Non-adiabatic couplings between the $2p$ and $2s$ states of the same symmetries are taken into account and lead to an overall increase of the ICD intensity without changing the shape. The most obvious potential source of the discrepancy is the *ab initio* decay width, but the spectrum turns out to be rather insensitive to this quantity and scaling $\Gamma(R)$ does not lead to any considerable improvement [A11].

ICD driven by nuclear motion

Even stronger impact of the nuclear motion on the decay rate is expected for electron transfer driven processes, such as ETMD or exchange ICD. In the exchange ICD, the usually dominant energy transfer pathway is forbidden for symmetry reasons. A natural example would be the interatomic decay of the $2s$ states of He_2 discussed in the preceding section, but there, the exchange character is disrupted by the non-adiabatic coupling with the $2p$ states of the same symmetry. Purely exchange ICD was observed in neon dimers by Jahnke *et al.* [160] in the decay of shake-up states of odd parity, created by photoemission of a $2s$ electron with simultaneous excitation of another $2p$ electron.

The decay widths associated with electron transfer processes reflect the orbital overlap between the neighbouring atoms and decrease exponentially with increasing interatomic distance. Furthermore, due to the longer characteristic times compared to ICD, the impact of nuclear dynamics is further accentuated. The decay occurs dominantly at the shortest possible distances, i.e., at the inner turning points of the vibrational motion or the thresholds defined by crossings of the decaying and final states PESs. Coincidence spectra are thus characterized by higher KER and very low energy of the secondary electrons [160,161]. We have investigated the electron transfer-driven process on the example of ETMD in the $NeKr_2$ trimer [A12]. In this system, ETMD represents an efficient relaxation mechanism of dicationic $Ne^{2+}(2p^{-2}\,{}^1D, {}^1S)Kr_2$ states populated by the Auger decay, induced by the core ionization of Ne. The dominant process is ETMD(3), in which one Kr atom donates an electron to Ne and the other Kr atom is ionized. The whole cascade can be thus summarized as

$$\begin{aligned} Ne^+(1s^{-1})Kr_2 &\longrightarrow Ne^{2+}(2p^{-2}\,{}^1D, {}^1S) + e^-_{\mathrm{AD}} \\ &\longrightarrow Ne^+(2p^{-1}) + Kr^+(4p^{-1}) + Kr^+(4p^{-1}) + e^-_{\mathrm{AD}} + e^-_{\mathrm{ETMD}}. \end{aligned} \quad (3.17)$$

Left panel of Fig. 3.11 shows PESs of the metastable $Ne^{2+}(2p^{-2}\,{}^1D)Kr_2$ state of the b_1 symmetry (C_{2v} point group) and of the repulsive ETMD final state. The r and θ coordinates correspond to the symmetric stretch and bending modes preserving the symmetry, which were taken into account. Superimposed on the metastable state PES is the classical trajectory, starting at the equilibrium geometry of the neutral cluster (point A) and following the nuclei for the first 650 fs. After the initial ionization and the nearly instantaneous Auger decay, the Ne-Kr bonds start to contract. At point B, the metastable and final states PESs cross and the ETMD process becomes forbidden between B and the inner turning point of the stretching mode. Simultaneously, the bond angle increases, lengthening the distance between the Kr atoms and decreasing the final state energy. Therefore, during the next oscillation of the stretching mode, the ETMD channels stay open until an even shorter Ne-Kr distance.

The dependence of the ETMD rate during this classical motion is shown in the lower panel on the right in Fig. 3.11. At the equilibrium geometry of the neutral cluster, the decay rate is $0.13\,\mathrm{ps}^{-1}$. At point C, the maximal rate is $11.5\,\mathrm{ps}^{-1}$, nearly two orders of magnitude higher.

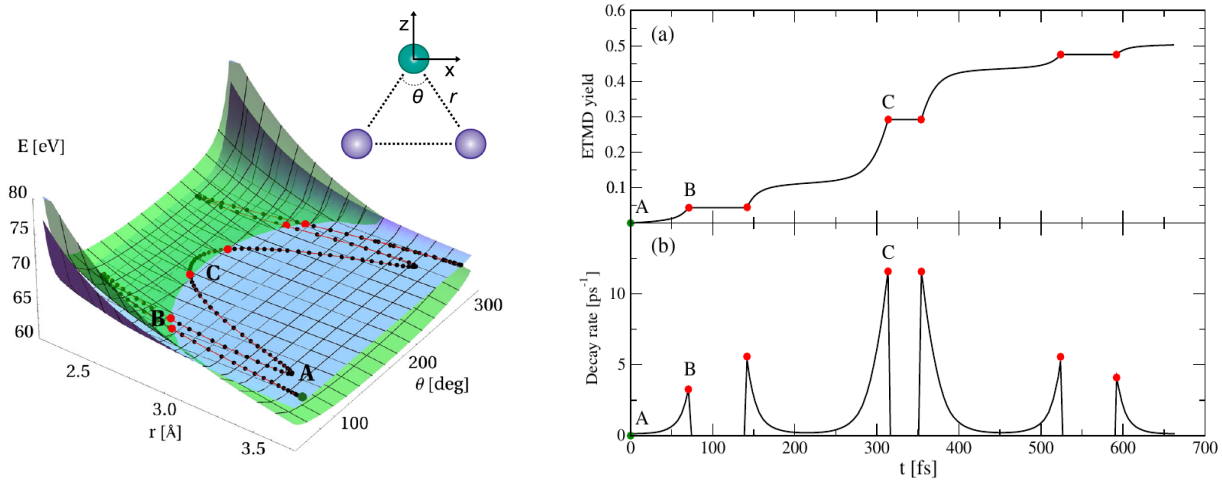

Figure 3.11: **Left panel:** Potential energy surfaces of the metastable $Ne^{2+}(2p^{-2}\,{}^1D)Kr_2$ b_1 state and of the ETMD(3) final state $Ne^+(2p^{-1})(Kr^+(4p^{-1})_2$. Red line with black dots shows the classical trajectory in the decaying state starting from the equilibrium geometry A of the neutral cluster. **Right panel:** ETMD(3) rate (bottom) and accumulation of the ETMD yield (top) along the classical trajectory shown in the left panel. Reprinted with permission from [A12] (Copyright 2013 APS).

Accumulation of the ETMD yield in time is plotted in the upper right panel of Fig. 3.11. It exhibits the intricate temporal profile of the decay process, which clearly cannot be characterized by a single lifetime. Still, since about 50% of the initial population of the metastable states has decayed during the initial 650 fs, the average decay rate is approximately $1\,\mathrm{ps}^{-1}$. The nuclear dynamics initiated by double ionization of the Ne atom thus leads to an almost tenfold increase of the effective decay rate compared to the equilibrium geometry [A12].

We have seen that the repulsive character of the multiply ionized decay channels can make the process energetically inaccessible for compact geometries. The same phenomenon occurs already in the inner-valence ionized neon dimer, see Fig. 1.4, but due to the short lifetime, it does not significantly disrupt the exponential character of the decay. However, in other systems, ICD can be energetically closed even at the equilibrium geometry. The excited state can then only decay nonradiatively when the bond length is stretched during the vibrations. In such systems, the electronic transition can be regarded as driven by nuclear motion.

For the inner-valence ionized neon, such a scenario occurs if the neighbouring atom is helium instead of another neon. Due to the significantly higher ionization potential of He, ICD of the $Ne^+(2s^{-1})$He metastable state is only possible if the bond stretches up to 6.2 Å, which is more than twice the equilibrium distance of the neutral NeHe of about 3.0 Å [137]. For a higher-lying metastable states above the $Ne^+(2s^{-1})$ threshold, ICD channels naturally open at gradually shorter interatomic distance with increasing excitation energy.

Relevant PESs are shown in the left panel of Fig. 3.12. At the bottom, the ground state PES of the neutral dimer is shown together with the probability density associated with the ground vibrational state (yellow). In the middle, PESs of the three lowest manifolds of metastable states are plotted in full lines. Individual manifolds are defined in the limit of large separations by

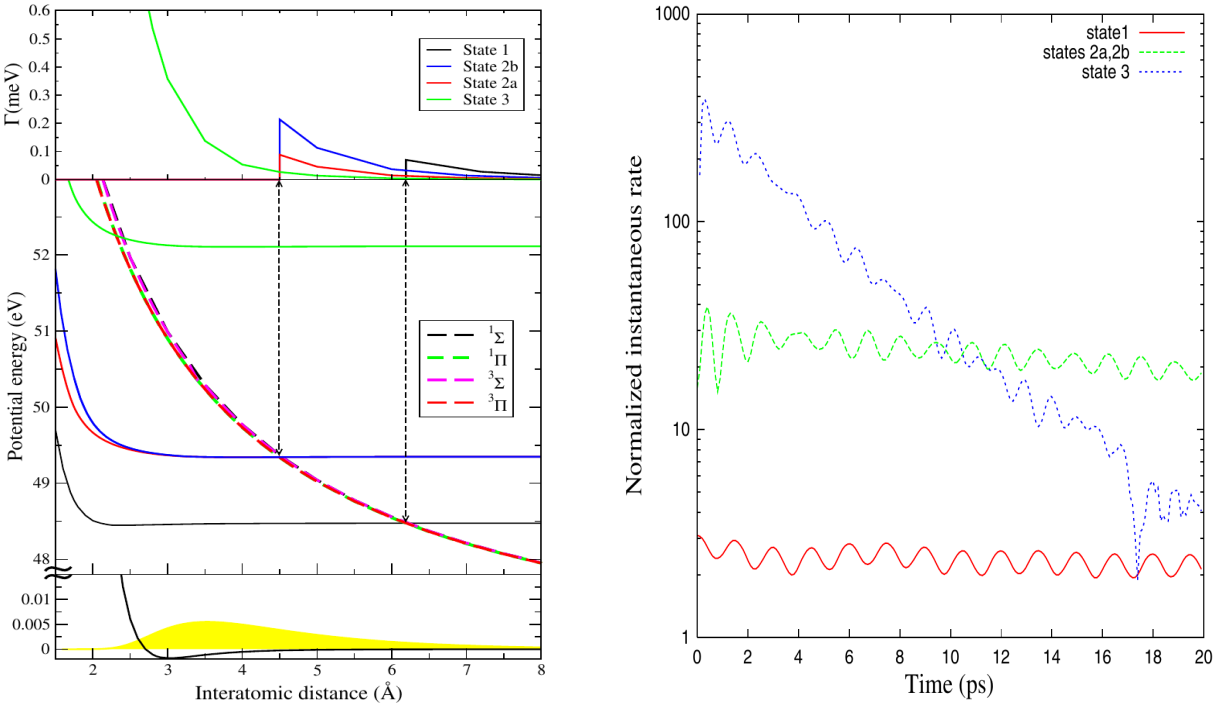

Figure 3.12: **Left panel:** Potential energy surfaces of the electronic states relevant for ICD in the NeHe dimer and the corresponding decay widths. **Right panel:** Instantaneous total decay rate, normalized to the radiative decay rate, as a function of time. Reprinted with permission from [137] (Copyright 2010 APS).

atomic states of the excited Ne, namely $Ne^+(2s^{-1})$ (state 1), $Ne^+(2p^{-2}3s\ ^2P)$ (states $2a$ and $2b$), and $Ne^+(2p^{-2}3s\ ^2D)$ (state 3). Repulsive dashed lines correspond to the $Ne^+(2p^{-1}) - He^+(1s^{-1})$ ICD final states. ICD opens at 6.2 Å for state 1, at 4.5 Å for states 2, and around 2.5 Å for state 3, which is reflected by the total ICD widths being zero below these thresholds (top panel of the plot). It is important to note that even at geometries where the ICD channels are closed, all the excited states can still decay radiatively with a lifetime of approximately 170 ps (the corresponding decay width is 3.8 μeV).

For the present discussion, the most interesting is the lowest excited state 1. Broadband photoionization induces sudden transition of the ground state vibrational wave packet onto the excited state's PES. Only a tiny fraction of the probability distribution is found at interatomic distances where ICD is open. Furthermore, the PES is attractive, and the bond starts to contract. However, since also higher vibrational levels of state 1 are excited, the wave packet periodically returns to the region where ICD is open. The period of these oscillations is around 1.5 ps. The total (ICD plus radiative) decay rate directly reflects the these oscillation, as shown in the right panel of Fig. 3.12. The ratio of the total and radiative decay rates oscillates between 2 and 3, showing that even at the distance of 6.2 Å, the returning tail of the probability distribution is enough to produce a significant ICD yield. The corresponding signal in the coincidence spectrum, characterized by a very low KER and nearly zero-energy of the secondary electron, was indeed detected in experiment [137]. Again, following the ICD process in time

would reveal direct information about the vibrational motion of the dimer in the excited state. For the other two manifolds of excited states shown in the figure, the impact of the nuclear dynamics is less significant. The instantaneous rates are also modulated by the vibrational motion, but ICD is always open and dominates over the radiative decay.

Site- and energy-selective production of slow electrons

The significance of the nuclear dynamics accompanying the decay process is strongly system dependent. At one extreme, the electronic transition is faster than the nuclear motion and the decay occurs dominantly at the equilibrium geometry of the neutral system. This results into a single peak in both the KER and secondary electron spectra, with its width determined essentially by the span of the ground state vibrational wave packet and the slope of the final states PESs. At the other extreme, the electronic transition is slow and the vibrations set in. The PESs of the ICD active states are typically more attractive[4] than those of the neutral ground state, the nuclear wave packet thus explores shorter interatomic distances. Combined with the increasing efficiency of the decay with decreasing bond lengths, the electronic transition occurs predominantly at the shortest possible distances, i.e., at the inner turning points or at thresholds if the decay channels close at some geometry. We have seen that this type of behavior is particularly pronounced for ETMD. The decay spectra are characterized by a broader, more structured KER signal, shifted to higher energies.

Interestingly, both the slow and fast ICD can be induced in a single system and exploited to exercise certain control over the energy of the secondary electrons as well as over the location of their production. We have proposed the principle in Ref. [A13]. It was then studied in detail in several theoretical [A14] [163] and experimental [164–167] works. In particular, we have analyzed ICD from the ionization shake-up satellite states in argon dimer,

$$\mathrm{Ar}^{+*}(3p^{-2}nl)\mathrm{Ar} \longrightarrow \mathrm{Ar}^{+}(3p^{-1}) + \mathrm{Ar}^{+}(3p^{-1}) + e^{-}. \tag{3.18}$$

These states can be efficiently populated by electron impact [167] or, indirectly, via resonant Auger decay (RAD) following the core $2p \rightarrow nl$ excitation of the Ar atom [A14]. RAD is usually strongly dominated by the so-called spectator decay, in which the core vacancy is filled by a valence electron and another valence electron is ejected into the continuum. The initially excited electron in the Rydberg orbital does not actively participate, but can move to another virtual orbital due to the shake-up mechanism [168]. The system is thus left in one of the ionization satellite states, and their population can be to some extent controlled by targeting different initial core-excited resonances. Decay into the cationic ground state via the participator RAD, in which the excited electron is directly emitted into continuum, is usually much less efficient [A13].

[4] This is true particularly for one-site ionized van der Waals clusters. In other situations, the metastable states themselves might be dissociative. An important example are excited molecular ions, for which the dissociation often represents strong relaxation mode competing with the electronic decay [162].

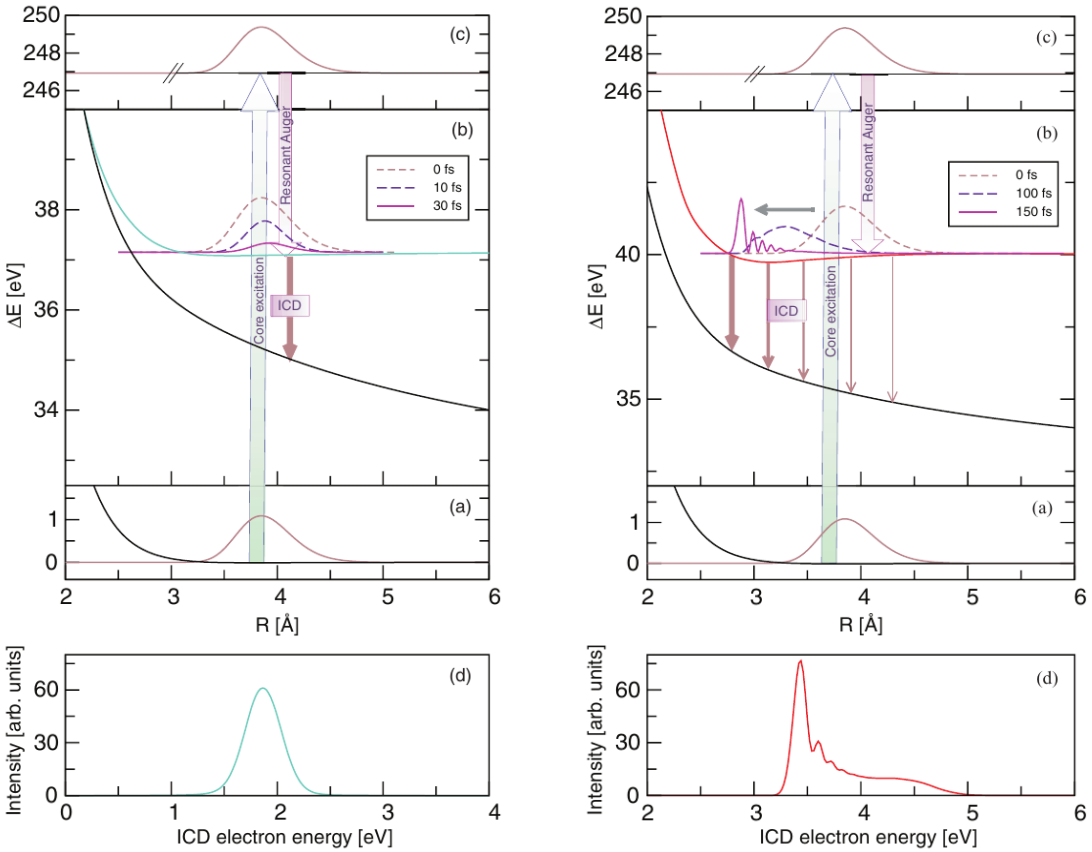

Figure 3.13: **Left panel:** PESs and time evolution of the nuclear wave packet for the cascade proceeding with a fast ICD through the $Ar^{+*}(3p^{-2}[^1D]3d\ ^2D)Ar\ ^2\Sigma_g^+$ satellite state. Resulting unstructured ICD electron spectrum is plotted at the bottom. **Right panel:** PESs and time evolution of the nuclear wave packet for the cascade proceeding with a slow ICD through the $Ar^{+*}(3p^{-2}[^1D]5s\ ^2D)Ar\ ^2\Sigma_g^+$ satellite state. The interplay between nuclear dynamics and electronic transition results in a broad ICD electron spectrum shown at the bottom, with dominant peak at the low energy side corresponding to the decay near the inner turning point of the intermediate state's PES. Reprinted with permission from [A14] (Copyright 2014 AIP Publishing).

For the low lying ionization satellites in argon dimer, characterized by the electron excited into the $4s$ or $3d$ orbital and excitation energy up to about 38 eV, ICD is fast (the computed lifetimes vary from 28 fs to 130 fs) and occurs predominantly at the equilibrium interatomic distance of 3.8 Å without any significant nuclear motion. A representative example is shown in the left panel of Fig. 3.13, which depicts the whole RAD-ICD cascade[5] proceeding via the $Ar^{+*}(3p^{-2}[^1D]3d\ ^2D)Ar\ ^2\Sigma_g^+$ satellite state. The bottom plot shows the expected single peak ICD electron spectrum.

For higher lying satellite states with the electron excited into $5s$ or $4d$, the temporal characteristics of the nuclear motion and ICD are the opposite. Due to the weaker repulsion between the electron excited into a more diffuse Rydberg orbital and the neutral Ar atom, the respec-

[5]The lifetimes of the core excited states of Ar are approximately 6 fs [169], the Auger step can thus be considered instantaneous in the simulations.

tive PESs have deeper minima shifted to shorter interatomic distances and the vibrational periods lie in the range from 180 fs to 250 fs. In contrast, the ICD lifetimes computed for the equilibrium geometry are longer, between 0.6 ps and 6.6 ps. The drop of the ICD rates with increasing principal quantum number n is also connected with the more diffuse character of the higher Rydberg orbitals, resulting in a weaker correlation with the other bound electrons. As shown in the right panel of Fig. 3.13, the decay time is long enough for the wave packet to move towards the left turning point and acquire characteristic multi-nodal structure with a dominant maximum located close to the left turning point [A14]. It is fully reflected in the ICD electron spectrum shown at the bottom of the plot, reminiscent of the mirror image of the KER spectrum measured in the helium dimer.

In the experiment carried out by Ren and coworkers [167], ICD was initiated directly by electron-impact ionization with the projectile energy $E_0 = 90$ eV. This excitation mechanism offers little control over the population of different satellite states. Still, by measuring the projectile energy loss spectra and the correlation between KER and ICD electron energy, it is possible to extract the energies and populations of the intermediate ICD-active states *a posteriori*. The measured KER spectrum shows the expected double-peak character – states decaying at the equilibrium geometry contribute to the lower peak around 3.8 eV while the broader peak at about 5.2 eV corresponds to the decay at the shorter interatomic distances. Fast- and slow-decaying states can thus be separated by filtering the low and high KER signal, respectively. Fast ICD is indeed observed for the lower-lying satellites with excitation energy up to 38.8 eV, while the higher lying states decay more slowly as predicted by the theory.

These results indicate that, through the dependence of the ICD electron spectra on the character of the metastable ionization satellite states, the RAD– ICD cascade offers certain control over the energy of the produced slow secondary electrons. Indeed, exploiting the resonant character of the initial photoexcitation, it is possible to selectively populate specific core-excited state by using monochromatic soft X-ray radiation tuned to the chosen resonance. In turn, the Auger decay of different parent core excited states populates predominantly different groups of ICD active ionization satellites. Studies of the RAD – ICD cascade in other ArX rare gas dimers (X = Ne,Kr,Xe) [163–166] confirm this control mechanism and show that it is not system specific.

Even more beneficial, however, might be the control this cascade process offers over the location of the emission of the slow ICD electrons. In a heteroatomic system, radiation tuned to a specific resonance in a specific element will populate the targeted core-excited states with a high probability, as the corresponding cross sections are much larger than those of non-resonant ionization or excitation. Due to the chemical shifts of the atomic levels in different chemical environments, it is even possible to select among chemically identical atoms occupying non-equivalent sites in the system. Because of the local character of RAD, the ICD-active ionization satellites are predominantly populated on the initially excited atom. In turn, ICD ionizes the environment in the vicinity of the parent core excitation.

The site selectivity of the resonant core excitation and the sensitivity of the ICD electron spectra to the closest neighbours offer interesting possibilities of turning the RAD-ICD cascade into a unique spectroscopic tool, probing both to the intramolecular electronic structure (RAD) and the local environment (ICD). Another potential application opens in the context of radiation biology and cancer radiotherapy. Ordinary radiotherapy employs broadband radiation to destroy cancerous cells with extensive side effects. Some approaches tag the cancerous cells with molecular markers containing high atomic number elements as emitters for targeted production of genotoxic secondary electrons [170]. Combination with the highly selective resonant excitation would help to localize the deposition of the radiation energy and thus minimize the overall radiation dose [162]. The energy-selectivity of the RAD-ICD cascade could help to further increase the efficiency by tuning the energies of the slow secondary electrons to induce the more lethal double strand breaks in the DNA of the cancerous cells [A13].

Extracting R-dependent absolute decay widths from the experiment

One of the central topics of this thesis is the theoretical determination of decay widths for ICD and related electronic processes. It is thus natural to ask whether the presented results can be verified by the experiment. We have postponed this question until after the discussion of nuclear dynamics, which, as we have seen, are inseparable from the electronic transition and can in fact serve as an inner clock for studying the evolution of the system. Since the decay width is not a directly measurable quantity, the opportunities to test the theory are sparse. In a pump-probe experiment conducted by Schnorr and coworkers [6], the lifetime of the $2s$ inner-valence vacancy in the neon dimer was estimated as 150 ± 50 fs, which is in reasonable agreement with the most recent theoretical value of 220 fs, computed by the Fano-ADC(2,2) method [A1]. The above mentioned PCI-based experiment of Trinter *at al.* [122] confirmed the predicted non-exponential decay of ionized-excited states in helium dimer. Quantitatively, experiment suggests significantly faster decay than the theory, but the comparison is inconclusive because of the large experimental error margins.

The ICD lifetime can also be inferred from the experiment indirectly through simulation of the nuclear dynamics using *ab initio* PESs and decay widths, combined with scaling of the decay width magnitude to obtain the best possible agreement between the measured and simulated KER spectra. We have used this approach to verify the predicted short CAD lifetime in the CH_3F molecule, as reported in Sec. 3.1. Ouchi *at al.* [171] used the same principle to estimate the rate of ICD after Auger decay of the Ne $1s$ vacancy in NeAr dimer and concluded that the actual ICD rate is roughly two times lower than predicted by *ab initio* calculations; their findings thus go in the opposite direction than those of Trinter and coworkers. In general, the agreement between theory and experiment is only semi-quantitative at best.

In 2017, Rist and coworkers [A15] went even further and attempted to extract the absolute R-dependent decay widths from the measured KER spectrum, using only the *ab initio* PESs

as an additional input. In the experiment, the argon dimers were irradiated by photons of energy $h\nu = 51\,\mathrm{eV}$, populating a number of ICD-active ionization satellite states of the type $\mathrm{Ar}^{+*}(3p^{-2}nl) - \mathrm{Ar}$. Photoelectrons, ICD electrons, and dissociating Ar^+ cations were detected in coincidence using the COLTRIMS apparatus. Several ICD signals are clearly discernible in the correlation plot between the secondary electron energy and KER (see Fig. 1 in [A15]), which can be assigned to different metastable states. Among these, the signal associated with the $3p^{-2}[^1D]4d\ ^2S$ satellite state was selected for further analysis because it appears to be energetically well isolated. It makes it possible to reliably separate the respective KER distribution and perform an inversion procedure to extract absolute ICD rate as a function of internuclear distance.

The inversion procedure is described in detail in Ref. [A15]. In short, a one-dimensional histogram of internuclear distances R is created and initialized with N test particles according to the shape of the vibrational wave function of the Ar_2 ground state. The number N corresponds to the total number of experimentally observed ICD events associated with the given metastable satellite state. Then, the evolution of the ensemble is simulated, assuming classical motion of the particles on the *ab initio* PES of the decaying state. The "local" ICD rate is determined by comparison of the actual number of decays observed at the given geometry[6] to their residence time in the given histogram bin, i.e., to the time needed for the particles to move to the neighbouring bin. Subsequently, the soundness of the procedure is verified by performing a fully quantum-mechanical simulation of the nuclear dynamics with the extracted geometry-dependent decay width Γ_{exp}.

The measured KER signal, shown in blue in the left panel of Fig. 3.14, has the characteristic double-peak structure. The lower KER maximum around 3.7 eV corresponds to the electronic transition taking place near the equilibrium geometry of the neutral cluster ($R_{\mathrm{eq}} = 3.8\,\mathrm{eV}$ [172]), while the higher-KER peak to the decay near the inner turning point of the intermediate state PES. The black curve shows the KER spectrum obtained by the fully quantum-mechanical simulation using the decay width Γ_{exp}, plotted by black points in the right panel of the Fig. 3.14. The agreement with the measured KER is good and justifies the inversion procedure based on the classical dynamics.

The *ab initio* decay width computed using the Fano-ADC(2)x method (Γ_{theory}) is shown in the right panel of Fig. 3.14 in blue. There is fundamental disagreement, both quantitative and qualitative, between Γ_{theory} and Γ_{exp}. At the equilibrium distance, Γ_{theory} is about four times larger than Γ_{exp}. Furthermore, the former behaves according to the R^{-6} rule while the latter is flatter between 4.0 Å and 3.5 Å and then increases much faster below 3.0 Å.[7] Consequently, the KER computed using the *ab initio* width (shown in red in the left panel of the figure) posses

[6] The mapping between interatomic distance and KER is obtained using the reflection approximation as $R = 1/\mathrm{KER}$, see also Fig. 3.10. Purely Coulombic character of the PESs of the $\mathrm{Ar}^+ + \mathrm{Ar}^+$ final states is assumed.

[7] The increase of Γ_{Exp} for $R > 4$ Å is likely a nonphysical artefact of the numerical procedure but is of little consequence as only a small tail of the wave packet explores this region.

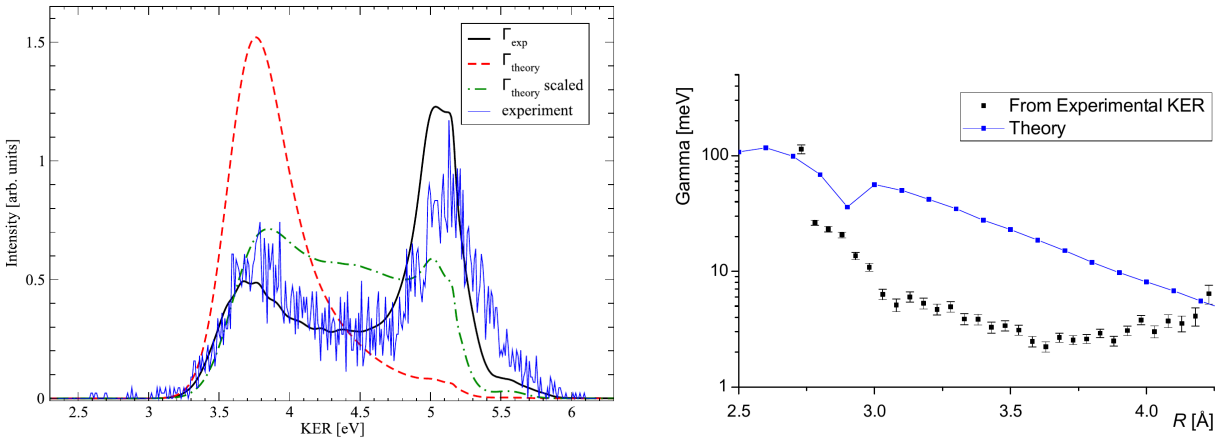

Figure 3.14: **Left panel:** Comparison between experimental and computed KER spectra produced in ICD of the $3p^{-2}[^1D]4d\ ^2S$ satellite state in Ar_2. The spectra were computed using the decay width Γ_{exp} extracted from the experiment (black solid), theoretical decay width Γ_{theory} (dashed red), and Γ_{theory} scaled such that it is equal to the value of Γ_{exp} at the equilibrium interatomic distance $R = 3.8\,\text{Å}$ (dashed-dotted green). All spectra are scaled such that their area is equal to 1. **Right panel:** The decay width Γ_{exp} extracted from the measured KER (black squares) and the *ab initio* width Γ_{theory}, computed with the Fano-ADC(2)x method. Reprinted with permission from Ref. [A15] (Copyright 2017 Elsevier).

essentially only the 3.7 eV maximum as the fast decay precludes any significant nuclear motion. Even when the theoretical width is scaled down by the factor of four to match the magnitude of Γ_{exp} at the equilibrium distance, the high-energy KER maximum stays too weak due to the missing steep rise of Γ_{theory} below 3 Å (green curve in the plot). Such a profound discrepancy casts serious doubts on the methodology presented in this work and needs to be resolved.

An obvious source of error is the ADC(2)x scheme used to represent the metastable state and evaluate the decay widths. At this level, the ionization satellites are described through the first order of PT only, which is likely insufficient to reproduce the wave function, particularly the spatial extent of the $4d$ orbital. On the experimental side, it is critical to realize that the extraction of the decay width rests on the theoretical PES associated with the metastable state. For high-lying satellites embedded in a continuum, it is extremely difficult to identify the corresponding eigenvalues in the high-level *ab initio* calculations. Therefore, the PES of the $Ar^{+*}(3p^{-2}[^1D]4d\ ^2S) - Ar$ state was approximated by the average of the PESs of the parent $Ar^{2+}(3p^{-2}[^1D]) - Ar$ dicationic states, computed using multi-reference CI singles and doubles [A14]. This seems justified as the inversion procedure is rather insensitive to the details of the PES and small variations in the position and width of the initial distribution of test particles [A15]. However, we will argue that the assumed physical picture of the $3p^{-2}[^1D]4d\ ^2S$ state being energetically isolated is incorrect in the dimer and that non-adiabatic effects play a critical role.

The recently developed Fano-ADC(2,2) method describes the ionization satellite states at the second-order of PT, and it is thus natural to reassess the theoretical interpretation of the experiment using the improved toolbox. Furthermore, the Fano-Feshbach approach, namely the

projection of the bound- ($\mathcal{Q}$) and continuum-like ($\mathcal{P}$) subspaces, makes it possible to reliably identify individual satellite states within the sparse spectrum of the $\mathcal{Q}$ subspace.[8] As such, together with the ADC(2)x scheme for the doubly ionized final states [89], the method can provide a fully *ab initio* model consistent through the second-order of PT. Here, we present the first attempt to construct such a model and reinterpret the measurement. Our objective is not yet to provide a definitive answer but rather to demonstrate the insufficiency of the original model and stimulate further study of the role of non-adiabatic effects in ICD.

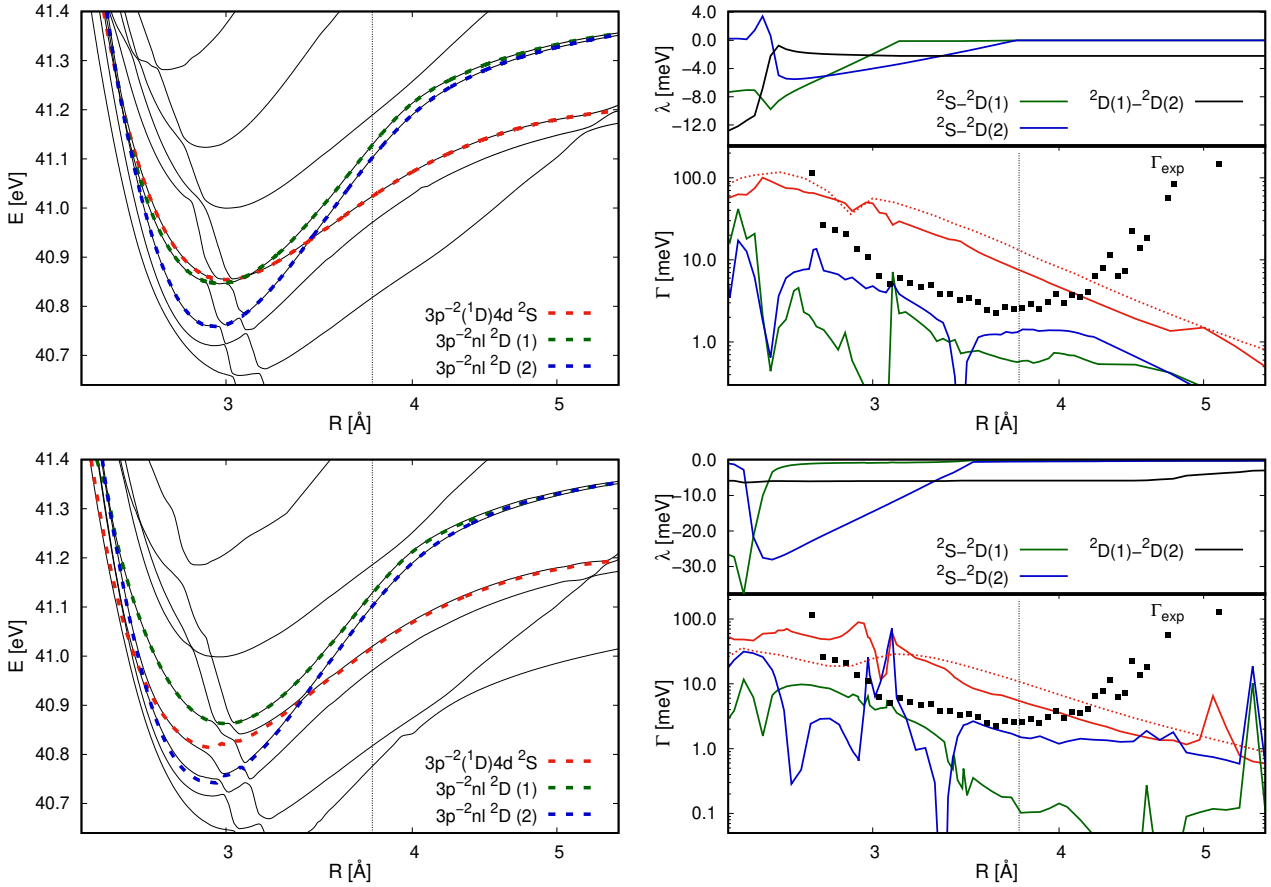

Figure 3.15: *Ab initio* model of ICD from $Ar^{+*}(3p^{-2}[^1D]4d\ ^2S)$ – Ar satellite state, computed using the Fano-ADC(2,2) method. Upper and bottom panels show the $^2\Sigma_g^+$ and $^2\Sigma_u^+$ total $D_{\infty h}$ symmetries, respectively. **Left panels:** Potential energy curves of the adiabatic states (solid black lines) found in the spectral region of interest, and the diabatic states (coloured dashed lines) included in the model. **Right panels:** (bottom) Decay widths of the diabatic states (solid lines), in the same colour coding as in the left panels. Thin dotted line and black points show, respectively, the original Fano-ADC(2)x width Γ_{theory} and Γ_{exp} from Fig. 3.14. (top) Non-adiabatic couplings between the three diabatic states shown in the left panels.

[8] In particular, the state of interest is easily distinguished by an appreciable admixture of the $3s^{-1}\ 1h$ configuration owing to its total ^2S symmetry. This feature also helps to identify other states with which it can significantly interact.

The results of the Fano-ADC(2,2) calculations[9] are summarized in Fig. 3.15; the upper and bottom panels correspond the $^2\Sigma_g^+$ and $^2\Sigma_u^+$ total $D_{\infty h}$ symmetries, respectively. In the left plots, black lines denote adiabatic metastable states (eigenstates of the projected QHQ Hamiltonian) found in the energy region of interest. The diabatic PES corresponding to the $3p^{-2}[^1D]4d\ ^2S$ state is plotted by the red dashed line. While at the equilibrium distance, indicated by the vertical dotted line, it might be considered isolated, between 3.4 Å and 3.1 Å it interacts with two states (shown by blue and green dashed lines) belonging to a multiplet correlating with an $\mathrm{Ar}(3p^{-2}nl\ ^2D)$ atomic term in the asymptotic region. All the states cross again around 2.5 Å. Furthermore, still more states come into play below 3.1 Å.

To find the exact non-adiabatic coupling elements (1.78) and construct a complete diabatic representation of the manifold of states shown in Fig. 3.15 would be a challenging task that goes beyond our present purpose and capabilities. Here, we merely want to demonstrate that such a picture can indeed explain the measured KER spectrum and that the rather unexpected shape of Γ_{exp} is likely a result of the description of complicated non-adiabatic dynamics using a simple single-state model. To this end, we reduce the new model to the three diabatic states shown by the coloured PESs in the figure. The non-adiabatic couplings $\lambda(R)$ between them are estimated using the simple approach used by Pahl *et al.* [66]. The point of the crossing of two diabatic states is determined as the geometry of the minimal energy distance of the corresponding adiabatic PESs. Since the diabatic and adiabatic representations are connected by a unitary transformation,

$$\boldsymbol{H}_{el}^{dia}(R) = \begin{pmatrix} U_1^{dia}(R) & \lambda(R) \\ \lambda(R) & U_2^{dia}(R) \end{pmatrix} = \boldsymbol{S}(R) \begin{pmatrix} U_1^{ad}(R) & 0 \\ 0 & U_2^{ad}(R) \end{pmatrix} \boldsymbol{S}^\dagger(R) \tag{3.19}$$

the requirement of the diabatic states to cross at the chosen geometry R_0 unambiguously determines the value of the coupling $\lambda(R_0)$ at this point. Assuming that the coupling is constant in turn fully determines the unitary transformation at other geometries.

In the present case, we have generalized the approach in two ways. Since some of the considered states cross at two internuclear distances, we have assumed linear dependence of the couplings to provide the necessary flexibility. Furthermore, since three adiabatic states are involved, the diabatization procedure was performed iteratively, and the final geometry-dependent transformation $\boldsymbol{S}_{tot}(R)$ was obtained by multiplication of the individual transformation matrices $\boldsymbol{S}(R)$. Any possible interaction with the other adiabatic states shown in Fig. 3.15 was ignored. Finally, the diabatic decay widths and the *via the continuum* couplings were computed from

[9]The calculations were carried out using an effective core potential with $4s$, $4p$, $4d$ and $1f$ basis functions for the 8 active valence electrons [173], as included in the MOLCAS [174] basis set library. The basis was further augmented by $6s$, $6p$ and $11d$ Rydberg-like diffuse functions [175] on each atom. After the SCF procedure, only the virtual orbitals with energy below 105 eV were included in the ADC(2,2) calculations to reduce computational costs. The basis is thus smaller than that used with the ADC(2)x in Ref. [A14]. Still, the convergence of the PES and the decay width of the $3p^{-2}[^1D]4d\ ^2S$ resonance was reached due to the much larger space of ISs.

the transformed discrete state-continuum couplings [66]

$$\boldsymbol{W}^{dia}(R) = \boldsymbol{S}_{tot}(R)\boldsymbol{W}^{ad}(R), \tag{3.20}$$

where $W_k^{ad}(R) = \sqrt{\Gamma_k^{ad}(R)/2\pi}$ and $\Gamma_k^{ad}(R)$ is the width determined for the adiabatic resonance by the Fano-ADC(2,2) method.

The resulting decay widths are shown in the right panels of Fig. 3.15 in a colour coding matching the PESs in the left panels. The jagged character of the blue and green lines results primarily from the imperfect diabatic transformation and neglecting other states. Notably, for the $3p^{-2}[^1D]\,4d\ ^2S$ diabatic state, the ADC(2,2) scheme predicts qualitatively the same decay width as the original ADC(2)x calculation, only by a factor 1.7 smaller. Therefore, around the equilibrium geometry, the new *ab initio* decay width is still by a factor of 2.5 larger than Γ_{exp}. In the multi-state picture, the latter is to be interpreted as an effective decay width, and its shape thus reflects also the population of the slowly decaying states from the ^2D manifold, as well as the strength of the non-adiabatic couplings.

The plausibility of the new multi-state model is confirmed by the KER spectrum calculated using Eqs. (1.96) and (1.99). The complete model consists of the neutral ground state PES [176], for each symmetry the three PESs of the diabatic states with the corresponding decay widths and non-adiabatic couplings as shown in Fig. 3.15, and the 18 PESs of the dicationic $\text{Ar}^+(3p^{-1}) - \text{Ar}^+(3p^{-1})$ final states. The latter are computed using the ADC(2)x scheme for double ionization [89] with the same basis set as used for the discrete states manifold. Equal population of all the final states is assumed. PESs of the whole discrete states manifold were shifted by 0.611 eV to match the reference atomic ionization potential of the $3p^{-2}[^1D]4d\ ^2S$ satellite state [177] at asymptotic distances. Similarly, the final states manifold was shifted by 0.928 eV.

Comparison of the measured and calculated KER spectra is shown in Fig. 3.16. In the calculations, we assume that only the $3p^{-2}[^1D]4d\ ^2S$ states are directly populated, with equal intensity assigned to the gerade and ungerade symmetries. No photoelectron signal is visible in the experiment [178] that could be associated with the ^2D multiplet, suggesting very low photoionization cross-section. Neglecting all the couplings between the diabatic states and thus working with an effectively one-state model results into the red dashed curve, which is qualitatively very similar to the results of the original model.[10] As in the Fig. 3.14, the green dashed-dotted line shows the spectrum obtained after scaling down the *ab initio* decay width, here by a factor of 0.3 to reproduce the relative magnitudes of the two maxima. The comparison with experiment is still rather poor. Furthermore, considering the accuracy of the Fano-ADC(2,2) method demonstrated in Ref. [A1], such a scaling is difficult to justify.

Result of the full model, with both the direct (λ) and the *via the continuum* couplings fully taken into account, is shown by the black curve. We see that the higher KER peak emerges

[10] Note the different normalization of the spectra in Figs. 3.14 and 3.16 – in the former, all spectra are normalized such that their area is equal to 1, in the latter we normalized all the spectra to the same magnitude of the lower maximum.

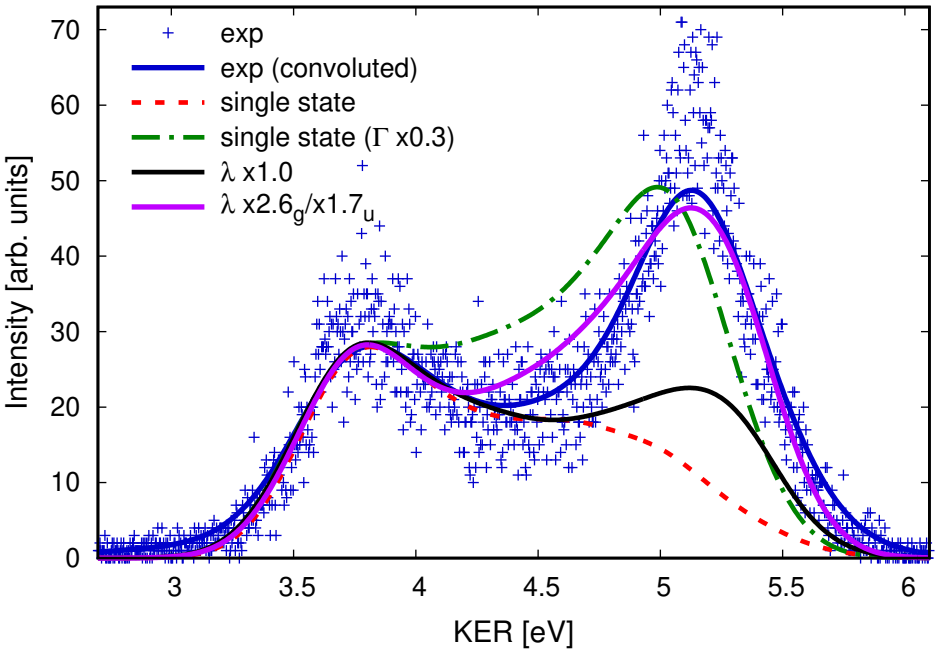

Figure 3.16: Comparison of the theoretical KER spectrum, calculated using the new Fano-ADC(2,2)-based model, with the experimental data. Red dashed curve shows KER obtained when only the $3p^{-2}[^1D]4d\ ^2S$ state is taken into account, green dashed-dotted line results from scaling of the *ab initio* decay width by a factor of 0.3. Solid black is the result of full model with non-adiabatic couplings taken into account, magenta spectrum is obtained when all non-adiabatic couplings are uniformly scaled by factors of 2.6 and 1.7 for the gerade and ungerade symmetry, respectively. The experimental KER spectrum is shown by blue points and by solid blue line after convolution with 150 meV FWHM Gaussian function. All theoretical spectra are convoluted with the same function to account for the finite experimental resolution.

but is weak compared to the measured signal. The discrepancy, however, can be corrected by a rather small adjustment. Considering the somewhat *ad hoc* approach to determine the non-adiabatic couplings, we take their magnitude as a free parameter of the model. Uniform scaling of all the direct couplings $\lambda(R)$ by a factor of 2.6 for gerade and 1.7 for ungerade symmetry then gives the KER spectrum shown by the magenta curve, in which the relative strength of the two maxima almost exactly matches that of the measured signal after convolution of both with the same 150 meV FWHM Gaussian function. The positions of the maxima and the total width of the predicted signal very accurately fit the experimental data as well. The only remaining discrepancy is the less pronounced dip between the peaks, which is mainly due to the larger decay width of the $^2D\,(2)$ ungerade state as compared to its gerade counterpart.

Clearly, the multi-state model describes the observed KER signal better than the original simple picture, and shows that the *ab initio* decay widths are compatible with the experiment. The fact that the decay dynamics of the ionization satellite states are affected by interaction with other close-lying states is not surprising. The phenomenon is known to occur in Rydberg series of autoionizing states even in atoms [48], and the density of states only increases in dimers or larger aggregates. Still, despite the excellent agreement with the experiment, the

presented results should not be overestimated as the model does not provide an absolutely conclusive picture of the process. It is important to keep in mind that the results were tweaked by adjusting the magnitude of the non-adiabatic couplings. Furthermore, the *via the continuum* couplings are estimated directly from the products of the total decay widths, which gives the upper bound for the coupling rather than the exact value. The neglected states associated with the steep PESs crossing the discrete states manifold around 3 Å (cf. Fig. 3.15) could also alter the dynamics.

Furthermore, despite the attempts to ensure convergence of the results, the substantial computational costs of the ADC(2,2) scheme and the efficiency of the available implementation of this recently developed method prevent the use of the optimal basis set. In fact, the investigated spectral region is at the limit of the capabilities of the method. The typical error of the ADC(2,2) ionization potentials is certainly larger than the energy spacing of $\sim 100\,\mathrm{meV}$ between the satellite states considered in the model. More importantly, the accuracy of relative energies of different ionization satellite states in rare gas atoms is comparable to this spacing already for the lowest states [A1], making the relative positions of different PESs found in the discrete states manifold inherently volatile. Thus, it is not possible to rule out that the appearance of the suitable multiplet interacting with the $3p^{-2}[^1D]4d\ ^2S$ resonance is coincidental. As mentioned before, this study should serve primarily as a motivation for further research of the non-adiabatic effects connected with interfering resonances. We have demonstrated that they can be found already in simple systems, amenable to both theory and experiment, and are surely abundant in nature.

Outlook

Nearly 25 years after its discovery, interatomic or intermolecular Coulombic decay is firmly established as a very general nonlocal relaxation mechanism, characteristic of relatively low-energy excited states of atoms and molecules in weakly bound aggregates. In fact, it took much less than that; already in 2011, it was *well-known that ICD appears everywhere and transfers the energy and the charge from the species with the vacancy to the environment surrounding it* [146]. Whenever an ICD channel is open, it outpaces any competing radiative and non-radiative decay modes save the local Auger-type processes. Its efficiency stems from the energy being transferred directly between electrons via the Coulomb interaction.

This thesis presented the framework for the theoretical description of ICD and related processes, and demonstrated their basic characteristics in the smallest possible systems. The focus is placed on the candidate's main contributions to the research field – the development and use of the efficient and widely applicable Fano-ADC method for the computation of the decay widths. On the one hand, its universality and capability to provide qualitative insight into the decay processes under various conditions enabled the prediction and analysis of novel mechanisms, such as the collective or superexchange ICD. Its efficiency and quantitative reliability, on the other hand, made Fano-ADC the method of choice for analysis and interpretation of experiments in several projects, carried out in collaboration with leading groups in the field. Furthermore, due to its unique ability to accurately capture the molecular orbital picture breakdown in the inner-valence ionization region, the ADC(2,2) scheme itself has many potential applications outside the realm of electronic decay, e.g., the study of electronic quantum coherence in complex molecules [179].

Although the focus of the ongoing research is naturally moving towards larger aggregates, molecules of biological relevance, or quantum dots and other nanoscale structures, there are still some fundamental questions that deserve attention. The non-adiabatic effects connected with interacting metastable states stand out very strongly. We have seen how they can alter the decay dynamics in diatomics, and with the growing size of the systems, their importance will only increase. Our latest calculations show that in the Ne_2He trimer, a considerable number of metastable states interact in the energy region of inner-valence ionization of neon, and their impact might be stronger than the superexchange mechanism.

A hitherto neglected question is the possible breakdown of the local complex potential approximation. The interatomic decay frequently occurs at the threshold, and in this regime,

the approximation is not justified. Proper treatment of the nonlocal dynamics is known to be essential for the correct description of various phenomena occurring in the resonant low-energy electron-molecule scattering [27]. It is thus natural to ask whether the nonlocality can be relevant also in the present context. In contrast to the electron-molecule collisions, however, for interatomic decay, there are no observations that would be in a manifest conflict with the local description.

Owing to the recent experimental evidence that multi-electron decay processes could be more significant in the response of matter to ionizing radiation than previously believed, the study of these phenomena appears to be more relevant. In this respect, the development of the Fano-ADC(2,2) method is timely. Due to its ability to describe states with two electrons in continuum and high accuracy of the computed decay widths, it appears to be the perfect candidate to study double Auger decay in molecules or double ICD in clusters. Since the theoretical understanding of these processes is very limited, they represent the obvious research subject for the nearest future.

List of Abbreviations

$\mathcal{L}^2$ Square-integrable functions

ADC Algebraic diagrammatic construction

CAD Collective Auger decay

CAP Complex absorbing potential

CES Correlated excited state

CI Configuration interaction

COLTRIMS Cold target recoil ion momentum spectroscopy

COR Canonical order relations

DIM Diatomics-in-molecules

ECO Excitation class orthogonalization

ETMD Electron-transfer mediated decay

GF Green's function

HF Hartree-Fock

ICD Interatomic Coulombic decay

IS Intermediate state

ISR Intermediate state representation

KER Kinetic energy release

LCP Local complex potential approximation

MO Molecular orbital

PCI Post-collision interaction

PES Potential energy surface

PT Perturbation theory

RAD Resonant Auger decay

SE-ICD Superexchange ICD

TDSE Time-dependent Schrödinger equation

TIP Triple ionization potential

TISE Time-independent Schrödinger equation

Bibliography

[1] L. Meitner. *Über den Zusammenhang zwischen β- und γ-Strahlen.* Zeit. Phys. **9**(1), 145 (1922).

[2] P. Auger. *Sur l'effet photoélectrique composé.* J. Phys. Radium **6**, 205 (1925).

[3] C. D. Wagner. *Chemical shifts of Auger lines, and the Auger parameter.* Faraday Discuss. Chem. Soc. **60**, 291 (1975).

[4] L. S. Cederbaum, J. Zobeley, and F. Tarantelli. *Giant intermolecular decay and fragmentation of clusters.* Phys. Rev. Lett. **79**(24), 4778 (1997).

[5] R. Santra, J. Zobeley, L. S. Cederbaum, and N. Moiseyev. *Interatomic Coulombic decay in van der Waals clusters and impact of nuclear motion.* Phys. Rev. Lett. **85**(21), 4490 (2000).

[6] K. Schnorr, A. Senftleben, M. Kurka, A. Rudenko, L. Foucar, G. Schmid, A. Broska, T. Pfeifer, K. Meyer, D. Anielski, R. Boll, D. Rolles, M. Kübel, M. F. Kling, Y. H. Jiang, S. Mondal, T. Tachibana, K. Ueda, T. Marchenko, M. Simon, G. Brenner, R. Treusch, S. Scheit, V. Averbukh, J. Ullrich, C. D. Schröter, and R. Moshammer. *Time-resolved measurement of interatomic Coulombic decay in Ne_2.* Phys. Rev. Lett. **111**, 093402 (2013).

[7] M. Förstel, T. Arion, and U. Hergenhahn. *Measuring the efficiency of interatomic Coulombic decay in Ne clusters.* J. El. Spect. Rel. Phenom. **191**, 16 (2013).

[8] A. Hans, C. Küstner-Wetekam, P. Schmidt, C. Ozga, X. Holzapfel, H. Otto, C. Zindel, C. Richter, L. S. Cederbaum, A. Ehresmann, U. Hergenhahn, N. V. Kryzhevoi, and A. Knie. *Core-level interatomic Coulombic decay in van der Waals clusters.* Phys. Rev. A **2**, 012022 (2020).

[9] L. Liu, P. Kolorenč, and K. Gokhberg. *Efficiency of core-level interatomic Coulombic decay in rare-gas dimers.* Phys. Rev. A **101**(3) (2020).

[10] Y. Morishita, X.-J. Liu, N. Saito, T. Lischke, M. Kato, G. Prümper, M. Oura, H. Yamaoka, Y. Tamenori, I. H. Suzuki, and K. Ueda. *Experimental evidence of interatomic Coulombic decay from the Auger final states in argon dimers.* Phys. Rev. Lett. **96**(24), 243402 (2006).

[11] D. You, H. Fukuzawa, Y. Sakakibara, T. Takanashi, Y. Ito, G. G. Maliyar, K. Motomura, K. Nagaya, T. Nishiyama, K. Asa, Y. Sato, N. Saito, M. Oura, M. Schoeffler, G. Kastirke, U. Hergenhahn, V. Stumpf, K. Gokhberg, A. I. Kuleff, L. S. Cederbaum, and K. Ueda. *Charge transfer to ground-state ions produces free electrons.* Nature Commun. **8**, 14277 (2017).

[12] V. Stumpf, K. Gokhberg, and L. S. Cederbaum. *The role of metal ions in X-ray-induced photochemistry.* Nat. Chem. **8**(3), 237 (2016).

[13] S. Marburger, O. Kugeler, U. Hergenhahn, and T. Möller. *Experimental evidence for interatomic Coulombic decay in Ne clusters.* Phys. Rev. Lett. **90**(20), 203401 (2003).

[14] R. Dörner, V. Mergel, O. Jagutzki, L. Spielberger, J. Ullrich, R. Moshammer, and H. Schmidt-Böcking. *Cold Target Recoil Ion Momentum Spectroscopy: a 'momentum microscope' to view atomic collision dynamics.* Phys. Rep. **330**(2-3), 95 (2000).

[15] T. Jahnke, A. Czasch, M. S. Schöffler, S. Schössler, A. Knapp, M. Käsz, J. Titze, C. Wimmer, K. Kreidi, R. E. Grisenti, A. Staudte, O. Jagutzki, U. Hergenhahn, H. Schmidt-Böcking, and R. Dörner. *Experimental observation of interatomic Coulombic decay in neon dimers.* Phys. Rev. Lett. **93**(16), 163401 (2004).

[16] U. Hergenhahn. *Interatomic and intermolecular Coulombic decay: The early years.* J. El. Spect. Rel. Phenom. **184**(3–6), 78 (2011).

[17] V. Averbukh, P. Demekhin, P. Kolorenč, S. Scheit, S. D. Stoychev, A. I. Kuleff, Y.-C. Chiang, K. Gokhberg, S. Kopelke, N. Sisourat, and L. S. Cederbaum. *Interatomic electronic decay processes in singly and multiply ionized clusters.* J. El. Spect. Rel. Phenom. **183**(1-3), 36 (2011).

[18] T. Jahnke. *Interatomic and intermolecular Coulombic decay: The coming of age story.* J. Phys. B: At. Mol. Opt. Phys. **48**(8), 082001 (2015).

[19] T. Jahnke, U. Hergenhahn, B. Winter, R. Dörner, U. Frühling, P. V. Demekhin, K. Gokhberg, L. S. Cederbaum, A. Ehresmann, A. Knie, and A. Dreuw. *Interatomic and intermolecular coulombic decay.* Chem. Rev. **120**(20), 11295 (2020).

[20] A. J. F. Siegert. *On the derivation of the dispersion formula for nuclear reactions.* Phys. Rev. **56**, 750 (1939).

[21] G. Gamow. *Zur Quantentheorie des Atomkernes.* Z. Phys. **51**(3), 204 (1928).

[22] J. R. Taylor. *Scattering Theory: The quantum Theory on Nonrelativistic Collisions* (Wiley, New York, 1972).

[23] S. Klaiman and I. Gilary. *On resonance: A first glance into the behavior of unstable states.* In C. Nicolaides and E. Brandas, eds., *Unstable states in the continuous spectra, part II – Interpretation, theory and applications*, vol. 63 of *Advances in Quantum Chemistry*, pp. 1–31 (Elsevier, 2012).

[24] P. Dirac. *Über die Quantenmechanik der Stoßvorgänge.* Z. Phys. **44**(8), 585 (1927).

[25] U. Fano. *Effects of configuration interaction on intensities and phase shifts.* Phys. Rev. **124**(6), 1866 (1961).

[26] H. Feshbach. *Unified theory of nuclear reactions.* Ann. Phys. **5**(4), 357 (1958).

[27] W. Domcke. *Theory of resonance and threshold effects in electron-molecule collisions: The projection operator approach.* Phys. Rep. **208**(2), 97 (1991).

[28] O. Vendrell, S. D. Stoychev, and L. S. Cederbaum. *Generation of Highly Damaging H_2O^+ Radicals by Inner Valence Shell Ionization of Water.* ChemPhysChem **11**(5), 1006 (2010).

[29] N. Sisourat. *Nuclear dynamics of decaying states: A semiclassical approach.* J. Chem. Phys. **139**(7), 074111 (2013).

[30] T. Åberg. *Theory of X-Ray Satellites.* Phys. Rev. **156**, 35 (1967).

[31] B. T. Pickup. *On the theory of fast photoionization processes.* Chem. Phys. **19**(2), 193 (1977).

[32] O. Gunnarsson and K. Schönhammer. *Dynamical theory of Auger processes.* Phys. Rev. B **22**, 3710 (1980).

[33] A. S. Davydov. *Quantum Mechanics* (Pergamon Press Ltd., 1965).

[34] L. S. Cederbaum and F. Tarantelli. *Nuclear dynamics of several decaying overlapping electronic states: A time-dependent formulation.* J. Chem. Phys. **99**(8), 5871 (1993).

[35] F. Kaspar, W. Domcke, and L. S. Cederbaum. *The influence of finite lifetime of electronic states on the vibrational structure of molecular electronic spectra.* Chem. Phys. **44**(1), 33 (1979).

[36] E. Pahl, H.-D. Meyer, and L. Cederbaum. *Competition between excitation and electronic decay of short-lived molecular states.* Z. Phys. D **38**(3), 215 (1996).

[37] M. Berman, L. S. Cederbaum, and W. Domcke. *Analysis of the ambiguities in the definition of the local complex potential in resonant electron-molecule scattering.* J. Phys. B: At. Mol. Opt. Phys. **16**(5), 875 (1983).

[38] A. Herzenberg. *Oscillatory energy dependence of resonant electron-molecule scattering.* J. Phys. B: At. Mol. Opt. Phys. **1**(4), 548 (1968).

[39] D. T. Birtwistle and A. Herzenberg. *Vibrational excitation of N_2 by resonance scattering of electrons.* J. Phys. B: At. Mol. Opt. Phys. **4**(1), 53 (1971).

[40] L. S. Cederbaum and W. Domcke. *Local against non-local complex potential in resonant electron-molecule scattering.* J. Phys. B: At. Mol. Opt. Phys. **14**(23), 4665 (1981).

[41] M. V. Fedorov. *Resonant ionisation of atoms and switching-on of the interaction.* J. Phys. B: At. Mol. Opt. Phys. **10**(13), 2573 (1977).

[42] M. E. Sukharev, E. Charron, A. Suzor-Weiner, and M. V. Fedorov. *Calculations of photodissociation in intense laser fields: Validity of the adiabatic elimination of the continuum.* Int. J. Quant. Chem. **99**(4), 452 (2004).

[43] E. P. Wigner. *On the behavior of cross sections near thresholds.* Phys. Rev. **73**, 1002 (1948).

[44] W. Domcke. *Analytic theory of resonances and bound states near Coulomb thresholds.* J. Phys. B: At. Mol. Opt. Phys. **16**(3), 359 (1983).

[45] L. Fonda, G. C. Ghirardi, and A. Rimini. *Decay theory of unstable quantum systems.* Reports on Progress in Physics **41**(4), 587 (1978).

[46] K. J. F. Gaemers and T. D. Visser. *Deviations from exponential decay in quantum mechanics.* Physica A **153**(2), 234 (1988).

[47] S. R. Wilkinson, C. F. Bharucha, M. C. Fischer, K. W. Madison, P. R. Morrow, Q. Niu, B. Sundaram, and M. G. Raizen. *Experimental evidence for non-exponential decay in quantum tunnelling.* Nature **387**, 575 (1997).

[48] F. H. Mies. *Configuration interaction theory. Effects of overlapping resonances.* Phys. Rev. **175**, 164 (1968).

[49] H. Estrada, L. S. Cederbaum, and W. Domcke. *Vibronic coupling of short-lived electronic states.* J. Chem. Phys. **84**(1), 152 (1986).

[50] S. Feuerbacher, T. Sommerfeld, and L. S. Cederbaum. *Intersections of potential energy surfaces of short-lived states: The complex analogue of conical intersections.* J. Chem. Phys. **120**(7), 3201 (2004).

[51] G. Howat, T. Åberg, and O. Goscinski. *Relaxation and final-state channel mixing in the Auger effect.* J. Phys. B: At. Mol. Opt. Phys. **11**(9), 1575 (1978).

[52] N. Moiseyev. *Quantum theory of resonances: calculating energies, widths and cross-sections by complex scaling.* Phys. Rep. **302**(5), 212 (1998).

[53] N. Moiseyev. *Non-Hermitian Quantum Mechanics* (Cambridge University Press, 2011).

[54] C. Mundel and W. Domcke. *Nuclear dynamics in resonant electron-molecule scattering beyond the local approximation: model calculations on dissociative attachment and vibrational excitation.* J. Phys. B: At. Mol. Opt. Phys. **17**(17), 3593 (1984).

[55] J. Horáček, M. Čížek, and W. Domcke. *Generalization of the nonlocal resonance model for low-energy electron collisions with hydrogen halides: the variable threshold exponent.* Theor. Chem. Acc. **100**(1), 31 (1998).

[56] J. Horáček, M. Čížek, K. Houfek, P. Kolorenč, and W. Domcke. *Dissociative electron attachment and vibrational excitation of* H_2 *by low-energy electrons: Calculations based on an improved nonlocal resonance model.* Phys. Rev. A **70**, 052712 (2004).

[57] L. S. Cederbaum and F. Tarantelli. *Nuclear dynamics of decaying states: A time-dependent formulation.* J. Chem. Phys. **98**(12), 9691 (1993).

[58] S. Scheit, L. S. Cederbaum, and H.-D. Meyer. *Time-dependent interplay between electron emission and fragmentation in the interatomic Coulombic decay.* J. Chem. Phys. **118**(5), 2092 (2003).

[59] C. J. Ballhausen and A. E. Hansen. *Electronic spectra.* Ann. Rev. Phys. Chem. **23**(1), 15 (1972).

[60] T. Pacher, L. S. Cederbaum, and H. Köppel. *Approximately diabatic states from block diagonalization of the electronic Hamiltonian.* J. Chem. Phys. **89**(12), 7367 (1988).

[61] W. Lichten. *Resonant charge exchange in atomic collisions.* Phys. Rev. **131**, 229 (1963).

[62] C. A. Mead and D. G. Truhlar. *Conditions for the definition of a strictly diabatic electronic basis for molecular systems.* J. Chem. Phys. **77**(12), 6090 (1982).

[63] Y.-C. Chiang, F. Otto, H.-D. Meyer, and L. S. Cederbaum. *Interrelation between the distributions of kinetic energy release and emitted electron energy following the decay of electronic states.* Phys. Rev. Lett. **107**, 173001 (2011).

[64] N. Moiseyev, S. Scheit, and L. S. Cederbaum. *Non-Hermitian quantum mechanics: Wave packet propagation on autoionizing potential energy surfaces.* J. Chem. Phys. **121**(2), 722 (2004).

[65] S. Scheit, V. Averbukh, H.-D. Meyer, J. Zobeley, and L. S. Cederbaum. *Interatomic Coulombic decay in a heteroatomic rare gas cluster.* J. Chem. Phys. **124**(15), 154305 (2006).

[66] E. Pahl, H.-D. Meyer, L. S. Cederbaum, D. Minelli, and F. Tarantelli. *Adiabatic and nonadiabatic effects of nuclear dynamics in spectra of decaying states: Auger spectrum of HF.* J. Chem. Phys. **105**(20), 9175 (1996).

[67] H. A. Kramers and W. Heisenberg. *Über die Streuung von Strahlung durch Atome.* Z. Phys. **31**(1), 681 (1925).

[68] J. J. Sakurai. *Advanced Quantum Mechanics* (Addison-Wesley, 1967).

[69] Y.-C. Chiang, F. Otto, H.-D. Meyer, and L. S. Cederbaum. *Kinetic energy release in fragmentation processes following electron emission: A time-dependent approach.* J. Chem. Phys. **136**(11), 114111 (2012).

[70] A. Cesar and H. Ågren. *State interference in resonance Auger and X-ray emission.* Phys. Rev. A **45**, 2833 (1992).

[71] M. Beck, A. Jäckle, G. Worth, and H.-D. Meyer. *The multiconfiguration time-dependent Hartree (MCTDH) method: a highly efficient algorithm for propagating wavepackets.* Phys. Rep. **324**(1), 1 (2000).

[72] P. Burke and K. Berrington, eds. *Atomic and molecular processes: an R-matrix approach* (Bristol: IOP Publishing, 1993).

[73] P. V. Demekhin, A. Ehresmann, and V. L. Sukhorukov. *Single center method: A computational tool for ionization and electronic excitation studies of molecules.* J. Chem. Phys. **134**(2), 024113 (2011).

[74] V. Averbukh and L. S. Cederbaum. *Ab initio calculation of interatomic decay rates by a combination of the Fano ansatz, Green's-function methods, and the Stieltjes imaging technique.* J. Chem. Phys. **123**(20), 204107 (2005).

[75] H. Feshbach. *Unified theory of nuclear reactions.* Rev. Mod. Phys. **36**, 1076 (1964).

[76] J. Schirmer. *Beyond the random-phase approximation: A new approximation scheme for the polarization propagator.* Phys. Rev. A **26**, 2395 (1982).

[77] J. Schirmer, L. S. Cederbaum, and O. Walter. *New approach to the one-particle Green's function for finite Fermi systems.* Phys. Rev. A **28**(3), 1237 (1983).

[78] J. Schirmer. *Closed-form intermediate representations of many-body propagators and resolvent matrices.* Phys. Rev. A **43**(9), 4647 (1991).

[79] F. Mertins and J. Schirmer. *Algebraic propagator approaches and intermediate-state representations. I. The biorthogonal and unitary coupled-cluster methods.* Phys. Rev. A **53**(4), 2140 (1996).

[80] P. W. Langhoff. *Stieltjes-Tchebycheff moment-theory approach to molecular photoionization studies.* In T. Rescigno, V. McKoy, and B. Schenider, eds., *Electron-Molecule and Photon-Molecule Collisions*, p. 183 (Plenum, New York, 1979).

[81] A. U. Hazi. *Stieltjes-moment-theory technique for calculating resonance widths.* In T. Rescigno, V. McKoy, and B. Schenider, eds., *Electron-Molecule and Photon-Molecule Collisions*, p. 281 (Plenum, New York, 1979).

[82] K. Gokhberg, V. Averbukh, and L. S. Cederbaum. *Interatomic decay of inner-valence-excited states in clusters.* J. Chem. Phys. **124**(14), 144315 (2006).

[83] S. Kopelke, K. Gokhberg, V. Averbukh, F. Tarantelli, and L. S. Cederbaum. *Ab initio interatomic decay widths of excited states by applying Stieltjes imaging to Lanczos pseudospectra.* J. Chem. Phys. **134**(9), 094107 (2011).

[84] R. Yun, E. Narevicius, and V. Averbukh. *Penning ionization widths by Fano-algebraic diagrammatic construction method.* J. Chem. Phys. **148**(11), 114101 (2018).

[85] P. Kolorenč and N. Sisourat. *Interatomic Coulombic decay widths of helium trimer: Ab initio calculations.* J. Chem. Phys. **143**(22), 224310 (2015).

[86] M. Pernpointner, N. V. Kryzhevoi, and S. Urbaczek. *Possible electronic decay channels in the ionization spectra of small clusters composed of Ar and Kr: A four-component relativistic treatment.* J. Chem. Phys. **129**(2), 024304 (2008).

[87] E. Fasshauer, P. Kolorenč, and M. Pernpointner. *Relativistic decay widths of autoionization processes: The relativistic FanoADC-Stieltjes method.* J. Chem. Phys. **142**(14) (2015).

[88] E. Fasshauer. *Effect of spin-orbit coupling on decay widths of electronic decay processes.* J. Chem. Phys. **152**(22) (2020).

[89] J. Schirmer and A. Barth. *Higher-order approximations for the particle-particle propagator.* Z. Phys. A **317**, 267 (1984).

[90] A. Tarantelli and L. S. Cederbaum. *Approximation scheme for the three-particle propagator.* Phys. Rev. A **46**, 81 (1992).

[91] A. B. Trofimov, G. Stelter, and J. Schirmer. *A consistent third-order propagator method for electronic excitation.* J. Chem. Phys. **111**(22), 9982 (1999).

[92] J. Schirmer. *Many-Body Methods for Atoms, Molecules and Clusters*, vol. 94 of *Lecture Notes in Chemistry* (Springer International Publishing, 2018).

[93] A. Szabo and N. S. Ostlund. *Modern Quantum Chemistry* (Dover, New York, 1996).

[94] T. A. Carlson and M. O. Krause. *Experimental evidence for double electron emission in an Auger process.* Phys. Rev. Lett. **14**, 390 (1965).

[95] V. Averbukh and L. S. Cederbaum. *Calculation of interatomic decay widths of vacancy states delocalized due to inversion symmetry.* J. Chem. Phys. **125**, 094107 (2006).

[96] W. P. Reinhardt. *L^2 discretization of atomic and molecular electronic continua: Moment, quadrature and J-matrix techniques.* Comp. Phys. Commun. **17**(1), 1 (1979).

[97] I. Cacelli, V. Carravetta, and R. Moccia. *Photoionization cross section calculations of HCl by the Stieltjes technique.* Mol. Phys. **59**(3), 385 (1986).

[98] V. Stumpf, S. Scheit, P. Kolorenč, and K. Gokhberg. *Electron transfer mediated decay in NeXe triggered by K-LL Auger decay of Ne.* Chem. Phys. **482**, 192 (2017).

[99] U. V. Riss and H. D. Meyer. *Calculation of resonance energies and widths using the complex absorbing potential method.* J. Phys. B: At. Mol. Opt. Phys. **26**(23), 4503 (1993).

[100] U. V. Riss and H.-D. Meyer. *Investigation on the reflection and transmission properties of complex absorbing potentials.* J. Chem. Phys. **105**(4), 1409 (1996).

[101] Z. Mašín, J. Benda, J. D. Gorfinkiel, A. G. Harvey, and J. Tennyson. *UKRmol+: A suite for modelling electronic processes in molecules interacting with electrons, positrons and photons using the R-matrix method.* Comp. Phys. Commun. **249**, 107092 (2020).

[102] A. C. Brown, G. S. Armstrong, J. Benda, D. D. Clarke, J. Wragg, K. R. Hamilton, Z. Mašín, J. D. Gorfinkiel, and H. W. van der Hart. *RMT: R-matrix with time-dependence. solving the semi-relativistic, time-dependent Schrödinger equation for general, multielectron atoms and molecules in intense, ultrashort, arbitrarily polarized laser pulses.* Comp. Phys. Commun. **250**, 107062 (2020).

[103] A. Landau, D. Bhattacharya, I. Haritan, A. Ben-Asher, and N. Moiseyev. *Ab initio complex potential energy surfaces from standard quantum chemistry packages.* In Sabin, JR and Brandas, EJ, ed., *Advances in Quantum Chemistry: Lowdin Volume*, vol. 74, pp. 321–346 (Academic Press, 2017).

[104] N. Vaval and L. S. Cederbaum. *Ab initio lifetimes in the interatomic Coulombic decay of neon clusters computed with propagators.* J. Chem. Phys. **126**(16), 164110 (2007).

[105] K. Gokhberg, A. B. Trofimov, T. Sommerfeld, and L. S. Cederbaum. *Ionization of metal atoms following valence-excitation of neighbouring molecules.* Europhys. Lett. **72**(2), 228 (2005).

[106] R. Santra and L. S. Cederbaum. *Non-Hermitian electronic theory and applications to clusters.* Phys. Rep. **368**(1), 1 (2002).

[107] Y.-G. Peng, Y. Wu, L.-F. Zhu, S. B. Zhang, J.-G. Wang, H.-P. Liebermann, and R. J. Buenker. *Complex multireference configuration interaction calculations for the k-vacancy Auger states of nq+ (q = 2-5) ions.* J. Chem. Phys. **144**(5), 054306 (2016).

[108] S. B. Zhang and D. L. Yeager. *Complex-scaled multireference configuration-interaction method to study Be and Be-like cations' (B, C, N, O, Mg) Auger resonances* $1s2s^22p\ ^{1,3}P^o$. Phys. Rev. A **85**, 032515 (2012).

[109] Y. Sajeev, A. Ghosh, N. Vaval, and S. Pal. *Coupled cluster methods for autoionisation resonances.* Int. Rev. Phys. Chem. **33**(3), 397 (2014).

[110] A. Ghosh, S. Pal, and N. Vaval. *Interatomic Coulombic decay in* $(HF)_n$ *(n = 2-3) clusters using CAP/EOM-CCSD method.* Mol. Phys. **112**(5-6), 669 (2014).

[111] A. Ghosh and N. Vaval. *Geometry-dependent lifetime of Interatomic Coulombic decay using equation-of-motion coupled cluster method.* J. Chem. Phys. **141**(23), 234108 (2014).

[112] B. Simon. *The definition of molecular resonance curves by the method of exterior complex scaling.* Phys. Lett. A **71**(2), 211 (1979).

[113] C. W. McCurdy, M. Baertschy, and T. N. Rescigno. *Solving the three-body Coulomb breakup problem using exterior complex scaling.* J. Phys. B: At. Mol. Opt. Phys. **37**(17), R137 (2004).

[114] U. V. Riss and H.-D. Meyer. *The transformative complex absorbing potential method: A bridge between complex absorbing potentials and smooth exterior scaling.* J. Phys. B: At. Mol. Opt. Phys. **31**, 2279 (1998).

[115] J. Tennyson. *Electron–molecule collision calculations using the R-matrix method.* Phys. Rep. **491**(2), 29 (2010).

[116] P. Burke. *R-Matrix Theory of Atomic Collisions: Application to Atomic, Molecular and Optical Processes.* Springer Series on Atomic, Optical, and Plasma Physics (Springer Berlin Heidelberg, 2011).

[117] F. T. Smith. *Lifetime matrix in collision theory.* Phys. Rev. **118**, 349 (1960).

[118] D. T. Stibbe and J. Tennyson. *TIMEDEL: A program for the detection and parameterization of resonances using the time-delay matrix.* Comp. Phys. Commun. **114**(1), 236 (1998).

[119] L. A. Morgan and P. G. Burke. *Low-energy electron scattering by HF.* J. Phys. B: At. Mol. Opt. Phys. **21**(11), 2091 (1988).

[120] J. M. Carr, P. G. Galiatsatos, J. D. Gorfinkiel, A. G. Harvey, M. A. Lysaght, D. Madden, Z. Mašín, M. Plummer, J. Tennyson, and H. N. Varambhia. *UKRmol: a low-energy electron- and positron-molecule scattering suite.* Eur. Phys. J. D **66**(3), 58 (2012).

[121] T. Havermeier, T. Jahnke, K. Kreidi, R. Wallauer, S. Voss, M. Schöffler, S. Schössler, L. Foucar, N. Neumann, J. Titze, H. Sann, M. Kühnel, J. Voigtsberger, J. H. Morilla, W. Schöllkopf, H. Schmidt-Böcking, R. E. Grisenti, and R. Dörner. *Interatomic Coulombic decay following photoionization of the helium dimer: Observation of vibrational structure.* Phys. Rev. Lett. **104**(13), 133401 (2010).

[122] F. Trinter, J. B. Williams, M. Weller, M. Waitz, M. Pitzer, J. Voigtsberger, C. Schober, G. Kastirke, C. Müller, C. Goihl, P. Burzynski, F. Wiegandt, T. Bauer, R. Wallauer, H. Sann, A. Kalinin, L. P. H. Schmidt, M. Schöffler, N. Sisourat, and T. Jahnke. *Evolution of interatomic Coulombic decay in the time domain.* Phys. Rev. Lett. **111**, 093401 (2013).

[123] B. M. Nestmann. *Characterization of metastable anionic states within theR-matrix approach.* J. Phys. B: At. Mol. Opt. Phys. **31**(17), 3929 (1998).

[124] P. Kolorenč, V. Brems, and J. Horáček. *Computing resonance positions, widths, and cross sections via the Feshbach-Fano R-matrix method: Application to potential scattering.* Phys. Rev. A **72**(1), 012708 (2005).

[125] N. V. Kryzhevoi, V. Averbukh, and L. S. Cederbaum. *High activity of helium droplets following ionization of systems inside those droplets.* Phys. Rev. B **76**, 094513 (2007).

[126] E. Fasshauer, M. Foerstel, S. Pallmann, M. Pernpointner, and U. Hergenhahn. *Using ICD for structural analysis of clusters: a case study on NeAr clusters.* New J. Phys. **16**, 103026 (2014).

[127] F. O. Ellison. *A Method of Diatomics in Molecules. I. General Theory and Application to H_2O.* J. Am. Chem. Soc. **85**, 3540 (1963).

[128] A. K. Belyaev, A. S. Tiukanov, and W. Domcke. *Generalized diatomics-in-molecules method for polyatomic anions.* Phys. Rev. A **65**, 012508 (2001).

[129] N. Sisourat, S. Kazandjian, A. Randimbiarisolo, and P. Kolorenč. *Interatomic Coulombic decay widths of helium trimer: A diatomics-in-molecules approach.* J. Chem. Phys. **144**(8), 084111 (2016).

[130] V. Weisskopf and E. Wigner. *Berechnung der natürlichen Linienbreite auf Grund der Diracschen Lichttheorie.* Z. Phys. **63**(1), 54 (1930).

[131] J. J. Sakurai. *Modern Quantum Mechanics, Revised Edition* (Addison-Wesley, 1994).

[132] J. Matthew and Y. Komninos. *Transition rates for interatomic Auger processes.* Surf. Sci. **53**(1), 716 (1975).

[133] V. Averbukh, I. B. Müller, and L. S. Cederbaum. *Mechanism of interatomic Coulombic decay in clusters.* Phys. Rev. Lett. **93**(26), 263002 (2004).

[134] K. Gokhberg, S. Kopelke, N. V. Kryzhevoi, P. Kolorenč, and L. S. Cederbaum. *Dependence of interatomic decay widths on the symmetry of the decaying state: Analytical expressions and* ab initio *results.* Phys. Rev. A **81**(1), 013417 (2010).

[135] D. A. Verner, G. J. Ferland, K. T. Korista, and D. G. Yakovlev. *Atomic Data for Astrophysics. II. New Analytic FITS for Photoionization Cross Sections of Atoms and Ions.* Astrophys. J. **465**, 487 (1996).

[136] J. Zobeley, R. Santra, and L. S. Cederbaum. *Electronic decay in weakly bound heteroclusters: Energy transfer versus electron transfer.* J. Chem. Phys. **115**(11), 5076 (2001).

[137] N. Sisourat, H. Sann, N. V. Kryzhevoi, P. Kolorenč, T. Havermeier, F. Sturm, T. Jahnke, H.-K. Kim, R. Dörner, and L. S. Cederbaum. *Interatomic electronic decay driven by nuclear motion.* Phys. Rev. Lett. **105**(17), 173401 (2010).

[138] A. Kuki. *Electronic tunneling paths in proteins.* In J. R. Winkler, ed., *Long-Range Electron Transfer in Biology*, vol. 75, pp. 49–83 (Springer, Berlin, Heidelberg, 1991).

[139] T. Renger, V. May, and O. Kühn. *Ultrafast excitation energy transfer dynamics in photosynthetic pigment–protein complexes.* Phys. Rep. **343**(3), 137 (2001).

[140] H. Agueny, M. Pesche, B. Lutet-Toti, T. Miteva, A. Molle, J. Caillat, and N. Sisourat. *Interparticle coulombic decay in coupled quantum dots: Enhanced energy transfer via bridge assisted mechanisms.* Phys. Rev. B **101**, 195431 (2020).

[141] J. L. Hemmerich, R. Bennett, and S. Y. Buhmann. *The influence of retardation and dielectric environments on interatomic Coulombic decay.* Nat. Commun. **9**, 2934 (2018).

[142] R. Sánchez, F. Gallego-Marcos, and G. Platero. *Superexchange blockade in triple quantum dots.* Phys. Rev. B **89**, 161402 (2014).

[143] V. Averbukh and L. S. Cederbaum. *Interatomic electronic decay in endohedral fullerenes.* Phys. Rev. Lett. **96**(5), 053401 (2006).

[144] V. V. Afrosimov, Y. S. Gordeev, A. N. Zinovev, D. K. Rasulov, and A. P. Shergin. *Observation of new types of Auger transitions in atoms with 2 internal vacancies.* JETP Lett. **21**(9), 249 (1975).

[145] E. De Filippo, G. Lanzanò, H. Rothard, and C. Volant. *Three-electron Auger process from beam-foil excited multiply charged ions.* Phys. Rev. Lett. **100**, 233202 (2008).

[146] T. Ouchi, K. Sakai, H. Fukuzawa, X.-J. Liu, I. Higuchi, Y. Tamenori, K. Nagaya, H. Iwayama, M. Yao, D. Zhang, D. Ding, A. I. Kuleff, S. D. Stoychev, P. V. Demekhin, N. Saito, and K. Ueda. *Three-electron interatomic Coulombic decay from the inner-valence double-vacancy states in NeAr.* Phys. Rev. Lett. **107**, 053401 (2011).

[147] A. Müller, A. Borovik, T. Buhr, J. Hellhund, K. Holste, A. L. D. Kilcoyne, S. Klumpp, M. Martins, S. Ricz, J. Viefhaus, and S. Schippers. *Observation of a four-electron Auger process in near-K-edge photoionization of singly charged carbon ions.* Phys. Rev. Lett. **114**, 013002 (2015).

[148] P. Kolorenč, V. Averbukh, R. Feifel, and J. Eland. *Collective relaxation processes in atoms, molecules and clusters.* J. Phys. B: At. Mol. Opt. Phys. **49**(8), 082001 (2016).

[149] A. H. Roos, J. H. D. Eland, J. Andersson, R. J. Squibb, D. Koulentianos, O. Talaee, and R. Feifel. *Abundance of molecular triple ionization by double Auger decay.* Sci. Rep. **8** (2018).

[150] A. C. LaForge, M. Drabbels, N. B. Brauer, M. Coreno, M. Devetta, M. Di Fraia, P. Finetti, C. Grazioli, R. Katzy, V. Lyamayev, T. Mazza, M. Mudrich, P. O'Keeffe, Y. Ovcharenko, P. Piseri, O. Plekan, K. C. Prince, R. Richter, S. Stranges, C. Callegari, T. Moeller, and F. Stienkemeier. *Collective Autoionization in Multiply-Excited Systems: A novel ionization process observed in Helium Nanodroplets.* Sci. Rep. **4**, 3621 (2014).

[151] Y. Ovcharenko, V. Lyamayev, R. Katzy, M. Devetta, A. LaForge, P. O'Keeffe, O. Plekan, P. Finetti, M. Di Fraia, M. Mudrich, M. Krikunova, P. Piseri, M. Coreno, N. B. Brauer, T. Mazza, S. Stranges, C. Grazioli, R. Richter, K. C. Prince, M. Drabbels, C. Callegari, F. Stienkemeier, and T. Möller. *Novel collective autoionization process observed in electron spectra of He clusters.* Phys. Rev. Lett. **112**, 073401 (2014).

[152] R. Obaid, H. Xiong, S. Augustin, K. Schnorr, U. Ablikim, A. Battistoni, T. J. A. Wolf, R. C. Bilodeau, T. Osipov, K. Gokhberg, D. Rolles, A. C. LaForge, and N. Berrah. *Intermolecular Coulombic decay in endohedral fullerene at the* $4d \rightarrow 4f$ *resonance.* Phys. Rev. Lett. **124**, 113002 (2020).

[153] A. C. LaForge, M. Shcherbinin, F. Stienkemeier, R. Richter, R. Moshammer, T. Pfeifer, and M. Mudrich. *Highly efficient double ionization of mixed alkali dimers by intermolecular Coulombic decay.* Nat. Phys. **15**(3), 247 (2019).

[154] A. I. Kuleff, K. Gokhberg, S. Kopelke, and L. S. Cederbaum. *Ultrafast interatomic electronic decay in multiply excited clusters.* Phys. Rev. Lett. **105**(4), 043004 (2010).

[155] C. Richter, D. Hollas, C.-M. Saak, M. Förstel, T. Miteva, M. Mucke, O. Björneholm, N. Sisourat, P. Slavíček, and U. Hergenhahn. *Competition between proton transfer and intermolecular Coulombic decay in water.* Nat. Commun. **9**(1), 4988 (2018).

[156] R. E. Grisenti, W. Schöllkopf, J. P. Toennies, G. C. Hegerfeldt, T. Köhler, and M. Stoll. *Determination of the bond length and binding energy of the helium dimer by diffraction from a transmission grating.* Phys. Rev. Lett. **85**, 2284 (2000).

[157] M. Przybytek, W. Cencek, J. Komasa, G. Łach, B. Jeziorski, and K. Szalewicz. *Relativistic and quantum electrodynamics effects in the helium pair potential.* Phys. Rev. Lett. **104**, 183003 (2010).

[158] S. Scheit, V. Averbukh, H.-D. Meyer, N. Moiseyev, R. Santra, T. Sommerfeld, J. Zobeley, and L. S. Cederbaum. *On the interatomic Coulombic decay in the Ne dimer.* J. Chem. Phys. **121**(17), 8393 (2004).

[159] E. A. Gislason. *Series expansions for Franck-Condon factors. I. Linear potential and the reflection approximation.* J. Chem. Phys. **58**(9), 3702 (1973).

[160] T. Jahnke, A. Czasch, M. Schöffler, S. Schössler, M. Käsz, J. Titze, K. Kreidi, R. E. Grisenti, A. Staudte, O. Jagutzki, L. P. H. Schmidt, T. Weber, H. Schmidt-Böcking, K. Ueda, and R. Dörner. *Experimental separation of virtual photon exchange and electron transfer in interatomic Coulombic decay of neon dimers.* Phys. Rev. Lett. **99**, 153401 (2007).

[161] V. Stumpf, S. Scheit, P. Kolorenč, and K. Gokhberg. *Electron transfer mediated decay in NeXe triggered by K-LL Auger decay of Ne.* Chem. Phys. **482**, 192 (2017).

[162] F. Trinter, M. S. Schoeffler, H.-K. Kim, F. P. Sturm, K. Cole, N. Neumann, A. Vredenborg, J. Williams, I. Bocharova, R. Guillemin, M. Simon, A. Belkacem, A. L. Landers, T. Weber, H. Schmidt-Boecking, R. Doerner, and T. Jahnke. *Resonant Auger decay driving intermolecular Coulombic decay in molecular dimers.* Nature **505**(7485), 664 (2014).

[163] T. Miteva, Y.-C. Chiang, P. Kolorenč, A. I. Kuleff, L. S. Cederbaum, and K. Gokhberg. *The effect of the partner atom on the spectra of interatomic Coulombic decay triggered by resonant Auger processes.* J. Chem. Phys. **141**(16), 164303 (2014).

[164] M. Kimura, H. Fukuzawa, T. Tachibana, Y. Ito, S. Mondal, M. Okunishi, M. Schöffler, J. Williams, Y. Jiang, Y. Tamenori, N. Saito, and K. Ueda. *Controlling low-energy electron emission via resonant-Auger-induced interatomic Coulombic decay.* J. Phys. Chem. Lett. **4**(11), 1838 (2013).

[165] P. O'Keeffe, E. Ripani, P. Bolognesi, M. Coreno, M. Devetta, C. Callegari, M. Di Fraia, K. C. Prince, R. Richter, M. Alagia, A. Kivimäki, and L. Avaldi. *The role of the partner*

atom and resonant excitation energy in interatomic Coulombic decay in rare gas dimers. J. Phys. Chem. Lett. **4**(11), 1797 (2013).

[166] M. Kimura, H. Fukuzawa, K. Sakai, S. Mondal, E. Kukk, Y. Kono, S. Nagaoka, Y. Tamenori, N. Saito, and K. Ueda. *Efficient site-specific low-energy electron production via interatomic Coulombic decay following resonant Auger decay in argon dimers.* Phys. Rev. A **87**, 043414 (2013).

[167] X. Ren, T. Miteva, P. Kolorenč, K. Gokhberg, A. I. Kuleff, L. S. Cederbaum, and A. Dorn. *Observation of fast and slow interatomic Coulombic decay in argon dimers induced by electron-impact ionization.* Phys. Rev. A **96**, 032715 (2017).

[168] J. A. de Gouw, J. van Eck, A. C. Peters, J. van der Weg, and H. G. M. Heideman. *Resonant Auger spectra of the* $2p^{-1}\,nl$ *states of argon.* J. Phys. B: At. Mol. Opt. Phys. **28**(11), 2127 (1995).

[169] J. C. Fuggle and S. F. Alvarado. *Core-level lifetimes as determined by X-ray photoelectron spectroscopy measurements.* Phys. Rev. A **22**, 1615 (1980).

[170] A. Ku, V. J. Facca, Z. Cai, and R. M. Reilly. *Auger electrons for cancer therapy – a review.* EJNMMI Radiopharmacy and Chemistry **4**(1), 27 (2019).

[171] T. Ouchi, K. Sakai, H. Fukuzawa, I. Higuchi, P. V. Demekhin, Y.-C. Chiang, S. D. Stoychev, A. I. Kuleff, T. Mazza, M. Schöffler, K. Nagaya, M. Yao, Y. Tamenori, N. Saito, and K. Ueda. *Interatomic Coulombic decay following Ne* 1*s Auger decay in NeAr.* Phys. Rev. A **83**, 053415 (2011).

[172] B. Ulrich, A. Vredenborg, A. Malakzadeh, L. P. H. Schmidt, T. Havermeier, M. Meckel, K. Cole, M. Smolarski, Z. Chang, T. Jahnke, and et al. *Imaging of the structure of the argon and neon dimer, trimer, and tetramer.* J. Phys. Chem. A **115**(25), 6936–6941 (2011).

[173] A. Nicklass, M. Dolg, H. Stoll, and H. Preuss. *Ab initio energy-adjusted pseudopotentials for the noble gases Ne through Xe: Calculation of atomic dipole and quadrupole polarizabilities.* J. Chem. Phys. **102**(22), 8942 (1995).

[174] F. Aquilante, L. De Vico, N. Ferré, G. Ghigo, P.-r. Malmqvist, P. Neogrády, T. B. Pedersen, M. Pitoňák, M. Reiher, B. O. Roos, L. Serrano-Andrés, M. Urban, V. Veryazov, and R. Lindh. *Molcas 7: The next generation.* J. Comp. Chem. **31**(1), 224 (2010).

[175] K. Kaufmann, W. Baumeister, and M. Jungen. *Universal Gaussian basis sets for an optimum representation of Rydberg and continuum wavefunctions.* J. Phys. B: At. Mol. Opt. Phys. **22**(14), 2223 (1989).

[176] P. Slavíček, R. Kalus, P. Paška, I. Odvárková, P. Hobza, and A. Malijevský. *State-of-the-art correlated ab initio potential energy curves for heavy rare gas dimers: Ar_2, Kr_2, and Xe_2.* J. Chem. Phys. **119**(4), 2102 (2003).

[177] A. Kramida, Yu. Ralchenko, J. Reader, and and NIST ASD Team. NIST Atomic Spectra Database (ver. 5.7.1), [Online]. Available: `https://physics.nist.gov/asd` [2019, October 22]. National Institute of Standards and Technology, Gaithersburg, MD. (2019).

[178] A. Kikas, S. Osborne, A. Ausmees, S. Svensson, O.-P. Sairanen, and S. Aksela. *High-resolution study of the correlation satellites in photoelectron spectra of the rare gases.* J. El. Spect. Rel. Phenom. **77**(3), 241 (1996).

[179] D. Schwickert, M. Ruberti, P. Kolorenč, S. Usenko, A. Przystawik, K. Baev, I. Baev, M. Braune, L. Bocklage, M. K. Czwalinna, S. Deinert, S. Düsterer, A. Hans, G. Hartmann, C. Haunhorst, M. Kuhlmann, S. Palutke, R. Röhlsberger, J. Rönsch-Schulenburg, P. Schmidt, S. Toleikis, J. Viefhaus, M. Martins, A. Knie, D. Kip, V. Averbukh, J. P. Marangos, and T. Laarmann. *Electronic Quantum Coherence in Glycine Probed with Femtosecond X-rays.* arXiv:2012.04852v1 [physics.chem-ph] (2020). URL https://arxiv.org/abs/2012.04852.

List of original papers

[A1] Přemysl Kolorenč and Vitali Averbukh. Fano-ADC(2,2) method for electronic decay rates. *J. Chem. Phys.*, 152(21):214107, 2020. DOI:10.1063/5.0007912.

[A2] Přemysl Kolorenč, Vitali Averbukh, Kirill Gokhberg, and Lorenz S. Cederbaum. Ab initio calculation of interatomic decay rates of excited doubly ionized states in clusters. *J. Chem. Phys.*, 129(24):244102, 2008. DOI:10.1063/1.3043437.

[A3] Nicolas Sisourat, Selma Engin, Jimena D. Gorfinkiel, Sevan Kazandjian, Přemysl Kolorenč, and Tsveta Miteva. On the computations of interatomic Coulombic decay widths with R-matrix method. *J. Chem. Phys.*, 146(24):244109, 2017. DOI:10.1063/1.4989538.

[A4] Tsveta Miteva, Sevan Kazandjian, Přemysl Kolorenč, Petra Votavová, and Nicolas Sisourat. Interatomic Coulombic decay mediated by ultrafast superexchange energy transfer. *Phys. Rev. Lett.*, 119(8):083403, 2017. DOI:10.1103/PhysRevLett.119.083403.

[A5] Petra Votavová, Tsveta Miteva, Selma Engin, Sévan Kazandjian, Přemysl Kolorenč, and Nicolas Sisourat. Mechanism of superexchange interatomic Coulombic decay in rare-gas clusters. *Phys. Rev. A*, 100:022706, 2019. DOI:10.1103/PhysRevA.100.022706.

[A6] Robert Bennett, Petra Votavová, Přemysl Kolorenč, Tsveta Miteva, Nicolas Sisourat, and Stefan Yoshi Buhmann. Virtual photon approximation for three-body interatomic Coulombic decay. *Phys. Rev. Lett.*, 122:153401, 2019. DOI:10.1103/PhysRevLett.122.153401.

[A7] Raimund Feifel, John H. D. Eland, Richard J. Squibb, Melanie Mucke, Sergey Zagorodskikh, Per Linusson, Francesco Tarantelli, Přemysl Kolorenč, and Vitali Averbukh. Ultrafast molecular three-electron Auger decay. *Phys. Rev. Lett.*, 116:073001, 2016. DOI:10.1103/PhysRevLett.116.073001.

[A8] Vitali Averbukh and Přemysl Kolorenč. Collective interatomic decay of multiple vacancies in clusters. *Phys. Rev. Lett.*, 103(18):183001, 2009. DOI:10.1103/PhysRevLett.103.183001.

[A9] Nicolas Sisourat, Nikolai V. Kryzhevoi, Přremysl Kolorenč, Simona Scheit, Till Jahnke, and Lorenz S. Cederbaum. Ultralong-range energy transfer by interatomic Coulombic decay in an extreme quantum system. *Nat. Phys.*, 6(7):508–511, 2010. DOI:10.1038/nphys1685.

[A10] Přemysl Kolorenč, Nikolai V. Kryzhevoi, Nicolas Sisourat, and Lorenz S. Cederbaum. Interatomic Coulombic decay in a He dimer: Ab initio potential-energy curves and decay widths. *Phys. Rev. A*, 82(1):013422, 2010. DOI:10.1103/PhysRevA.82.013422.

[A11] Nicolas Sisourat, Nikolai V. Kryzhevoi, Přemysl Kolorenč, Simona Scheit, and Lorenz S. Cederbaum. Impact of nuclear dynamics on interatomic Coulombic decay in a He dimer. *Phys. Rev. A*, 82(5):053401, 2010. DOI:10.1103/PhysRevA.82.053401.

[A12] Vasili Stumpf, Přemysl Kolorenč, Kirill Gokhberg, and Lorenz S. Cederbaum. Efficient pathway to neutralization of multiply charged ions produced in Auger processes. *Phys. Rev. Lett.*, 110(25):258302, 2013. DOI:10.1103/PhysRevLett.110.258302.

[A13] Kirill Gokhberg, Premysl Kolorenč, Alexander I. Kuleff, and Lorenz S. Cederbaum. Site- and energy-selective slow-electron production through intermolecular Coulombic decay. *Nature*, 505(7485):661, 2014. DOI:10.1038/nature12936.

[A14] Tsveta Miteva, Ying-Chih Chiang, Přemysl Kolorenč, Alexander I. Kuleff, Kirill Gokhberg, and Lorenz S. Cederbaum. Interatomic Coulombic decay following resonant core excitation of Ar in argon dimer. *J. Chem. Phys.*, 141(6):064307, 2014. DOI:10.1063/1.4891986.

[A15] J. Rist, T. Miteva, B. Gaire, H. Sann, F. Trinter, M. Keiling, N. Gehrken, A. Moradmand, B. Berry, M. Zohrabi, M. Kunitski, I. Ben-Itzhak, A. Belkacem, T. Weber, A. L. Landers, M. Schoeffler, J. B. Williams, P. Kolorenč, K. Gokhberg, T. Jahnke, and R. Doerner. A comprehensive study of interatomic Coulombic decay in argon dimers: Extracting R-dependent absolute decay rates from the experiment. *Chem. Phys.*, 482:185–191, 2017. DOI:10.1016/j.chemphys.2016.09.024.

Appendix A

Original papers

(Removed from this version)